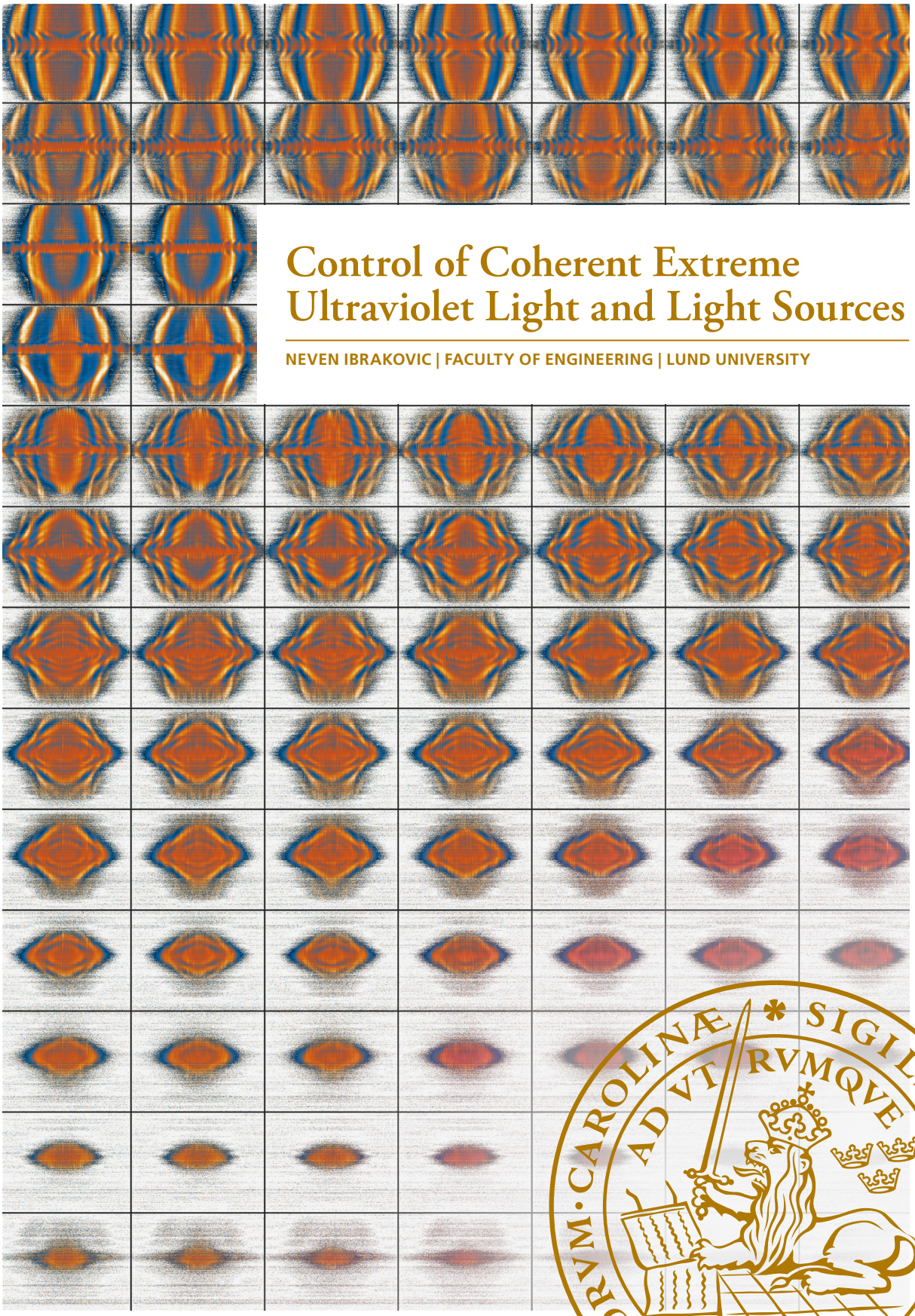

Control of Coherent Extreme Ultraviolet Light and Light Sources

NEVEN IBRAKOVIC | FACULTY OF ENGINEERING | LUND UNIVERSITY

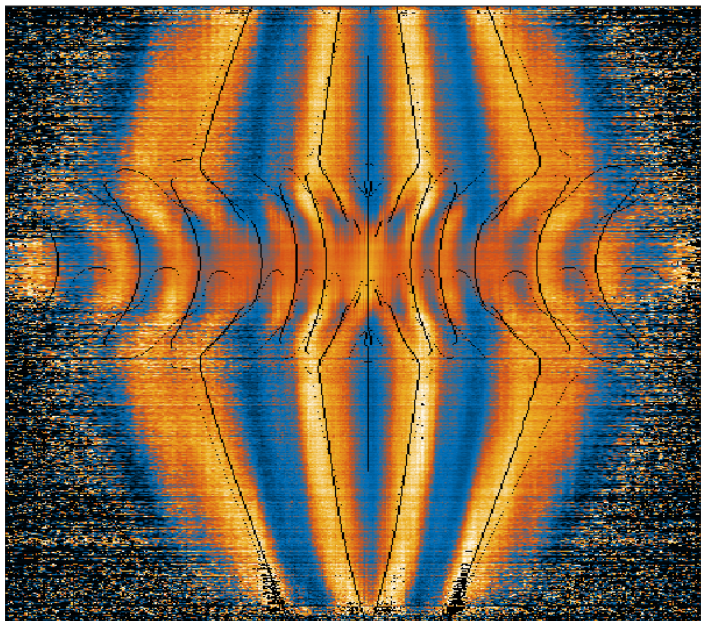

This one is my favorite.

Printed by Media-Tryck, Lund 2019 NORDIC SWAN ECOLABEL 3041 0903

Lund University,
Faculty of Engineering
Department of Physics

ISBN 978-91-7895-378-3
ISSN 0281-2762
Lund Reports on Atomic Physics, LRAP-562 (2019)

Control of Coherent Extreme Ultraviolet Light and Light Sources

Control of Coherent Extreme Ultraviolet Light and Light Sources

Neven Ibrakovic

LUND
UNIVERSITY

Thesis for the degree of Doctor of Philosophy
Thesis advisors: Professor Johan Mauritsson, Doctor Cord Arnold, Doctor Emma Simpson & Doctor Lars Rippe
Faculty opponent: Dr. Caterina Vozzi

To be presented, with the permission of the Faculty of Engineering of Lund University, for public criticism in the Rydberg lecture hall (Rydbergsalen) at the Department of Physics on Friday, the 17th of January 2020 at 09:15.

Organization
LUND UNIVERSITY

Department of Physics
Box 118
SE–221 00 LUND
Sweden

Document name
DOCTORAL DISSERTATION

Date of disputation
2020-01-17

Sponsoring organization

Author(s)
Neven Ibrakovic

Title and subtitle
Control of Coherent Extreme Ultraviolet Light and Light Sources:

Abstract
Coherent extreme ultraviolet (XUV) light sources are necessary for the investigation of physical processes in the natural length and time scales of atoms. These experiments require a high degree of control of the coherent XUV light. The optical components and techniques, which are available for visible and infrared light, unfortunately cannot be used for controlling XUV light. In this thesis, novel techniques to control ultraviolet to XUV light are presented. The sources of XUV light discussed in this thesis include: high-order harmonic generation, free electron lasers and nitrogen air lasing. These sources are complementary and are suited for different applications.

High-order harmonic generation produces XUV light with a very large spectral bandwidth, which can be compressed to produce the shortest light pulses to date. The yield of XUV light that can be produced through high-order harmonic generation is limited since the conversion efficiency of this process is low. Our experiments therefore aim to develop low-loss techniques for controlling the XUV light. We demonstrate techniques to measure and control the spatial phase of the harmonics using quantum path interference, and to control the XUV light after it is generated using opto-optical modulation.

In contrast to high-order harmonic generation, free electron lasers can produce XUV pulses with very high intensities and at tunable wavelengths. Furthermore, there are free electron lasers where the amplitude and phase control of the XUV light, when compared to other sources, is unparalleled. The pulses that are produced with FELs, however, are not sufficiently short to perform attosecond ($1 \cdot 10^{-18}$s) experiments. In this thesis, we describe a free electron laser experiment, where sub-femtosecond waveform structures are generated in a controlled and reproducible way. The results from this experiment present the possibility to perform attosecond physics using free electron lasers, a field which was previously confined to the high-order harmonic generation community.

Finally, experiments with nitrogen air lasing are also presented in this thesis. Unlike the other techniques, nitrogen air lasing does not produce XUV light. Instead, this technique produces coherent ultraviolet light, which is promising for atmospheric remote sensing. Since the mechanism generating the light with this technique is currently not understood, a recollision model, similar to the model describing high-order harmonics generation, is tested.

None of the aforementioned sources have the same intensity, coherence or possibility to be controlled as conventional lasers. Instead, these sources excel within their own parameter space. Our experiments aim to push these techniques to cover the gaps where none of these sources currently can be used.

Key words
ultrafast lasers, XUV optics, high-order harmonic generation, quantum path interference, opto-optical modulation, free electron lasers, nitrogen lasing

Classification system and/or index terms (if any)

Supplementary bibliographical information

Language
English

ISSN and key title
0281-2762
Lund Reports on Atomic Physics, LRAP-562

ISBN
978-91-7895-378-3 (print)
978-91-7895-379-0 (pdf)

Recipient's notes

Number of pages
151

Price

Security classification

Control of Coherent Extreme Ultraviolet Light and Light Sources

Neven Ibrakovic

LUND
UNIVERSITY

A doctoral thesis at a university in Sweden takes either the form of a single, cohesive research study (monograph) or a summary of research papers (compilation thesis), which the doctoral student has written alone or together with one or several other author(s).

In the latter case the thesis consists of two parts. An introductory text puts the research work into context and summarizes the main points of the papers. Then, the research publications themselves are reproduced, together with a description of the individual contributions of the authors. The research papers may either have been already published or are manuscripts at various stages (in press, submitted, or in draft).

Cover illustration front: Set of QPI measurements for different intensities.

Cover illustration back: My favourite QPI measurement: Harmonic 15.

Funding information:

Faculty of Engineering, Department of Physics

ISBN: 978-91-7895-378-3 (print)
ISBN: 978-91-7895-379-0 (pdf)
ISSN: 0281-2762
Lund Reports on Atomic Physics, LRAP-562

Printed in Sweden by Media-Tryck, Lund University, Lund 2019

Dedicated to the trustworthy Pharos laser; I could always rely on you.

Abstract

Coherent extreme ultraviolet (XUV) light sources are necessary for the investigation of physical processes in the natural length and time scales of atoms. These experiments require a high degree of control of the coherent XUV light. The optical components and techniques, which are available for visible and infrared light, unfortunately cannot be used for controlling XUV light. In this thesis, novel techniques to control ultraviolet to XUV light are presented. The sources of XUV light discussed in this thesis include: high-order harmonic generation, free electron lasers and nitrogen air lasing. These sources are complementary and are suited for different applications.

High-order harmonic generation produces XUV light with a very large spectral bandwidth, which can be compressed to produce the shortest light pulses to date. The yield of XUV light that can be produced through high-order harmonic generation is limited since the conversion efficiency of this process is low. Our experiments therefore aim to develop low-loss techniques for controlling the XUV light. We demonstrate techniques to measure and control the spatial phase of the harmonics using quantum path interference, and to control the XUV light after it is generated using opto-optical modulation.

In contrast to high-order harmonic generation, free electron lasers can produce XUV pulses with very high intensities and at tunable wavelengths. Furthermore, there are free electron lasers where the amplitude and phase control of the XUV light, when compared to other sources, is unparalleled. The pulses that are produced with FELs, however, are not sufficiently short to perform attosecond ($1 \cdot 10^{-18}$s) experiments. In this thesis, we describe a free electron laser experiment, where sub-femtosecond waveform structures are generated in a controlled and reproducible way. The results from this experiment present the possibility to perform attosecond physics using free electron lasers, a field which was previously confined to the high-order harmonic generation community.

Finally, experiments with nitrogen air lasing are also presented in this thesis. Unlike the other techniques, nitrogen air lasing does not produce XUV light. Instead, this technique produces coherent ultraviolet light, which is promising for atmospheric remote sensing. Since the mechanism generating the light with this technique is currently not understood, a recollision model, similar to the model describing high-order harmonics generation, is tested.

None of the aforementioned sources have the same intensity, coherence or possibility to be controlled as conventional lasers. Instead, these sources excel within their own parameter space. Our experiments aim to push these techniques to cover the gaps where none of these sources currently can be used.

Contents

Scientific publications and the author's contributions

Paper I: Harmonic dipole phase reconstruction by chirping the fundamental driving laser

N. Ibrakovic, S. Ek, E. R. Simpson, S. Bengtsson, A. Olofsson and J. Mauritsson.
Manuscript in preparation

This paper tests the validity of a technique for retrieving the intensity dependent dipole phase in HHG by chirping the IR laser beam. In this paper we also model the off-axis interference which we see in our experiments for the first time. I was involved in constructing the lab, procuring and assembling most of the equipment for the laser setup. I designed and assembled the HHG setup. The measurements in the paper were performed by me and S. Ek. The Gaussian beam code was originally written by Jana Preclíková, the code was adapted for three source terms by S. Ek and me. I wrote major parts of the manuscript.

Paper II: Probing Stark-induced nonlinear phase variation with opto-optical modulation

E. R. Simpson, M. Labeye, S. Camp, **N. Ibrakovic**, S. Bengtsson, A. Olofsson, K. J. Schafer, M. B. Gaarde and J. Mauritsson.
Physical Review A, **100**, 023403 (2019)

In this paper we demonstrate a measurement of the nonlinear AC-Stark shift of the Helium 1s2p state. The measurements are reproduced in a geometrical propagation code including TDSE calculated phase shifts. The opto-optical modulation experiments were the first experiments i participated in when i started my PhD studies. I participated in the measurements, the initial analysis of the measurement data and discussions for the manuscript.

Paper III: Attosecond pulse shaping using a seeded Free Electron Laser

P. K. Maroju, C. Grazioli, M. Di Fraia, M. Moioli, D. Ertel, H. Ahmadi, O. Plekan, P. Finetti, E. Allaria, L. Giannessi, G. De Ninno, C. Spezzani, G. Penco, A. Demidovich, M. Danailov, R. Borghes, G. Kourousias, C. E. D. Reis, D. Billé, A. A. Lutman, R. J. Squibb, R. Feifel, P. Carpeggiani, M. Reduzzi, T. Mazza, M. Meyer, S. Bengtsson, **N. Ibrakovic**, E. R. Simpson, J. Mauritsson, T. Csizmadia, M. Dumergue, S. Kühn, N. G. Harshitha, D. You, K. Ueda, M. Labeye, J. E. Baekhoj, K. J. Schafer, E. V. Gryzlova, A. N. Grum-Grzhimailo, K. C. Price, C. Callegari and G. Sansone.
Accepted for publication in Nature

This paper demonstrates waveform synthesis of sub-femtosecond pulse structures in a FEL, retrieved using a novel method for reconstructing the temporal structures. I was involved in the data analysis during the experiment and contributed to the manuscript by feedback.

Paper IV: Unexpected Sensitivity of Nitrogen Ions Superradiant Emission on Pump Laser Wavelength and Duration

Y. Liu, P. Ding, **N. Ibrakovic**, S. Bengtsson, S. Chen, R. Danylo, E. R. Simpson, and E. W. Larsen, X. Zhang, Z. Fan, A. Houard, J. Mauritsson, A. L'Huillier, C. L. Arnold, S. Zhuang, V. Tikhonchuk, and A. Mysyrowicz
Physical Review Letters, **119**, 203205 (2017)

In this paper, a semi-classical interpretation for the Nitrogen ion "lasing" is tested. The experiments performed for this paper measure the pump laser duration dependence of the 391 nm lasing signal. I took part in the preparation, experimental measurements and discussions for the manuscript.

Paper V: Achromatic dual-waveplate for inline two color high-order harmonic generation

N. Ibrakovic, E. W. Larsen, G. Zinner and J. Mauritsson.
European Journal of Physics D, **72:148** (2018)

This paper presents a waveplate designed for broadband pulses centered at 650- and 1300 nm. The waveplate works as a full- and half-waveplate at the respective wavelengths, and is intended for aligning the polarization of the pulses in order to perform two-color harmonics generation. I was involved in simulating the polarization characteristics of the waveplate and writing major parts of the manuscript.

List of acronyms

AOM	Acousto-Optic Modulator
CPA	Chirped Pulse Amplification
CW	Continuous Wave
EWP	Electron Wave-Packet
FEL	Free Electron Laser
FWHM	Full Width at Half Maximum
HHG	High-order Harmonic Generation
IR	Infrared
MCP	Multi-Channel Plate
OOM	Opto-Optical Modulation
QPI	Quantum Path Interference
SASE	Self-Amplified Spontaneous Emission
SFA	Strong Field Approximation
SHG	Second Harmonic Generation
TDSE	Time-dependent Schrödinger Equation
UV	Ultraviolet
VUV	Vacuum-Ultraviolet
XUV	Extreme Ultraviolet

Populärvetenskaplig sammanfattning på svenska

Vi kontrollerar och styr ljus varje dag. Vi använder oss av glasögon och förstoringsglas för att se bättre. Vi använder oss av speglar för att se förbi hinder eller för att se oss själva. Men tänk om inget material släppte igenom eller reflekterade ljus, och ingen av dessa uppfinningarna fungerade. Detta är vad som händer när fotonernas våglängd blir kortare än vakuum-ultraviolet, då absorberas dessa fotoner i de flesta material.

"-Men det är väl inte hela världen?", kanske man tänker. Vi har ju aldrig sett det här"vakuum-ultravioletta" ljuset med våra egna ögon, sant, men det betyder inte att det inte påverkar våra liv. För industriella tillämpningar så är fotoner med kort våglängd, ända nere i den extremt ultravioletta (XUV) regimen, väldigt intressanta. I mikrolitografi så avgör fotonernas våglängd hur små sturkturer vi kan tillverka. Sedan början av 90-talet så har våglängden som används i denna teknik gått från en mikrometer ($1\mu m = 10^{-6}$m)) till ungefär 10 nanometer ($1\,nm = 10^{-9}$m)) idag, en reduktion på en faktor 100. Detta är en av anledningarna till att vi idag kan gå runt med 90-talets motsvarighet till superdatorer i våra fickor. Inom grundforskning används ljus i detta våglängdsområde bland annat för att generera väldigt korta ljuspulser. Pulserna är så korta så att de lämpar sig för att studera elektronernas dynamik i atomer och molekyler.

Men hur gör man allt detta när linser och speglar bara absorberar de mesta av ljuset? Det finns många tekniker där man försöker komma runt detta problemet, men oftast brukar de brukar fortfarande innebära stora förluster av strålningen.

I mitt avhandlingsarbete har jag främst arbetat med *hög övertonsgenerering*. I övertonsgenerering utnyttjas en infraröd laser till att jonisera atomerna i en gas, och sedan accelerera elektronerna tillbaka till jonen. Om elektronerna rekombinerar med jonen genereras XUV-strålning. En stor del av arbetet handlar om hur man kan kontrollera XUV ljusets egenskaper när det genereras, och hur man kan kontrollera det kortvågiga ljuset efter det har genererats.

Under genereringsprocessen finns det flera vägar elektronerna kan ta till jonen. Eftersom elektronen är en kvantpartikel, och flera av dessa kvantvägarna kan bidra till samma fotonenergi för den utsända strålningen uppstår interferens, detta fenomen kallas *kvantbaneinterferens*. Genom att studera denna interferensen kan vi mäta vad elektronerna gör i övertonsgenereringsprocessen, men vi kan dessutom kontrollera hur ljuset sänds ut från atomerna.

För att styra XUV ljuset efter det har genererats kan vi använda oss av en teknik som kallas opto-optisk modulering (OOM). Då fokuserar vi först XUV ljuset i en gas där den absorberas under en kort tid. Medans ljuset är absorberat i gasen skickar vi en infraröd styrpuls för att kontrollera XUV ljuset. Detta gör att vi kan skräddarsy vågfronten, och därmed ut-

bredningsriktningen av XUV ljuset när det sänds ut igen. Kan vi kontrollera vågfronten av XUV ljuset så kan vi fokusera, dela eller rikta om XUV luset. Förutom att styra ljuset ger denna metoden insikt i hur atomens energinivåer skiftas på grund av styrpulsen.

Dessa kontrollteknikerna låter oss både utveckla nya metoder för att kontrolla XUV-strålning samt att studera elektrondynamiken i atomer. I dagsläget har vi bara demonstrerat att dessa formerna av kontroll är möjliga att åstadkomma, men min förhoppning är att de i framtiden kan utvecklas och lösa problem som idag inte har praktiska lösningar.

Chapter 1

Introduction

This thesis deals with various techniques for coherent manipulation of the properties of ultraviolet- to extreme ultraviolet light (XUV). The experiments performed in the thesis work use apparatus for which the size and complexity range from user-friendly turnkey table-top laser systems to state-of-the-art large scale free electron laser (FEL) facilities.

The invention of the laser in 1960 [1] is considered to be a milestone for scientific and industrial developments. The laser provides a source of intense, highly coherent radiation, where both the intensity and the phase of the light can be controlled. The coherent properties of the laser light allows for producing short pulses, which can be used either for time-resolved techniques [2], or non-linear optical processes, as these short pulses provide a high peak intensity [3]. By the 1990's, femtosecond ($1 \cdot 10^{-15}$ s) laser systems were demonstrated [4], in which the time-scale suitable for studying molecular dynamics. Today, conventional lasers can still only operate in the visible- and infrared (IR) regimes and with down to femtosecond pulse durations. Generating much shorter wavelengths than for the visible range using conventional lasers is problematic, as at some point most materials become absorptive in the vacuum-ultraviolet (VUV) regime. Techniques such as capillary discharge x-ray lasers [5, 6] and solid slab x-ray lasers [7] fall short as they can only reliably produce narrowband radiation and nanosecond ($1 \cdot 10^{-9}$)- to picosecond ($1 \cdot 10^{-12}$) pulse durations. Currently, there are other sources than lasers, that can produce femtosecond pulses with photon energies higher than VUV, although the amount of control that can be exerted from these sources, is far from what is possible in the visible and IR regimes.

In the thesis work, experiments have been performed using three kinds of UV- to XUV-sources: High Order Harmonics Generation (HHG) [8, 9], FELs and nitrogen air lasing. These three sources are based on physical phenomena that differ from lasing for the generation of coherent UV-XUV radiation.

HHG can be produced by using in-house lasers. The laser pulses are focused into a gas target in a small table top setup, generating a large bandwidth of coherent radiation. Photon energies produced with this technique can reach the soft x-ray regime [10]. The spectrum can be compressed to a train of attosecond ($1 \cdot 10^{-18}$ s) pulses [11, 12], or single isolated attosecond pulses [13, 14], and used to probe electron dynamics in atoms [15]. Currently, HHG is the process that produces the largest coherent bandwidth [16] and generates the shortest possible pulse durations [17], but the downside is that the flux of XUV radiation is very low compared to other sources.

FELs, as the name suggests, generate radiation from unbound electron bunches that are accelerated to relativistic velocities and forced through magnetic insertion devices to oscillate. During oscillation, the electron bunches emit coherent radiation, tunable across a large bandwidth [18]. To reach high photon energies, however, FEL–facilities have to be very large in order to accelerate the electron to sufficient velocities [19]. In addition, the generation process is stochastic, causing a large shot-to-shot variation. To decrease the fluctuations and jitter in FELs, it is possible to seed an FEL with a femtosecond (10^{-15}s) laser, imprinting the laser's coherence onto the electron bunches [20, 21]. Still, the emitted radiation does not have bandwidths, pulse durations, coherences, or fluctuation stabilities comparable with those from HHG. FELs, however, provide unprecedented flux and wavelength tunability across a large spectral region.

Nitrogen air lasing is the least understood of the techniques presented here. When focusing a high intensity femtosecond IR laser in nitrogen, under certain circumstances, part of the laser energy will convert into coherent radiation at 391 nm, corresponding to a resonance in molecular nitrogen [22]. In addition, this UV pulse is not only emitted forward together with the IR pulse, but also backwards towards the source, making it ideal for remote sensing [23].

In all of these techniques, the spatial and temporal coherence is imprinted by a conventional laser, and subsequently, the properties of emitted radiation can be tailored and controlled by changing the properties of the laser source [11, 24]. The manipulation of conventional laser sources is well established, such that the properties of IR laser pulses can be altered to a high degree of control. What this work mainly strives for is to determine how much control can be transferred from our IR beams onto the XUV beam.

1.1 Aim of this work

The aim of this work is to demonstrate spatio-temporal control of UV-XUV radiation during and after its generation. Since these techniques rely on physical processes which today are not completely understood, we also probe the intrinsic dynamics of the techniques in

the experiments.

HHG experiments with two different experimental setups were carried out. One HHG setup was built, to be used with a commercial variable rep-rate turnkey laser. This laser has a very stable output power, making it ideal for measuring the interference between two quantum trajectories of these harmonics (*cf.***Paper I**). These results showed that it is possible to assert control of the intensity-dependent dipole phase in HHG by changing the intensity of the IR driving pulse. The second setup involved the use of a pump-probe interferometer, where an XUV pulse was resonantly absorbed in a gas cell, and a second IR control pulse stark shifted the atomic resonance and imprinted an intensity-dependent phase onto the emitted XUV beam [25, 26]. **Paper II** describes the probing of the intensity-dependent Stark shift of the helium 2p state, and demonstrated that this state can be used as an effective XUV beam splitter. Both of these papers aimed to demonstrate control of the XUV wavefront during- and after the generation process by using IR light.

The experiments presented in **Paper III** were performed at the FERMI free electron laser at Elletra Sincrotrone in Trieste. At this facility it is possible to generate harmonics of the fundamental FEL beam, and the aim of the experiment was to demonstrate that changing the phase of these harmonics enables short-pulse generation as they are phase-locked. The results demonstrate that it is possible to perform XUV waveform synthesis by changing the phase between the harmonics.

Paper IV evaluates an interpretation of the source of the 391 nm nitrogen air lasing radiation. As it is not known why nitrogen air lasing occurs, a proposed recollision model [27] was tested as the source of energy and coherence transfer from the 800 nm IR beam to the 391 nm air lasing beam.

Paper V describes a custom-made, achromatic waveplate intended for inline, parallel polarized, two-color HHG [28, 29]. An inline configuration is more stable than a split-beam configuration, but it is limited by the bandwidth of the optics. With the achromatic waveplate described in **Paper V**, few cycles pulses can be used in an inline configuration.

1.2 Outline of the thesis

Chapter 2 of this thesis lays out the foundation of the techniques used in this work. We start by describing femtosecond lasers, which are the enabling tool, and the source of the coherence, for all our techniques. The semi-classical mechanics of the HHG process are presented followed by a brief introduction of FELs. Chapter 3 expands on the spatio-temporal control techniques. Quantum path interference and opto-optical modulation are explained for the HHG experiments. The control of XUV waveforms are described for the FEL experiment, and the experiments and interpretation of the nitrogen air lasing is

discussed. Chapter 4 summarizes the findings from all the experiments.

Chapter 2

Short-pulse light sources

This chapter introduces the conceptual background for lasers, HHG and FELs, and also describes the setups used for the experiments discussed later. As all of the work presented in this thesis relies on short light pulses, necessary theory describing their generation is introduced.

The benefit of short-pulse light sources can be considered to be two-fold. On the one hand, the pulses have a short duration, and therefore provide a good temporal resolution in experiments. On the other hand, short pulse light sources generally have a high peak intensity, as the average output energy of the source is confined to a very short duration. Regardless of the reason for generating short light pulses there are physical restrictions for how short the pulses can be made. The first, and the most intuitive restriction, is that the duration of a pulse can not be shorter than a single optical cycle. This means that our choice of wavelength, λ, determines what the shortest possible pulse duration is. Secondly, the duration of an electromagnetic pulse is inversely proportional to the frequency bandwidth of the pulse, and this relation depends on the shape of the pulse. If we consider a Gaussian spectrum, with a full width at half maximum (FWHM) bandwidth $\Delta\nu$, then the shortest possible pulse duration, τ, is given by the time-bandwidth product:

$$\tau = \frac{0.44}{\Delta\nu}. \tag{2.1}$$

The time-bandwidth product is directly related to the wave nature of light, and is illustrated in Fig. 2.1. For a monochromatic spectrum the pulse duration is infinite, *i.e.* it is not pulsed at all, and lasers which produce monochromatic light are denoted as continuous wave (CW) lasers. In the middle panel in Fig. 2.1, two more monochromatic peaks are added to the spectrum. The waves will now periodically interfere constructively, producing a

train of pulses. In the bottom panel we instead have a full Gaussian spectral distribution, the resulting waveform is now an isolated pulse. At this point we could extend the bandwidth of our spectrum, although the lower limit of the pulse duration would be a single cycle of our central frequency.

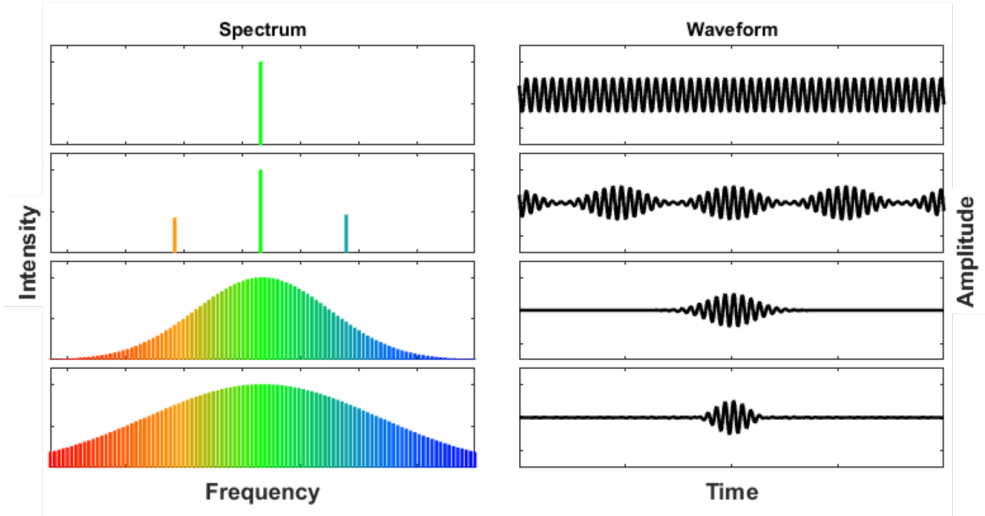

Figure 2.1: Illustration of the spectro-temporal relations of electromagnetic waveforms. The left columns represent a frequency spectrum, and the right columns show the corresponding temporal waveform for the given spectrum. The first row shows a single frequency component, the resulting waveform is infinitely long. In the second row, several spectrally separated peaks combine to create a train of pulses. Third row: a continous distribution yields an isolated waveform in time. Bottom row: the larger the frequency bandwidth is, the shorter the waveform can become.

A broadband pulse is, however, not automatically short. For short pulse generation, aside from producing a broad spectrum, it is important to ensure that the bandwidth is coherent and that the spectral components arrive simultaneously. The latter requirement becomes more important the broader the bandwidth becomes, as different wavelengths generally have different phase velocities in different dielectric media, a phenomena known as *dispersion*. It is therefore important for the spectral components to have the right phase, in order to obtain short pulses.

2.1 Femtosecond lasers

With conventional lasers it is possible to reach the femtosecond regime. Since these lasers rely on bulk material for amplification of the laser radiation it is the spectroscopic properties

of the bulk material that limit the bandwidth of the amplification process. Today, the most widely used medium for femtosecond lasers is titanium sapphire (Ti:Al_2O_3), or Ti:Sapphire [30], which has a gain bandwidth of almost 400 nm, centered at 800 nm. The entire gain bandwidth of Ti:Sapphire is, however, not usable in most setups, since the reflectivity of the cavity mirrors can not cover such a large bandwidth. The output of Ti:Sapphire lasers is instead limited to a few tens of femtoseconds, which corresponds to a few tens of optical cycles.

Even though Ti:Sapphire lasers can produce the required bandwidth for femtosecond pulses it is not possible to directly amplify these pulses in the gain medium, as the pulses can reach intensities that may damage the gain medium. In order to avoid burning and dielectric breakdown in the Ti:Sapphire crystal, chirped pulse amplification (CPA) [31] is used, where the pulses are temporally stretched before they are amplified in the gain medium.

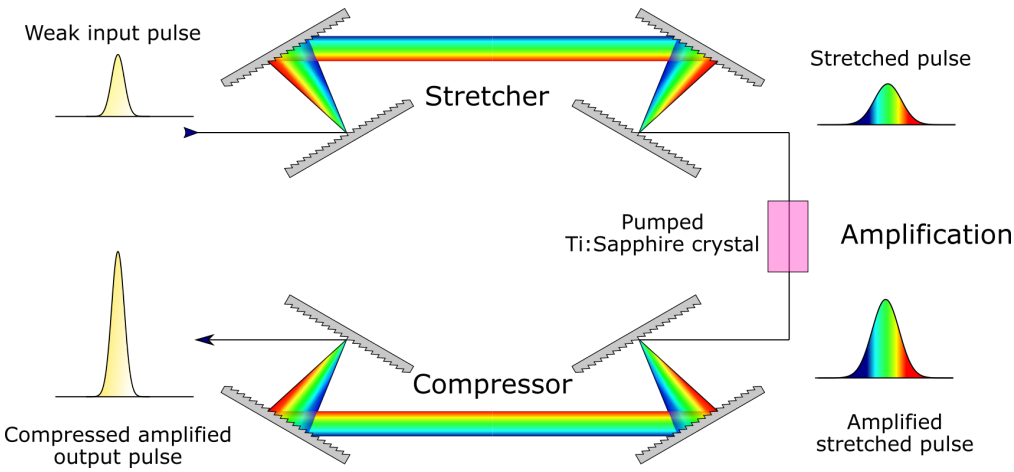

Figure 2.2: Illustration of the CPA technique. A weak input pulse is stretched in time using a grating compressor. The stretched pulse may be amplified without the risk of damaging the Ti:Sapphire crystal. The long amplified pulse is compressed after passing through a grating compressor. The resulting pulses have a short duration and a high peak intensity.

The schematic in Figure 2.2 illustrates a typical routine for CPA. Weak input pulses, from, for example, an oscillator are first temporally stretched, usually to a few picoseconds in a grating stretcher. These long pulses are then amplified in a Ti:Sapphire crystal (population inversion in these crystals is achieved using pump lasers), and then compressed in a grating compressor.

For most of our experiments, two laser systems were used: An ytterbium based laser, and a Ti:Sapphire laser. The specifications of the lasers is briefly discussed below.

2.1.1 Ytterbium laser

The ytterbium laser, also called the Pharos, is a commercial turnkey laser system from Light Conversion Ltd., based on ytterbium potassium gadolinium tungstate (Yb:KGW) as the amplification medium. The Pharos produces a 5-7 W (depending on the repetition rate) average output power, with a repetition rate that varies between 1 and 200 kHz. The output wavelength is centered at 1030 nm with ∼10 nm bandwidth, producing 180 fs FWHM pulses. The energy of the pulses varies from 1 mJ to 33 µJ. The Pharos laser has a built in pulse picker and attenuator, making it possible to obtain different combinations of pulse power and average power.

Even though the specifications of the Pharos laser at first might seem unattractive for ultrafast experiments, the Pharos comes with an upside: robustness. The Pharos is primarily designed for industrial use, where sometimes the laser has to operate for extended periods of time without any drift of the output power. The long, narrowband pulses are insensitive to dispersion effects during propagation or vibrations in the compressor. From a practical point of view, the laser is easy to start, maintain and operate, as it is intended to be used by non laser experts, meaning that the experimental problems encountered are shifted down the beamline closer to the experiment, rather than at the source.

2.1.2 Ti:Sapphire laser

The laser in the "Attolab" is a custom-built Ti:Sapphire laser system, operating at 1 kHz and centered at 800 nm. The laser produces 20 fs pulses with ∼ 4mJ pulse energy.

The system is seeded by a Ti:Sapphire oscillator (Rainbow VI, Femotlaser), which produces 7 fs, 2 nJ pulses with a 300 nm bandwidth at a 78 MHz repetition rate. Before the seed enters the amplification stages the bandwidth is reduced to 100 nm due to the reflectivity of dielectric mirrors after the oscillator. The seed is amplified in four Ti:Sapphire amplification stages. The Ti:Sapphire crystals are pumped by two Neodymium-doped yttrium lithium fluoride (Nd:YLF) lasers at 527 nm, a "Photonics DM 30-527" laser and a "Continuum Terra laser".

The laser system uses acousto-optic modulators [32] (AOM) to shape and reconstruct the spectral phase and amplitude of the laser pulses. Three AOMs are used in total. The first AOM is placed after the stretcher in the laser system to ensure a flat spectral amplitude before the seed is sent to amplification (Dazzler, Fastlite). The second AOM is positioned in the third amplification stage in order to counter gain narrowing during the amplification (Mazzler, Fastlite). The third AOM is used to reconstruct the spectral profile of the pulses at the laser output (Wizzler, Fastlite). The spectral reconstruction with the Wizzler includes higher dispersion orders, which can be fed back to the Dazzler to pre-compensate

before the amplification chain. The Wizzler and Dazzler can therefore actively measure and shape the phase profile of the pulses. Besides removing higher-order dispersions to produce transform-limited pulses, the Dazzler can truncate the bandwidth of the pulses to 50 nm, and by doing so makes it possible to have 40 fs pulses, where the central wavelength is tunable between 780-820 nm.

2.2 High-Order Harmonic Generation

Lasers can produce many different wavelengths, ranging from the mid infrared [33, 34] to the UV regime [35]. There are, however, no high-power lasers sources that operate in the VUV regime. Since materials absorb most radiation in this regime, the working principle for conventional lasers can not be used.

In the late 80's, a promising candidate for an alternative source of coherent sub-VUV radiation was found. Two independent research groups measured a spectral plateau of XUV radiation when focusing IR laser pulses into a gas target [8, 9]. The spectrum consisted of odd harmonic orders of the IR laser. From the previous understanding of perturbative harmonic generation[3] it was unexpected that the yield of the harmonics would exhibit a plateau, or any measureable signal at such high orders. Today we know that this process is different from perturbative harmonic generation and it is called high-order harmonic generation (HHG).

2.2.1 Three-step model

HHG requires high intensities of the laser pulses. When the electric field of the laser beam is comparable in strength to that of the electrostatic attraction of the electron and the nucleus in the target gas, quantum tunneling becomes probable. By the early 90's, an intuitive semi-classical three-step model was proposed to explain the phenomenon [36, 37]. The tunnel-ionization and recombination can not be explained classically, but the propagation of the tunneled particle can:

(I) An atom is subjugated to the electric field of the laser pulse. The laser field distorts the potential binding the outermost electron to the nucleus, forming a barrier. Part of the electron wave-packet (EWP) may tunnel out through the barrier, *cf.* Figure. 2.3.

(II) The free EWP is accelerated away from the parent ion in the continuum. During the excursion the wavepacket spreads.

(III) When the driving field changes sign, the freed EWP is retarded and may be accelerated back to the nucleus, gaining kinetic energy. When it returns to the ion, part of

the EWP may recombine. The excess energy from acceleration is released as high-energy photons.

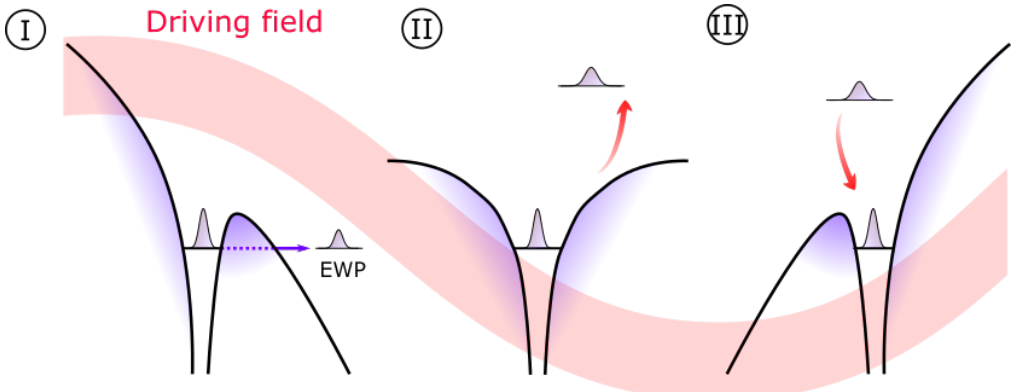

Figure 2.3: Illustration of the three step model for HHG. The laser field (red line) distorts the atomic potential (black line), allowing part of the EWP to tunnel out. The freed EWP part is accelerated away from the nucleus, once the laser field changes sign it may be accelerated back. Part of the EWP may recombine with the ion, the excess energy is released as high energy photons.

HHG is more accurately described by Lewenstein *et. al* in the strong field approximation (SFA) [38] model, where the full harmonic spectrum is released during the recombination of the EWP. Since the wavepacket spreads during the propagation step, there are different ionization- and return times for different parts of the EWP. The freed EWP then contains a continuum of kinetic return energies. In the acceleration step, the various parts of the EWP are therefore considered to travel along different *quantum paths*. A more intuitive picture, however, can be constructed if we consider the EWP to be an electron that has tunneled out, and that follows a classical *trajectory* in the driving field.

We can assume that the electron, once it has tunneled out into the continuum, is a free particle that is only influenced by the external electric field. The acceleration of the electron is then given by:

$$\ddot{x} = -\frac{eE_0}{m_e}\sin(\omega_0 t), \tag{2.2}$$

where E_0 and ω_0 are respectively the electric field strength and wavelength of the IR laser pulse, e and m_e is the charge and mass of the electron. The velocity at any given time is then given by:

$$\dot{x} = \frac{eE_0}{m_e\omega_0}\left[\cos(\omega_0 t) - \cos(\omega_0 t_i)\right], \tag{2.3}$$

introducing the time of tunnel-ionization t_i. Integrating the expression again gives the displacement of the electron as a function of time:

$$x = \frac{eE_0}{m_e\omega_0^2}\left[\sin(\omega_0 t) - \sin(\omega_0 t_i) - \omega_0(t - t_i)\cos(\omega_0 t_i)\right]. \tag{2.4}$$

By using Eq. 2.4 it is possible to calculate the trajectories of the electrons, as a function of the time of tunnel-ionization, Fig. 2.4 (a). For each of the trajectories we assign a corresponding return time, $\mathrm{t_r}$, when the electron returns to the ion. Provided that we have the time of ionization, $\mathrm{t_i}$ and time of recombination, $\mathrm{t_r}$, we can calculate the amount of kinetic energy, E_k, accumulated during this excursion:

$$E_k = \frac{1}{2}m_e\dot{x}^2 = \frac{e^2E_0^2}{m_e^2\omega_0^2}\left[\cos(\omega_0 t_r) - \cos(\omega_0 t_i)\right]^2. \tag{2.5}$$

The constants the rightmost term of Eq.2.5 are rewritten as; U_p, the *ponderomotive energy*, *i.e.*, the kinetic energy acquired by a free particle in an electric field:

$$U_p = \frac{e^2\lambda^2 I}{8\pi^2 m_e\epsilon_o c^3}. \tag{2.6}$$

Here, λ is the wavelength of the driving laser, I is the peak intensity of the laser pulses, c is the vacuum speed of light and ϵ_0 is the vacuum permittivity.

The trajectories in Fig. 2.4 (a) are color-coded to display the distribution of return energies accumulated in the acceleration step. It is apparent that there are always two trajectories within a single half-cycle leading to the same final energy. For obvious reasons these two trajectories are referred to as the *long* and the *short* trajectory, corresponding to the time duration they spend in the continuum. The kinetic behavior of the electron trajectories is illustrated in Fig. 2.4 (b), the classical interpretation is that the shortest trajectories do not accumulate any kinetic energy in the continuum as they immediately recombine after tunneling. The longest trajectories do not accumulate any kinetic energy either, as they spend a full laser cycle in the continuum, wherefore the net acceleration amounts to zero.

The largest possible kinetic energy, that can be acquired is $3.17U_p$, which is found for electrons spending $\sim$ 0.65 cycles in the driving laser field. These electrons are born at

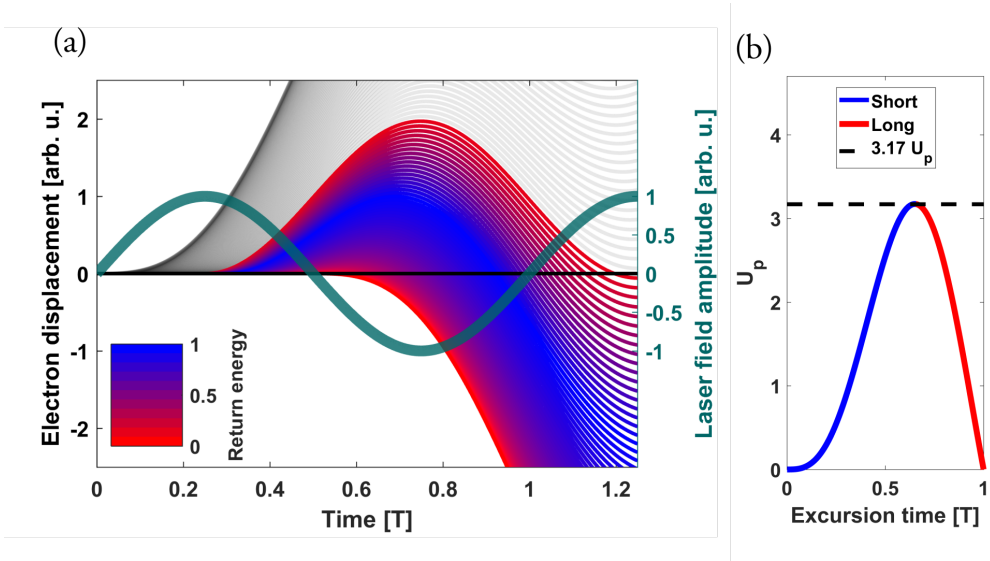

Figure 2.4: (a) Classically calculated electron trajectories as a function of laser period T. The trajectories are released during the first half of the driving field laser cycle $0 < T < 0.5$. The trajectories are color coded to display return energy for each tunneling time. Grey trajectories never return to the parent ion. (b) Return energy of the different trajectories as a function of their excursion times, showing two classes of trajectories leading to the same energy. The highest energy is 3.17 U_p, where U_p is the ponderomotive energy.

approximately $T/3$. The total energy of the emitted photon is then the sum of the accumulated kinetic energy, and the ionization potential of the atom, I_p. The highest possible photon energy, also called the harmonic *cut-off* [39], predicted by the semi-classical three step model is:

$$E_{max} = 3.17 U_p + I_p. \tag{2.7}$$

Multi-periodic effects

For all trajectories within a single half-cycle, the three-step model predicts a continuum of possible energies produced by the returning electrons. This is indeed true for single cycle pulses, however, for multi-cycle pulses we have consecutive generation events. These events introduce an additional interference effect, producing discrete harmonics of the fundamental driving field. In an isotropic medium, such as gas, while the odd-order harmonics of the fundamental driving field interferes constructively, the even orders interfere destructively. This occurrence of discrete harmonics can not be explained with the classical electron

picture. Instead, we have to consider the wave nature of the EWP.

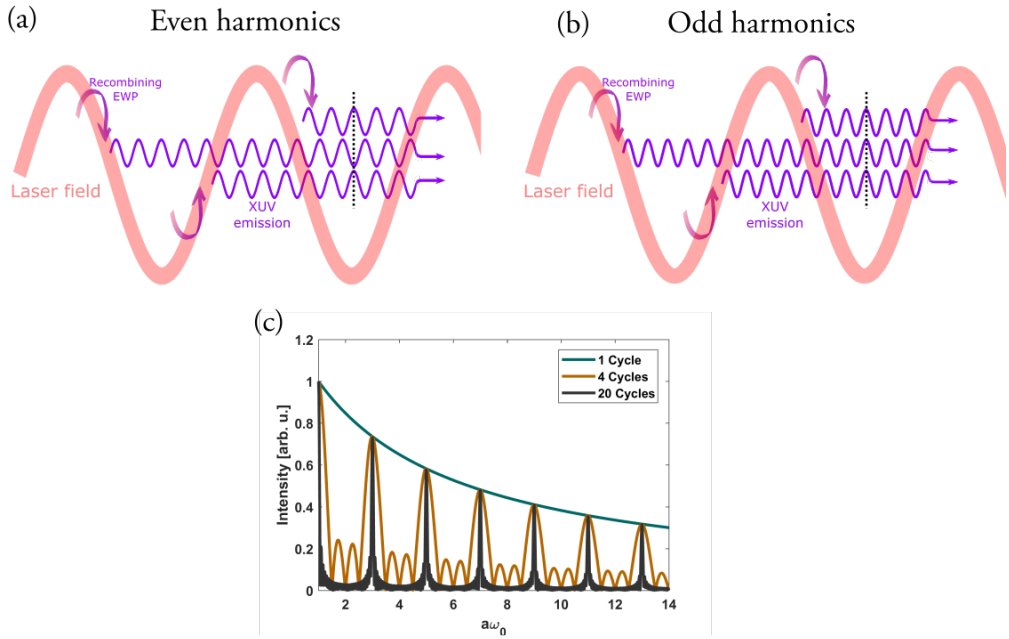

Figure 2.5: (a) Illustration of the phase relation of even harmonics during consecutive half-cycle recombination events. (b) Calculation of the spectral bandwidth of harmonics, generated for 1, 4 and 20 cycles.

From Fig. 2.4 it becomes apparent that a certain emitted photon energy originates from a specific trajectory, with specific t_i and t_r. During each cycle there are two tunnel-ionization time windows of the EWP, in opposite directions. When the second recombination event occurs in the following cycle, the emitted XUV radiation is π-shifted due to the reversed sign of the driving field. For even harmonics, the phase shift solely due to the distance between the two generation events corresponds to πn, where n is the order of the even harmonic. Including the π-shift from the driving field sign change ensures that consecutive emission events of the even-order harmonics are always out of phase, shown in Fig. 2.5 (a). For the odd-order harmonics, the opposite is true. Here, the spacing between two consecutive events is always out of phase, $(2n + 1)\pi$, and adding the π-shift from field inversion consistently gives a constructive interference, *cf.* Fig. 2.5 (b).

The number of cycles contained in the laser pulse generating the harmonics determines the spectral width of the harmonics in the spectrum. We can qualitatively evaluate the cycle dependent electric field $\tilde{E}_{tot}$ by calculating following equation:

$$\tilde{E}_{tot}(t) = E_0 e^{ia\omega_0 t} \sum_{b=0}^{n-1} e^{ia\omega_0 bT/2} e^{ib\pi}, \tag{2.8}$$

where b is the number of cycles contained in the pulse, $a\omega_0$ is the photon energy of which we are evaluating the intensity of and T is the cycle duration.

The result of Eq. 2.8 for 1, 4 and 20 cycles is illustrated in Fig. 2.5 (c). As observed, a single cycle pulse produces a continuous spectrum whereas additional cycles narrow the bandwidth of the individual harmonics. The resulting frequency comb which is generated will produce a train of pulses. This generated frequency comb is still extremely broad, and the pulses in the train can reach attosecond durations.

2.2.2 Two-color HHG

An inversion-symmetric HHG would produce only odd harmonic orders. The generate of even orders requires that either the inversion symmetry of the generation medium or the generating electric field is broken. One method to generate even-order harmonics through HHG is by mixing the driving laser field with its second harmonic [40–46]. The second harmonic can enhance the electric field of the fundamental in one direction and suppress the electric field in the opposite direction. In the resulting modulated electric field, ionization and return times are separated by a full cycle of the fundamental driving field, and the harmonics from consecutive events are then spaced by $2\pi n$, allowing for the generation of both odd- and even order harmonics.

Paper V describes an achromatic waveplate designed for two-color HHG in an inline configuration, using broadband laser pulses. The fundamental and the second harmonic pulses are centered at 1300 nm and 650 nm respectively. In contrast to an interferometric configuration, the inline configuration is inherently more stable as the phase of the fundamental and second harmonic shift together due to any vibrations or changes to the optics in the setup. An inline setup, however, relies more on material properties of the optics in the setup. Two key components in this setup are: a nonlinear crystal for producing an orthogonal second harmonic of the fundamental through second harmonic generation (SHG), and a waveplate to create parallel alignment the polarization of the fundamental and its second harmonic. To accommodate for broadband pulses, the SHG crystal is thin in order to have a broad phase-matching bandwidth. The solution for the waveplate is not as straightforward. Instead its composition and dimensions are the result of a numerical optimization problem. The study in **Paper V** therefore focuses on comparing the experimental and theoretical polarization characteristics of this composite waveplate.

The final state of polarization, after the light has passed through the achromatic waveplate,

was measured by placing the waveplate between two parallel polarizers and measuring the transmission of white light through this setup. The resulting spectrum displayed a 100 nm plateau of transmission centered at 650 nm and a 300 nm plateau centered at 1300 nm. The experiment was reproduced using Jones calculus [47], and excellent agreement was found between the output spectra. The comparison, however, does not account for any potential temporal distortions of the pulses intended to be used with this waveplate. Therefore an experiment using short pulses at the intended wavelengths must still be performed in order to fully demonstrate the functionality of this achromatic waveplate.

2.2.3 Yield and spectrum

One of the main disadvantages of HHG is the conversion efficiency. This is an inherent problem to the generation process itself, as there are several phenomena involved that give rise to a reduced conversion efficiency.

- The IR driving field may never become depleted: HHG relies on a strong external field that is enabling tunnel-ionization. For an extremely nonlinear process like HHG, a minor loss of IR energy corresponds to a huge loss in tunneling efficiency.
- A part of the EWP has to remain bound in order for the process to be coherent, meaning that only part of it may tunnel out. During the excursion the tunneled wavepacket will spread, and upon returning only a fraction of the EWP can recombine.
- Throughout the entire generation process the medium will be continuously ionized, reducing the number of atoms participating in the process and once the XUV is generated it will be reabsorbed while propagating in the generation medium.

In addition, only part of the radiation will interfere constructively. This topic is in more detail in the next section. A rough estimation, for an 800 nm central wavelength driving laser generating harmonics in argon, is that an intensity of $10^{14}\mathrm{W/cm^2}$ is optimal when balancing tunneling efficiency versus ionization losses. Expected peak conversion efficiencies for the plateau harmonics can reach 10^{-5} of the input energy, and the harmonic cut-off is expected to reach 50-60 eV. Extending the cut-off further is possible. If we consider Eq. 2.7 there are two possibilities, either a gas with higher I_p can be used (for example, neon or helium), or the value of U_p can be increased. Increasing I_p does not only shift the harmonic spectrum by the energy difference of the gases, but also allows for generation with higher intensities as ionization losses are decreased.

In Eq. 2.6, the maximum value of U_p can be increased by raising the peak intensity of the pulses. However, this does introduce higher losses from ionization. In addition, it also

affects the phase-matching which is discussed in the next section. Alternatively, the more popular option is to use the favorable quadratic dependence of the wavelength [48, 49], where it becomes possible to reach photon energies spanning from hundreds- to thousands of eV [50, 51]. When the wavelength of the IR driving field is increased, the EWP spends more time accelerating in the continuum accumulating kinetic energy, but during this time the EWP spreads more, reducing the overlap with the ion when it recombines. Studies show that the yield of the HHG process scales as $\lambda^{-5} - \lambda^{-6}$ [52], demanding more laser power to compensate for this reduction in conversion efficiency.

2.2.4 Phase matching

The single atom response can give an intuitive interpretation of HHG, however, it is insufficient for describing efficient generation conditions in the lab. Instead, HHG must be treated as a macroscopic process. Since HHG takes place within an interaction volume, containing spatially separated emitters, it is important to ensure that the emission events add up coherently along the propagation axis, this is called phase matching. Normally, the phase matching criteria are described as an amount of mismatch, Δk, between the wave vectors of the driving laser beam and a specific harmonic. For HHG, Δk can be decomposed into four sources generating a mismatch of the wave vector [53]:

$$\Delta k = \Delta k_{\mathrm{g}} + \Delta k_{\mathrm{d}} + \Delta k_{\mathrm{n}} + \Delta k_{\mathrm{p}}, \tag{2.9}$$

where Δk_{g} is called the Gouy phase mismatch, Δk_{d} is the dipole phase mismatch, Δk_{n} is the phase mismatch due to neutral gas dispersion and Δk_{p} is the mismatch due to plasma dispersion.

The Gouy phase mismatch is a geometrical phase, introduced when focusing the driving laser. In general, there is a π phase shift (the beam is inverted) on the other side of the focus, but this shift occurs continuously across the focus. In the near field, the difference in Gouy phase shift between the fundamental beam and a q-th order harmonic can be expressed as:

$$\Delta k_{\mathrm{g}} = -\frac{q}{z_{\mathrm{R}}}, \tag{2.10}$$

where z_{R} is the Rayleigh length. The dipole phase mismatch comes from the generation process itself: each photon energy is born with a phase related to its specific EWP trajectory, and the trajectory is related to the intensity of the driving laser, I. A good approximation, for the plateau harmonics, is that this phase has a linear intensity dependence with an empirically retrieved slope α_{q} [54–56]. The offset between the driving laser and a harmonic, along the propagation direction z, is then given by:

$$\Delta k_{\mathrm{d}} = \alpha_{\mathrm{q}} \frac{\delta I}{\delta z}. \tag{2.11}$$

The neutral gas and plasma phase mismatch simply arises from the fundamental and harmonic velocity difference in the medium:

$$\Delta k_{\mathrm{n}} = q\frac{\omega}{c}(n_{\mathrm{f}} - n_{\mathrm{q}}), \tag{2.12}$$

$$\Delta k_{\mathrm{p}} = q\frac{\omega}{c}(n_{\mathrm{f}}^{\mathrm{e}} - n_{\mathrm{q}}^{\mathrm{e}}). \tag{2.13}$$

Here, n_{f} and n_{q} are the refractive index for the fundamental and the harmonic beam in the medium, respectively, n^{e} indicates the plasma refractive index in the medium and ω is the frequency of the fundamental beam. Ideally, the sum in Eq. 2.9 should be minimized for optimal phase matching, and this is usually achieved by tuning the IR pulse intensity and spot size, gas pressure at the target and the position of the focusing optic while monitoring the yield of XUV radiation.

2.3 Free electron lasers

Unlike lasers and HHG, FELs do not rely on the restrictions of any medium for generating radiation. Instead, FEL devices, as their name implies, generate radiation from free electrons. The electrons are accelerated to relativistic velocities and undulated in magnetic insertion devices. Since FELs do not rely on a medium for the generation and amplification of the light, they can therefore produce femtosecond pulses at higher intensities, compared to other sources.

An illustration of the operating principle is shown in Fig. 2.6. An electron bunch accelerated to relativistic velocities enters an undulator. The undulator consists of periodically poled permanent- or electromagnets. Due to the Lorentz force, the magnets exert a lateral force on the electrons causing them to oscillate as they propagate through the undulator. These oscillations induce synchrotron radiation in the propagation direction of the electrons. Initially, this emission is incoherent as the electrons in the bunches have no restrictions in how they emit their radiation. If the undulators spacing is set correctly, however, the radiation that is produced by the electron bunch will modulate the electron distribution.

This modulation of the electron distribution causes the electrons to form *microbunches*. Provided that the microbunches slip one wavelength period of the emitted radition during an oscillator period, the sum of consecutive emissions will interfere constructively. A

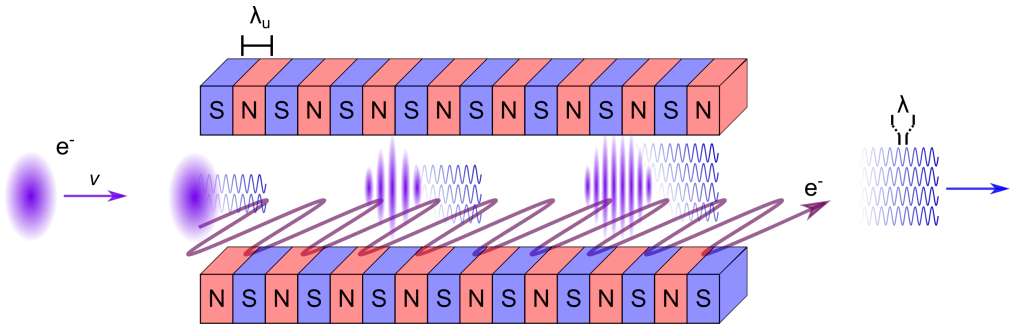

Figure 2.6: The principle of an FEL. An electron bunch, accelerated to relativistic velocities, enters an undulator. In the undulator, the electron bunch will begin oscillating and emitting radiation. The radiation causes the electron bunch to form microbunches that are resonant with the emitted radiation. The emitted radiation from the modulated electron bunch interferes more constructively, encouraging more microbunching. After passing the undulator, the electron bunch is deflected, and the radiation generated from the process travels forward towards an application chamber.

self-amplifying feedback occurs, the microbunching encourages more radiation to interfere constructively, the resulting increased flux causes the microbunches to bunch more, promoting an exponential increase in emission [57]. This mode of operation is denoted as Self-amplified spontaneous emission (SASE).

The wavelength of the FEL radiation, λ, depends on the undulator period, λ_u and the velocity of the electron bunch, v_e. In the lab frame, the oscillation period of the electron bunch is λ_u, however, in the frame of reference of the electrons, since they travel at relativistic velocities, they perceive a Lorentz contracted undulator period, λ:

$$\lambda = \frac{\lambda_u}{2\gamma}. \tag{2.14}$$

Here, γ is the Lorentz factor:

$$\gamma = \frac{1}{\sqrt{1 - \frac{v_e^2}{c^2}}}, \tag{2.15}$$

and c is the vacuum speed of light. Since the velocity of the electrons is so close to the speed of light, the electron kinetic energy is more commonly used. A rough estimate for XUV generation ($\lambda = 6\,\mathrm{nm}$) in an FEL are: 1 GeV electron beam energy and $\lambda_u = 2.7\,\mathrm{cm}$ [58]. The first demonstration of hard X-ray generation, $\lambda = 1.2$, required 13.6 GeV and $\lambda_u = 3\,\mathrm{cm}$ [59].

It is apparent that FELs demonstrate the possibility of generating high photon flux at very short wavelengths, even though FELs have a large shot-to-shot variation of the generated light pulses, compared with both lasers and HHG. Typically, in phase- and intensity sensitive experiments with FELs, each light pulse is "tagged" and the temporal waveform is reconstructed. In post-processing, only the shots within a certain variance of, for example, intensity or pulse duration are used. Since FELs typically have a repetition rate of a few tens of Hz, each measurement becomes time-consuming in order to gather enough statistical data.

2.3.1 Seeded free electron lasers

With the SASE technique, the onset of amplification is stochastic. The microbunching occurs inside the undulator, at a random time, causing each shot to vary with regard to amplification and phase. To counteract this random onset of amplification, a conventional laser can be used to seed the initial microbunching of the electrons: a mode of operation called a seeded FEL [21, 60]. In a seeded FEL, the electron bunch and the seeding laser co-propagate into an initial undulator, called a *modulator*. The electron bunch is modulated by the laser beam in a more controlled manner as compared to SASE, before it is sent for amplification in the main undulator line, denoted as the *radiator*.

The experiment described in **Paper III** was performed at the FEL-1 undulator line, at Fermi FEL, Elletra Sincrotrone, which is a seeded FEL operating in the XUV regime [61]. FEL-1 provides 50-100 fs pulses between 20-100 nm with up to 200 µJ pulse energy, at 10-50 Hz repetition rate. Part of the laser beam used for seeding can be split off and recombined with the FEL generated XUV at the experimental target, with a jitter between the beams close to 4 fs. Compared with SASE FELs, where the jitter is several tens or- even up to a hundred fs, 4 fs is in a regime where pump-probe spectroscopy can be performed more reliably. Compared with equivalent experiments with HHG, where jitter can be reduced down to a few tens of attoseconds, it still has a comparably low stability.

2.4 Conclusions

The sources described in this chapter are complementary to each other, and very dependent on the application. Conventional lasers have a very high degree of spatial and temporal coherence, can reach high peak intensities and their radiation can easily be manipulated using well-established optical components. For wavelengths shorter than VUV, or pulse durations below the femtosecond barrier, other sources have to be used. HHG can provide radiation with a very high spatial and temporal coherence, at wavelengths reaching the soft x-ray regime. The HHG technique is fairly inexpensive and therefore accessible. However,

the method suffers from low conversion efficiency and therefore low photon flux of the generated radiation.

FELs are a tunable source of high photon energy radiation, covering the VUV to hard x-ray regime, and producing a high photon flux. FELs, however, have a large shot-to-shot variation of the pulse duration and intensity. For two pulse experiments, FELs have a large jitter between the pulses used in the experiments, limiting the temporal resolution of these kinds of experiments.

Chapter 3

Spatio-temporal control techniques

In the previous chapter we discussed two different short pulse light sources operating at wavelengths shorter than the VUV regime: HHG and FELs. HHG produces very short pulses, and since they are generated by a laser there is a high degree of stability to the driving laser in interferometric experiments. HHG, however, has a very low conversion efficiency. FELs provide a large flux, they have a high degree of wavelength tunability, but are hard to synchronize with an external laser source and can not produce very short pulses.

The present chapter discusses techniques that control radiation from HHG and FELs. For HHG, we explore control of the spatio-temporal phase of the XUV radiation as it is generated using quantum path interference (QPI). We show how to control the XUV radiation after it is generated with HHG using an IR pulse, in a technique called opto-optical modulation (OOM). An experiment for producing and measuring sub-femtosecond pulses in an FEL is presented. Finally, experiments testing a recollision model for nitrogen air lasing is shown and discussed.

3.1 Quantum path interference

In HHG there are two electron quantum paths that result in the same final kinetic energy. However, the two parts of the EWP following these two paths spend unequal amounts of time in the continuum, and during their excursion they experience different electromagnetic environments. The phases accumulated by these two parts are therefore dissimilar. Provided that the radiation from their recombination overlaps in the far field where it is detected we observe something something called quantum path interference (QPI).

Historically, the prospect of several quantum paths contributing to the same photon energy

was already proposed by Lewenstein *et. al* [38] in 1994, while developing the SFA for HHG. Experiments measuring the coherence time for harmonics later revealed that there are two spatially separated regions in the harmonic spectra with different coherence times, and the phenomenon is attributed to the two quantum paths [62–64]. The two paths have unequal phase matching conditions as they have different dipole phase parameters, α [55, 65]. For applications, the phase matching for the shortest path is favored, and the long one is suppressed, in order to avoid temporal interference of the trajectories. Since the QPI contains information about the intrinsic electron dynamics of HHG process there are also experiments that try to phase match both paths in order to observe the interference.

It is important to note that QPI can not be explained classically, as the interference comes from different parts of the light generated by the same EWP. However, much of the behaviour of the intensity dependent dipole phase can be calculated classically, again by treating *part* of the EWP as an electron following the long- and the short trajectories.

The main difference between the phase matching of the long- and the short trajectory is the dipole phase mismatch term in Eq. 2.9. The intensity dependent dipole phase we write as [38]:

$$\Phi = q\omega t_{\mathrm{r}} - \int_{t_{\mathrm{i}}}^{t_{\mathrm{r}}} \left(\frac{\mathbf{p} + \mathbf{A}(t)^2}{2} + I_{\mathrm{p}} \right) \mathrm{d}t, \tag{3.1}$$

where $\mathbf{p} = m_{\mathrm{e}}\dot{\mathbf{x}}$ is the momentum of the electron (EWP part) and $\mathbf{A}(t)$ is the vector potential of the IR field. Since this expression is derived from the SFA it is less accurate in describing the shortest of the short trajectories, *i.e.*, the harmonics for which the photon energy is close to I_{p}, since they are most affected by the atomic potential. It does, however, allow for an interpretation of the phase accumulation for different harmonics. We can interpret the right hand term in Eq. 3.1 as the part of the EWP that has tunneled out, and will return to the core with energy $q\omega$. In this way it can be treated as a laser dressed electron, where the kinetic energy it acquires translates into an increase in the frequency of the EWP part. By integrating the momentum along its excursion path we therefore obtain the average frequency which has evolved during the excursion. The left hand term instead follows the evolution of the bound part of the EWP, starting at the onset of the applied electric field at $t = 0$ until the time the liberated part of the EWP recombines, at t_{r}.

Subsequently, we analyze the trajectories from Fig. 2.4 (a), and the presented solution for the trajectories is general for any parameters of the electric field as long as it is sinusoidal, meaning that we can separate the two trajectories simply by ionization time during the cycle. If there is a returning trajectory, and the ionization event occurs during $0 \leq T \leq 0.3$ then it is a long trajectory, and if the ionization event occurs during $0.3 < T \leq 0.5$ the trajectory is short. We solve Eq. 3.1 for each of the trajectories in order to determine their respective intensity-dependent phase variation, shown in Fig. 3.1.

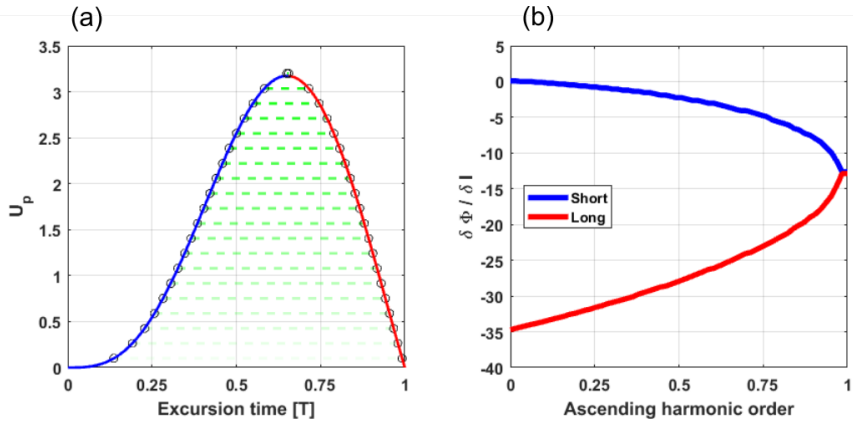

Figure 3.1: (a) Return energy as a function of excursion time. Different harmonic orders (dashed green lines) are chosen to calculate the variation of the intensity dependent dipole phase in (b). The phase behaviour of the long- and short trajectory converge towards the cut-off, since they converge towards the same classical trajectory.

From the results in Fig. 3.1 (b) it is apparent that the long trajectories always have larger intensity dependence of the dipole phase than the short trajectories. This can be attributed to the fact that the long trajectories always spend more time in the continuum and therefore are more sensitive to any change of electric field amplitude. What is also noticeable is that the difference in accumulated phase between the trajectories is largest for the lowest order harmonics, and for increasing harmonic order, the long and the short trajectory converge towards the same path at the harmonic cut-off.

In Fig. 3.2 (a) we instead observe a single harmonic, indicated by the green line, and vary the peak intensity of the driving field. In doing so, the phase variation for a given photon energy can be retrieved, *cf.* Fig. 3.2 (b), showing that the harmonic is at the cut-off when the intensity is low, and as the intensity is increased the harmonic branches off into the long- and short-trajectory contributions.

The intensity-dependent dipole phase of the harmonics ultimately influences the resulting wavefront of the XUV radiation. Since the harmonics are generated close to the focus of an IR laser, the intensity distribution of the IR focus shapes the spatial phase of the harmonic radiation. For all photon energies, except for the cut-off energy, there are two wavefronts generated: one for the short and one for the long trajectory, shown in Fig. 3.3. For a spatially varying focal profile (*i.e.*, not a top hat profile), the wavefront of the long trajectory is always more curved, since its phase is more sensitive to intensity variation, as shown in Fig. 3.2 (b). This results in a more divergent beam. The harmonic spectrum when measured in the far field displays the short trajectories as an intense, on-axis distribution with slightly increasing divergence towards the cut-off. The long trajectories on the other

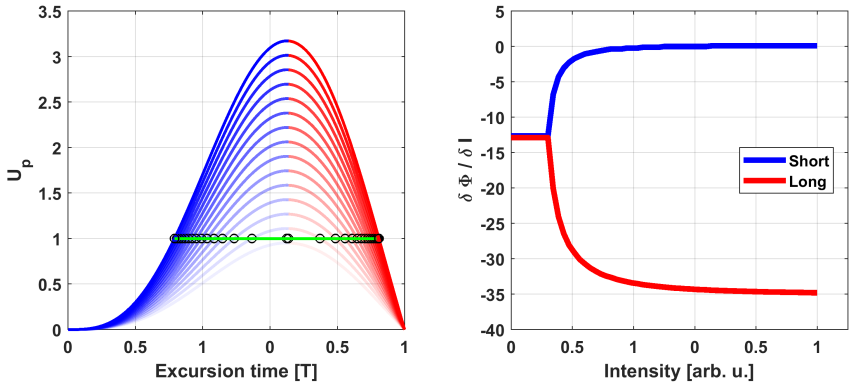

Figure 3.2: (a) Return energy as a function of excursion time, for several different intensities of the driving laser field. For a single harmonic order (green line), the variation of the intensity dependent dipole phase is calculated (b). For the lowest intensities of the driving field there is only one trajectory describing the harmonic. As the intensity is increased, this trajectory branches into a long- and short trajectory contribution.

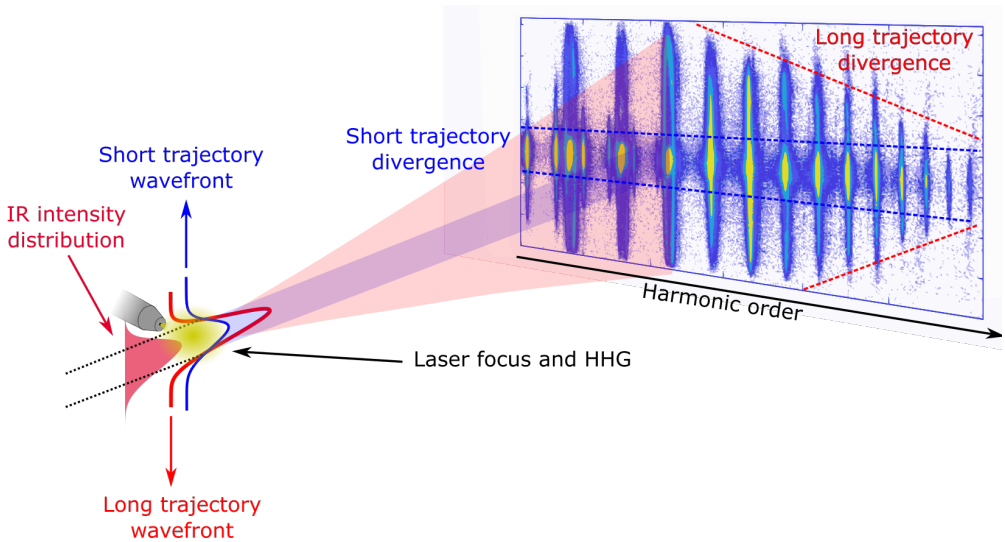

Figure 3.3: Illustration of the trajectory contributions in the far-field. In the near field, the long- and short trajectories will acquire different wavefront curvatures due to their different intensity dependent dipole phase accumulation. The short trajectory is less divergent and will be constricted to a small on-axis angle. The more divergent long trajectory will cover almost the entire detector surface. Contributions from both trajectories are found on-axis, which is where they will interfere.

hand are very divergent for low order harmonics, but converge towards the same divergence

as the short trajectories near the cut-off.

For harmonics far from the ionization potential of the atom, the intensity-dependent phase for the short- and the long trajectories is well approximated by the linear slopes in 3.2 (b):

$$\Phi^{q}_{l/s} = \alpha^{q}_{l/s} I. \tag{3.2}$$

As the dynamics of the two trajectories have a different intensity dependence, the phase of the emitted radiation between these two trajectories will predominantly depend on the difference between the corresponding dipole phase parameters $\alpha^{q}_{s} - \alpha^{q}_{l}$. Our experiments aim at retrieving the difference between, and the magnitude of said dipole phase parameters by measuring and theoretically reconstructing the intensity variation of the harmonics in the spectrum.

3.1.1 200 kHz laser HHG setup

The QPI experiments were performed using the 200 kHz Pharos laser. A custom-built, inherently stable HHG setup was constructed for this purpose. The aim of the setup was to optimize for passive stability, and as such, as few optical components as possible were used to transport the beam to the experiment chamber. The experiment chamber itself was also intentionally kept simple in order to ensure passive stability: only the most necessary components for generating and detecting harmonics were used. A schematic of the setup is given in Fig.3.4 and as can be seen, the beam was focused outside of the vacuum chamber with a 10 cm focusing lens. The beam first entered the Generation chamber, where it was focused at the tip of an effusive gas get. The gas jet had a 50 µm hole and 1-3 bar backing pressure. The harmonics and the laser beam passed through a differential pumping compartment, designed to keep a low (10^{-5} mbar) ambient pressure in the spectrometer chamber. This differential pumping chamber consisted of a pumping hole, 2 mm in diameter placed 3 centimeters after the gas jet, and a second 8 mm differential pumping hole approximately 20 cm from the gas jet. Inside the spectrometer chamber the beam was diffracted using an aberration-corrected flatfield grating (001-0639, Hitachi). The IR beam and the specular reflection (0^{th} order diffraction) were diffracted/reflected onto the walls of the vacuum chamber, whereas the XUV first-order diffraction was incident onto a high-voltage multi-channel plate (MCP) detector. The detector was integrated with a fluorescent screen displaying the XUV spectrum. A camera on the outside of the chamber was then used to record the image (Pike F-505B, Allied Vision Technologies).

The vacuum system consisted of two roughing pumps and two turbomolecular pumps. One of the roughing pumps was used to pump the gas from the effusive gas jet in the generation chamber. The second roughing pump was used as a backing pump for two tur-

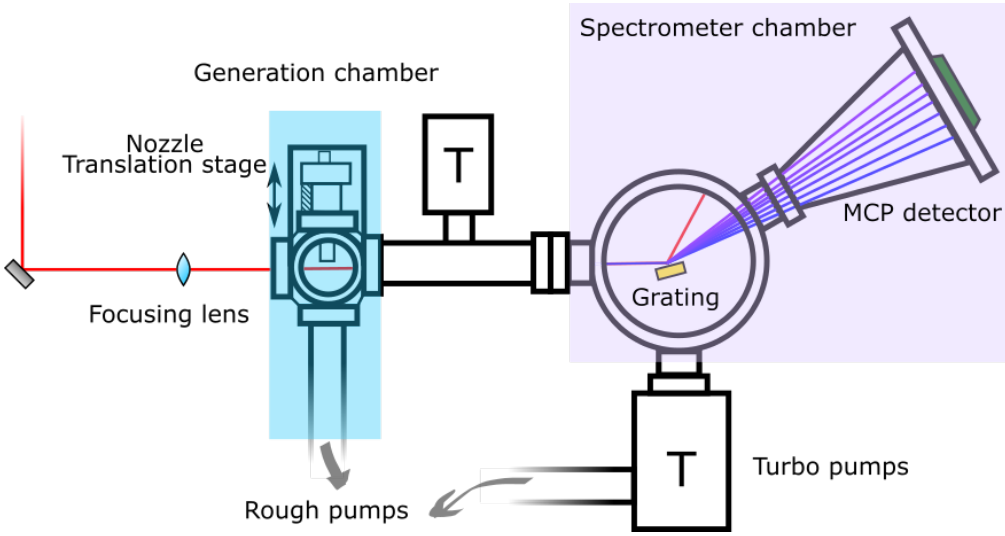

Figure 3.4: Schematic overview of the 200 kHz laser HHG setup. The laser beam from the 200 kHz laser is focused into a target gas nozzle using a 10 cm focusing lens, generating high order harmonics. The laser and the harmonics propagate into the spectrometer chamber, where they are diffracted using an XUV grating. Only the harmonics have a correct diffraction angle in order to be projected onto the MCP detector.

bomolecular pumps. Without the turbomolecular pumps, the chamber could be pumped down to 10^{-3} mbar. With the turbomolecular pumps on, the pressure in the spectrometer chamber managed to reach as low as 10^{-6} mbar without the gas load in the generation chamber. During HHG, with gas constantly injected into the generation chamber, the differential pumping segment managed to maintin a pressure difference of three orders of magnitud between the two chambers. The reason for needing such low pressure in the spectrometer chamber is twofold: prolonging the lifetime of the MCP detector, and limiting reabsorption of the XUV during propagation in the chamber.

When generating harmonics with a 1030 nm driving laser in argon, an intensity of at most $1 \cdot 10^{14} \mathrm{W/cm^2}$ was found to be optimal. With the Pharos laser, this intensity at the IR focus at a 10 kHz repetition rate, and 700µJ pulse energy, was achieved when using a 10 cm focusing lens. The output beam diameter was 5 mm, but the aperture was reduced slightly, using an iris outside the chamber, in order to ensure a more homogeneous beam profile and proper beam spot size in the focus. Typically, 20% of the laser energy was discarded and lost through reflection losses. Optimizing the phase matching was done by adjusting the position of the lens, which was mounted on a linear translation stage outside the chamber, changing the pressure of the gas at the gas nozzle and by trimming the beam diameter with the iris. Typically, the focal position of the IR beam is always located past the gas nozzle for HHG in order to minimize the phase mismatch of the short trajectory. For

QPI experiments the focus was located even further past the gas nozzle, in order to phase-match the long trajectory contributions. The short trajectory contributions were slightly phase mismatched in this configuration, however, their signal reamined strong compared to the long trajectory contributions. The diffraction grating was installed onto a motorized rotation and linear translation stage in order to fine-tune the focusing of the XUV spectrum at the MCP detector.

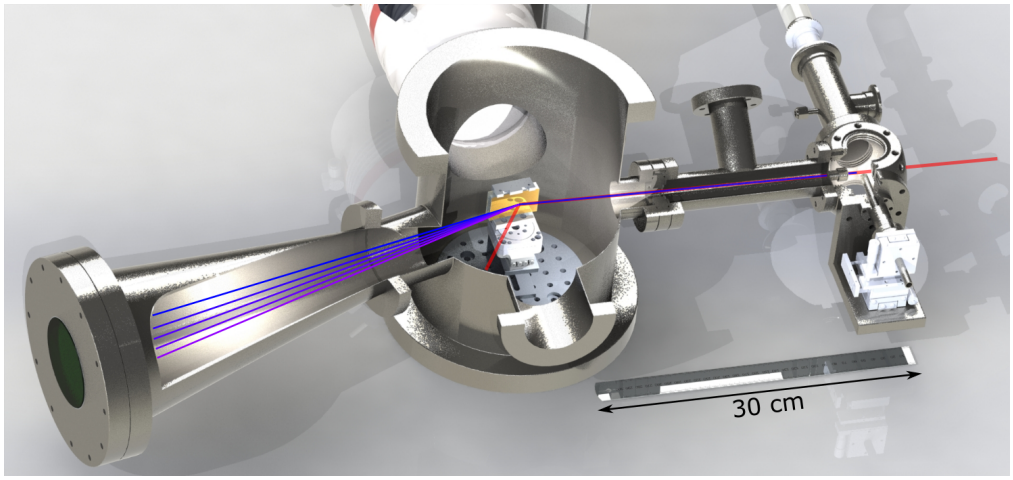

Figure 3.5: Cross sectional rendering of the 200 kHz laser HHG setup, highlighting the small size of the setup. A 30 cm ruler is added in the assembly for comparison. Most of the vacuum equipment, such as the turbomolecular pumps and electrical feedthroughs are removed for simplicity.

What made this setup unique was its size and passive stability. The laser output and beam pointing was designed to be stable for extended periods of time, the chamber was simple and robust, aligning the beam through the setup is not necessary for weeks of intermittent usage and the startup procedure took only a few minutes. Fig. 3.5 gives a rendering of the CAD drawing of the setup, illustrating its size. The XUV spectrometer constituted most of the setup since the grating required specific distances from the source and the MCP detector. In a situation where lower spectral resolution is needed the photon spectrometer could technically be further reduced in size. However, for QPI experiments the spectral resolution was one of the key factors.

3.1.2 QPI measurements

The HHG setup can record high resolution spectra of the narrow harmonics. The Pharos laser has a low intensity fluctuation, providing a very stable measurement of the HHG spectra. The influence of QPI on the XUV spectrum is subtle, and often not directly

visible in the spectrum itself. To clearly see the QPI, variations of the spectrum are studied, as a function of either intensity, chirp or focal point position (in relation to the gas nozzle) of the IR beam. For most of our measurements the chirp was varied, mainly in order to change the peak intensity of the pulses, a technique that was first performed and described by Carlström *et. al* [56]. We refer to this as the *chirp-scan technique*. There are benefits of controlling the chirp instead of the intensity directly, for instance, the compressor grating translation motors of the Pharos laser have a better step resolution than the attenuator. Of course, a custom attenuator could be designed to match the precision of the grating translation, however, another more fundamental benefit is that a chirp scan retains the pulse energy whilst still lowering the peak intensity. This is illustrated in Fig. 3.6, where we assumed that we had a certain peak pulse intensity, I_0, and aimed to reduce it to half using the two different techniques (chirp scan and intensity scan). It was apparent that just attenuating the intensity removes energy from the pulse, whereas chirping it just stretched it in time. By using the chirp scan technique it become possible to reach the same peak intensity, but with the generation process occuring for more cycles allowing for more XUV signal to be generated in each pulse.

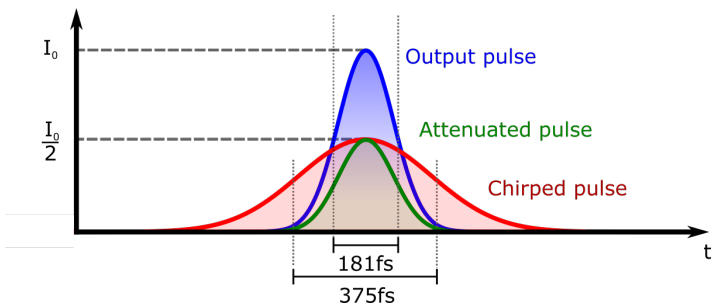

Figure 3.6: Illustration of the difference between a chirp-scan and an intensity scan. The peak intensity of transform limited pulses from the 200 kHz laser is reduced to half of its original value in two ways. In the intensity scan technique (shown in green), the pulse is simply attenuated, discarding energy to reach the new peak intensity value. In the chirp scan technique (red), the pulses are stretched in time in order to attenuate the peak intensity, allowing for HHG during more cycles. The durations shown is the typical transform limited pulse duration (181 fs), and the longest pulse duration before the signal reaches the noise level (375 fs).

Fig. 3.7 shows the measurement procedure of a QPI chirp scan. The motorized compressor grating of the Pharos laser was tuned from producing a negatively chirped pulse- to a positively chirped one, crossing the transform limited pulse duration in the middle of the scan. In the HHG chamber, depending on the peak intensity in the IR focus, the long- and the short-trajectory contributions of the generated XUV radiation had a certain phase difference $\Delta\Phi$, resulting in an interference between the two trajectories that was recorded at the MCP detector. By recording these harmonic spectra for each position of the compressor it

was possible to retrieve the on-axis interference as a function of chirp, by evaluating a section of the data set along a certain harmonic. We called the chirp-divergence cross sections of the data sets *QPI plots*, and they were unique for each harmonic under each generation condition.

For low-order harmonics (15-23 in our experiments) there were two main features noticeable in the QPI plots: the first one was the high-periodicity on-axis modulation as seen in Fig. 3.7, corresponding to the interference between the first- and second quantum trajectory, and the second feature was large concentric rings for which the radius was decreased when the intensity was reduced. This was the movement of the ring-like structures seen in Fig. 3.3 as a function of intensity. The source of this ring-like pattern is currently still debated: some groups claim that these rings are in fact the QPI of the two shortest trajectories [56, 66, 67], while others believe that these structures can be generated only from the long-trajectory contribution interfering with itself, as it has a very strong intensity dependence [68, 69]. Our interpretation is closer to the latter, however, the true origin of this phenomenon was not important for our experiments, as will be explained later, since we reconstruced the QPI with arbitrary sources.

The recorded data was post-processed in order to enhance the visibility of the intensity-dependent interference. First, the harmonic spectra were straightened, and since the harmonics normally display a minor tilt due to alignment imperfections, the spectra were sheared using an affine transform, *cf.* Fig. 3.8 (a) & (b). This ensures that there was an even lineout across the divergence axis, covering the spectral content of the long- and the short trajectory contributions.

The QPI plots of each harmonic were then re-interpolated in order to display a linear dependence of the pulse duration rather than the compressor position, as presented in Fig. 3.8 (c) & (d). The linear pulse duration dependence was closer to an intensity dependence, since it relates inversely to it, as opposed to the compressor position, which has more of a hyperbolic dependency to the intensity and is dependent on the specific compressor that is used. It is apparent from Fig. 3.8 (c) that most of the QPI oscillations were confined to the edges of the QPI plot, which is a result of the dispersion insensitivity of the pulse duration close to the zero chirp of the compressor. Once re-interpolated, *cf.* Fig. 3.8 (d), the oscillating pattern become evenly spread across the entire QPI plot, allowing for a better visual overview of the phenomenon.

The dynamic range of the signal in the re-interpolated spectra was, in this context, mainly dominated by arbitrary intensity-dependent yield of the HHG, which peaked at the shortest pulse duration in each scan. Each row on the divergence axis in the QPI plots was therefore re-normalized to itself in order to enhance the contrast of the QPI oscillations. This is shown in Fig. 3.9, where harmonic 15 was post-processed in order to remove yield-dependent signal. Re-scaling the color axis in 3.9 (a) would increase the contrast of the QPI oscillations

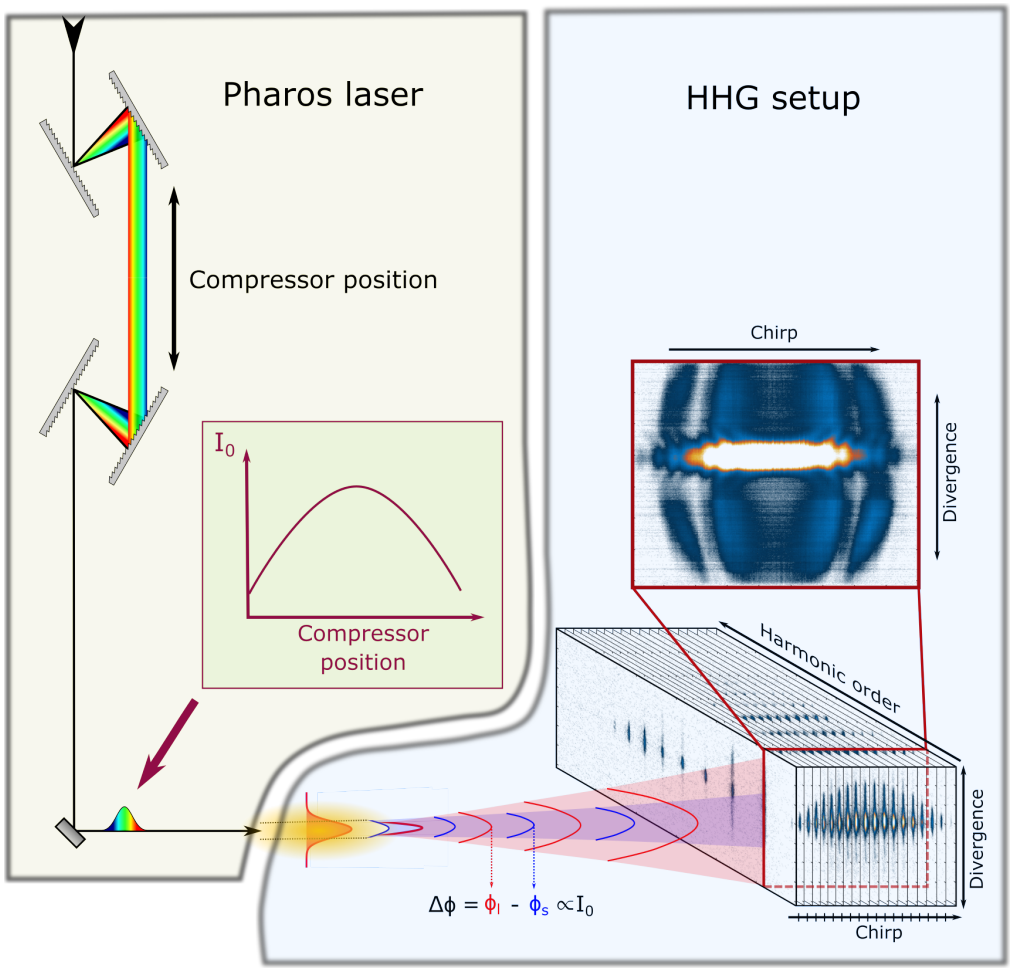

Figure 3.7: Experimental procedure for measuring QPI plots. Pulse duration of the 200 kHz laser output is varied by changing the compressor position, going from negatively chirped pulses to positively chirped. In the HHG focus, the generated harmonics will have different phase relation between the long- and the short trajectories, depending on the peak intensity of the laser. For each compressor position, a harmonic spectrum is recorded, generating a spatio-spectral data set for different intensities of the driving laser. The relevant section of data is the divergence and chirp axis, taken across a harmonic, since it displays the intensity dependent modulations due to QPI.

near the edge, but would also saturate the interference in the center where the pulse duration was close to transform limited. Instead, a horizontal lineout along the chirp axis was evaluated, as shown in Fig. 3.9 (b), and a low-order polynomial was fitted to the intensity profile and subtracted from the signal, leaving only the higher frequency oscillations of the QPI. This was done for each position on the divergence axis, producing a QPI plot only

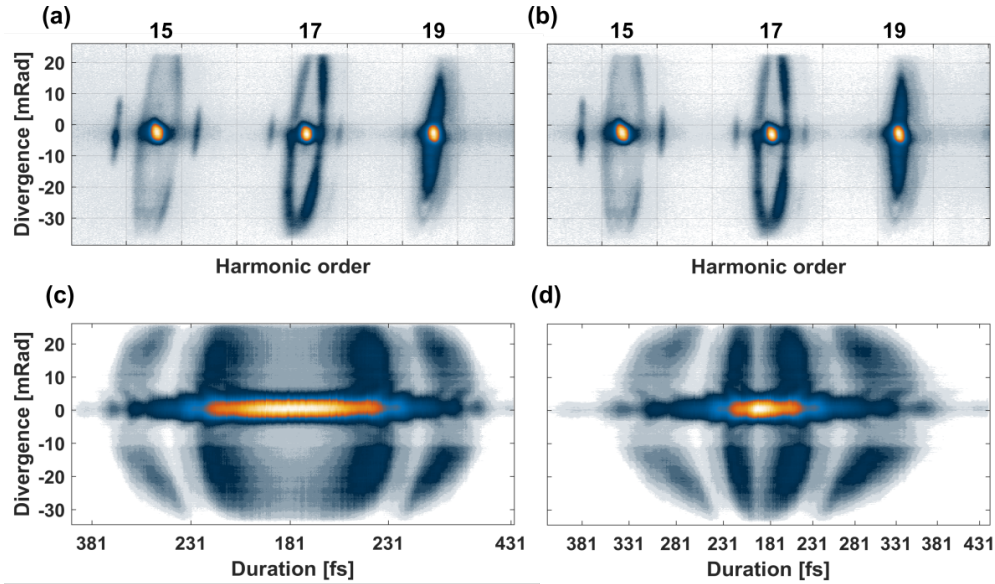

Figure 3.8: Corrections of the measured harmonics in argon, and their corresponding QPI plots. (a) The measured harmonics appear slightly sheared on the detector screen. (b) Using an affine transform, the harmonics are correct in order to appear straight vertical. (c) QPI plot of Harmonic 15. Plotting the divergence as a linear function of compressor position gives a non-linear dependency on the pulse duration. Therefore, a large region close to the transform limited pulse duration where the intensity does not vary. (d) Re-interpolating for linear step size in pulse duration instead gives a more uniform distribution of the QPI fringes.

containing oscillations related to the interference, as shown in Fig. 3.9 (c).

The post-processed QPI plots are representative of the interference of the long- and the short trajectory, seen to occur between -7 to 7 mrad in Fig. 3.9 (c), and the interference seen off-axis. As the chirp scan technique is intended to be an alternate technique for measuring the intensity-dependent phase between the trajectories, it is not clear whether or not chirping the fundamental beam would introduce any additional phase difference between the two trajectories. It is well known that the laser driving field in HHG imparts its chirp on the generated harmonics [70], although it is not apparent if it does so differently for the long and the short trajectory.

The actual influence of the chirp scan was one of the ambiguities that was addressed in **Paper I**. In order to investigate whether any additional phase was introduced through chirping of the IR beam, an intensity scan was performed using the built-in attenuator of the Pharos laser. The post-processed QPI plot from the intensity scan was compared to one from a chirp scan, and the results are presented in Fig. 3.10. The scan range of the chirp scan in

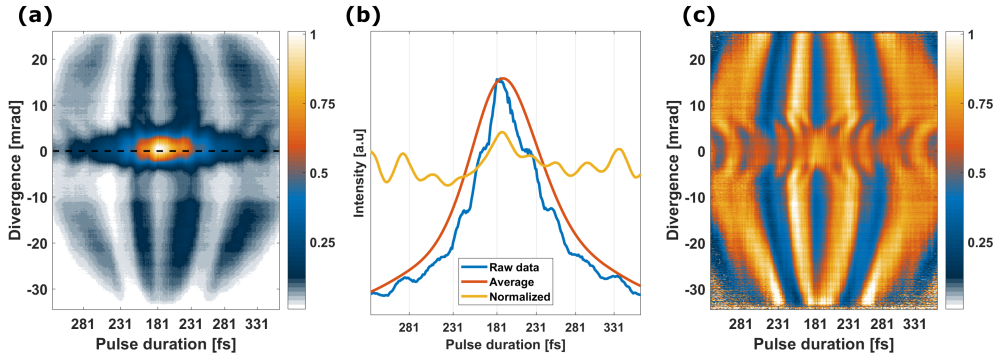

Figure 3.9: The post processing procedure of the QPI plots, shown for harmonic 15 in argon. (a) The dynamic range of the QPI plots is mainly dominated by the intensity dependent yield of the harmonic radiation. The signal of each row on the divergence axis is therefore normalized. (b) A linout, indicated by the black dashed line in (a) is taken, a low order polynomial is fitted and subtracted from the duration dependent intensity profile. (c) The resulting, filtered, fringes of the QPI plot cover more of the dynamic range, providing a better visual overview of the QPI.

Fig. 3.10 (a) was truncated in order to match the scan range of the intensity scan (b). The resulting plots displayed a striking visual resemblance with regard to fringe position of the on-axis QPI, but also for the off-axis interference. One of the main differences between these two techniques is the reduced contrast of the interference fringes in the intensity scan, compared with the chirp scan. Fig. 3.10 (c) shows a cross-section of the on-axis line from the QPI plots, illustrating not only the matching fringe spacing, but also the much more rapid decrease of the XUV signal when using the intensity scan.

Comparing the two scan methods did not directly provide an answer to whether or not the driving field chirp was imprinted differently onto the long- and the short trajectory contributions. However, it was not apparent from the QPI plots that there was a difference between the fringe spacing in the two techniques. As is discussed later, the QPI plots were the structures which we simulated in order to retrieve the number of XUV sources needed, as well as their corresponding dipole phase parameters, to theoretically recreate the HHG process. What the chirp/intensity-scan comparison concluded was that the QPI structures produced with both techniques were as similar *as if* they had been phase-shifted by the same amount due to the driving field chirp and only shifted differently due to their corresponding intensity dependence. The results from **Paper I** showed that the chirp-scan technique can be interpreted as an *effective* intensity scan with an extended scanning range.

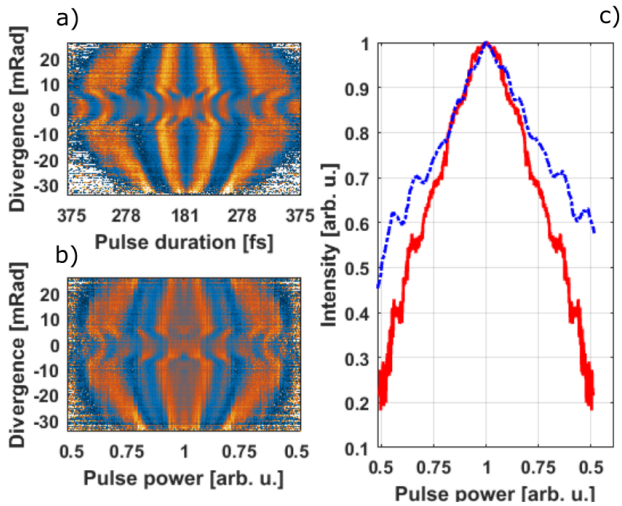

Figure 3.10: Comparison between the chirp-scan technique (a) and an intensity scan (b) performed over the same range of pulse peak intensity attenuation, for harmonic 15 in argon. (c) Lineout across the zero divergence for the chirp-scan (blue) and intensity scan (red) in logarithmic scale.

3.1.3 QPI simulation

Interference between the long- and the short trajectories is found in SFA calculations, however, its interpretation is often shrouded by the mathematics needed for the quantum mechanical explanation. In our simulations we instead relied mainly on a geometric model, presented in [56], allowing us to reproduce a more intuitive origin of QPI as illustrated in Fig. 3.3. The benefit of this model is that the entire understanding of QPI, from the origin of trajectories to the emergence of the QPI plots, can be traced back to the three step model.

The key assumption in the geometrical model is that the interference seen on the detector can be represented by an electrical field E_{DET}, when evaluated in any point along its divergence axis y. At the distance z from the source, the resulting electric field can be described by the interference of two separable sources emerging from $z = 0$:

$$E_{\mathrm{DET}}(y,z) = E_{\mathrm{s}}(y,z) + E_{\mathrm{l}}(y,z), \tag{3.3}$$

where the long- and short trajectory sources $E(y,z)_{\mathrm{l/s}}$ can be written as:

$$E_{\mathrm{l/s}}(y,z) = C_{\mathrm{l/s}} I_0^{\frac{q}{2}} W(z) exp\left[-iG(y,z) + i\Phi_{\mathrm{l/s}}(y,z)\right]. \tag{3.4}$$

Here, $C_{l/s}$ is a constant describing the intensity ratio between the long- and the short trajectories. $W(z)$ is the evolution of the beam waist of the harmonic as it propagates and $G(y,z)$ is the geometrical phase from focusing. The dipole phase term, $\Phi_{l/s}(y,z)$, can be expanded as:

$$\Phi_{l/s}(y,z) = \alpha_{l/s} I_0 + \Phi^0_{l/s}, \tag{3.5}$$

where $\alpha_{l/s} I$ is the intensity-dependent dipole phase that we are interested in, and $\Phi^0_{l/s}$ is a constant offset of the phase. The latter only affects the position of the QPI fringes and not their periodicity, wherefore $\Phi^0_{l/s}$ was set to zero in our simulations. The result of Eq. 3.3 gives a one dimensional interference across the divergence axis. The calculation of Eq. 3.3 is repeated for several different intensities, I_0, and the results are collated into an image that resembles a chirp scan, as seen in Fig. 3.11 (a). The parameters are optimized to visually match the experimental QPI plot presented in Fig. 3.11 (b), and the crests from the simulation are overlaid on the measured QPI plot to illustrate the resemblance of the features.

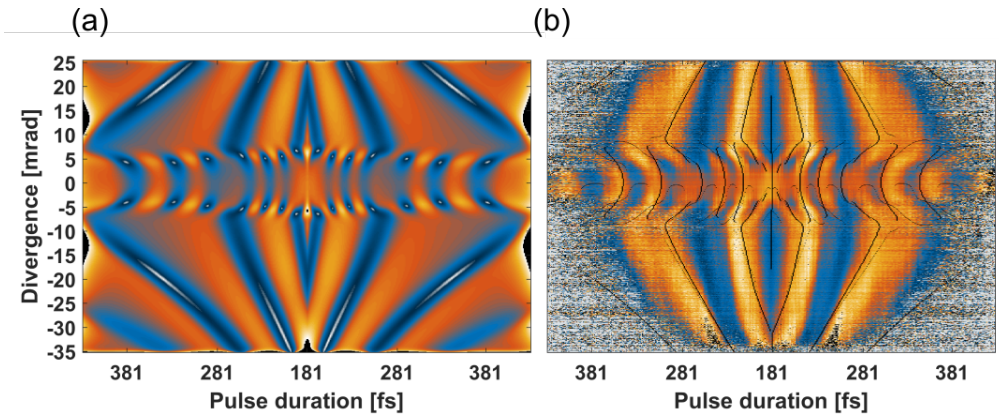

Figure 3.11: (a) Optimized result from the Gaussian beam model for harmonic 15 in argon. The crests from the interference fringes from the theoretical model are overlaid on the measured chirp-scan (b)

The visual matching procedure covers a large parameter space, however, most of the parameters are set when reproducing the experimental conditions. The constant $C_{l/s}$ does not influence the position or the periodicity of the interference fringes, instead, it is just used to change the contrast of the interference. The terms $W(z)$ and $G(y,z)$ are given by the focusing geometry which is used in the lab. The intensity in the IR focus, I_0, is estimated from the focal spot size and pulse power. The remaining unknown parameter, $\alpha_{l/s}$, is the quantity we want to retrieve from the simulation.

Estimating $\alpha_{l/s}$ from a single calculation of Eq. 3.3 is possible by matching the divergence of the beams with the experimentally measured spectra. However, the divergence depends strongly on the accuracy of the estimation of the IR focal spot size and intensity. Additionally, the divergence of the beam measured on the MCP detector does not necessarily correspond to the simulated beams divergence due to the nonlinear response of the MCP detector. Instead, the divergence of the beams is matched as a first estimation of the $\alpha_{l/s}$ values. Matching the periodicity and curvatures of the interference fringes, however, requires more precision. Therefore, the accuracy in determining the difference between the dipole phase parameters, $\alpha_s - \alpha_l$, is higher than determining their absolute values.

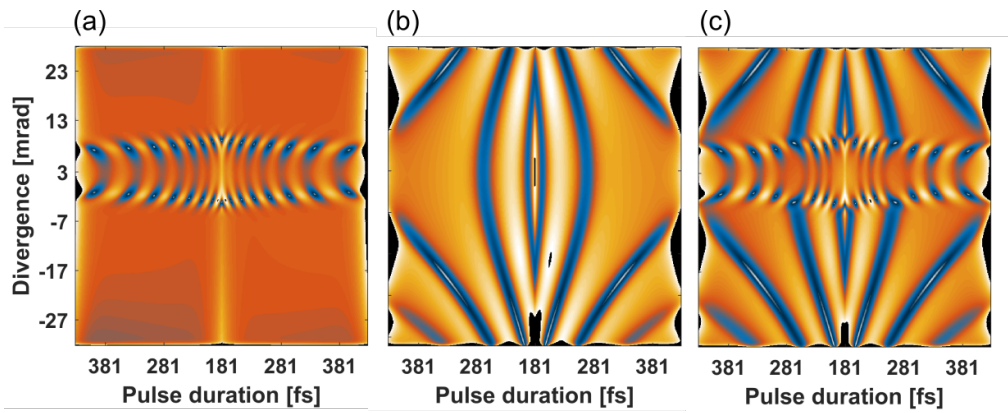

Figure 3.12: Separation of the QPI contributions in the Gaussian beam model for harmonic 15. (a) Only including the long- and the short trajectory, (b) two long trajectories and (c) all three trajectory contributions.

In addition, when retrieving the dipole phase parameters for the long and short trajectories, the off-axis interference is also reproduced by introducing a third source term with a dipole phase parameter α_3 that is slightly larger than α_l. In the off-axis region no short-trajectory contributions are expected, and the α_3/α_l interference can therefore be matched before introducing the short trajectory contributions. The different interference phenomena are illustrated in Fig. 3.12 and in (a) we see only the long- and the short trajectory interference, which is confined to the on axis region. In (b) the α_3/α_l interference is displayed, and in (c) we have all three sources. The off-axis modulation slightly distorted the periodicity of the long- and the short-trajectory interference, which is consistent with the experimental observations in Fig. 3.11. Due to this shift of the fringe positions, there is a slight correction of the retrieved value of α_s in our simulations.

A full comparison of the measured and simulated QPI plots is presented in Fig. 3.13. The model and the measured plots were in good agreement for most harmonics, but the model struggled with reproducing the features of harmonics 19-23. The model also omitted the decreased efficiency of the HHG process when the pulses were very long, which appeared

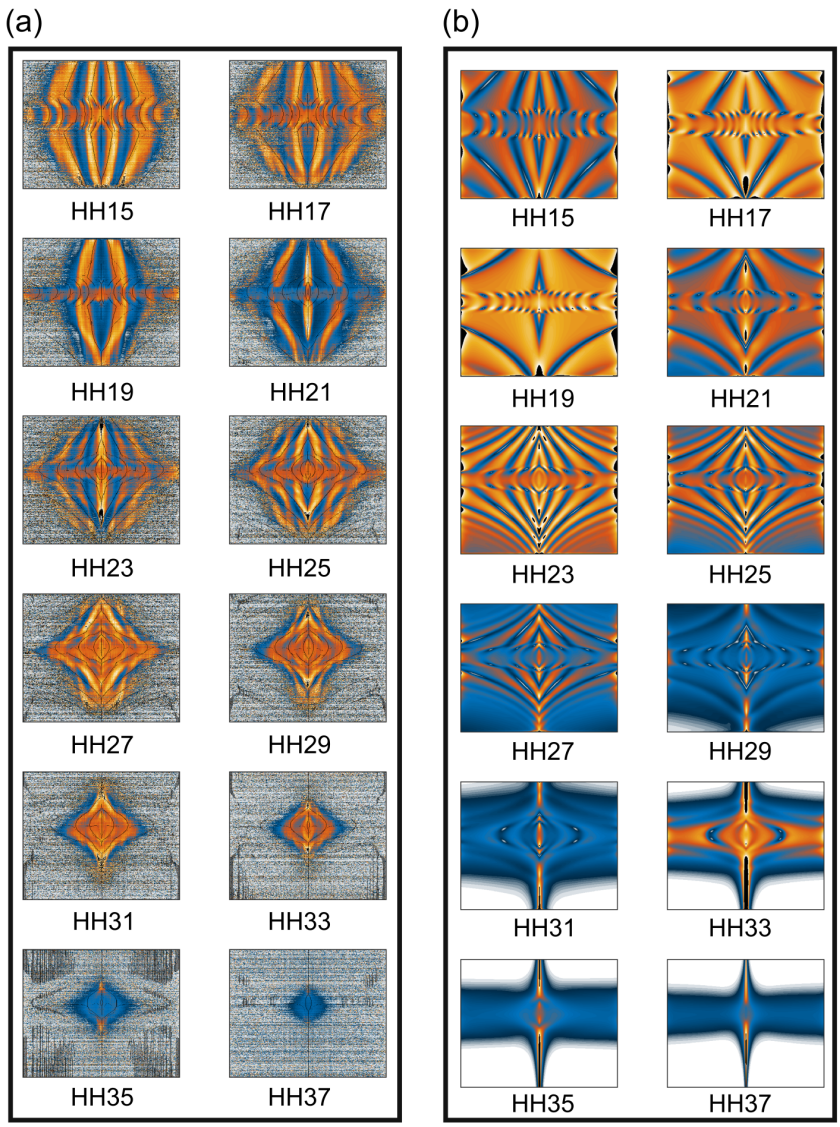

Figure 3.13: (a) Measured QPI plots for harmonics 15-37. (b) Optimized QPI plots, using three sources, from the Gaussian beam model. The crests of the fringes from the simulations are overlaid on the measured QPI plots (black lines).

as noise in the corners of the measured QPI plots in Fig. 3.13. For this reason, we only compared the corresponding area in the modeled QPI plots. Still, the main features, such as the position and periodicity of the fringes, both on- and off-axis, could be accurately reproduced using the geometric model.

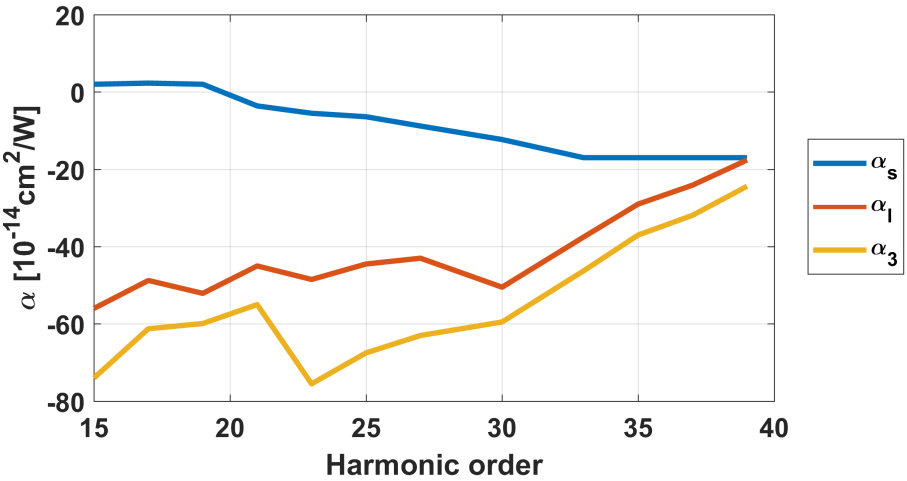

Figure 3.14: The retrieved alpha parameters from the manual fitting procedure.

Fig. 3.14 presents the retrieved α-values as a function of harmonic order. The separation $\alpha_s - \alpha_l$ was largest for the lowest measured harmonics and converged towards the cut-off. This was consistent with the classical calculation shown in Fig. 3.1. The α_s-values for harmonic orders 17 and 19 consistently showed the opposite sign compared to the α_l-values, otherwise it was not possible to match the curvature of the QPI fringes. An opposite sign of the α-parameter indicates that the phase of a certain harmonic decreases with increasing intensity. This anomalous intensity dependence can be seen in the measured QPI plots for harmonic orders 15 and 17 in Fig. 3.13 as a concave curvature of the QPI pattern. Harmonic orders 19 to 23 were close to the zero crossing of the α-parameter and did not display any modulations on-axis. The harmonics above order 23 displayed only convex fringe curvatures, indicating that the α-parameters were all positive.

The origin of the anomalous intensity dependence of the dipole phase parameter is currently still not understood. The negative α-parameter can be obtained classically from Eq. 3.1, however, the trajectories used to obtain the negative α-values are the ones closest to the atom. As the equation is derived from SFA, where the atomic core is completely neglected, it is unlikely that the equation properly describes the phenomenon under observation.

3.1.4 Interpretation of the third source

The experimental and simulated results indicate that, for low-order harmonics, two distinct interference regimes occur in the QPI plots: the on-axis, high-periodicity long-/-short-trajectory interference, and an unknown off-axis, low-periodicity interference. One of the possible explanations for the off-axis interference is self-interference of the long trajectory [56, 68, 69].

This type of interference cannot be reproduced in the geometrical model with one single source, because in our simulations, the paraxial approximation is made in order to analytically solve the propagation to the far field, resulting in a parabolic expression for the calculated wavefronts. A parabolic wavefront will never interfere with itself, however, we expect the wavefronts to be Gaussian in the experiments, and these types of wavefronts can interfere with themselves. We can interpret the third source contribution as a first-order approximation of the self-interference of the long trajectory, as illustrated in Fig. 3.15 (a). At the tails of a Gaussian wavefront there are emitters that can radiate to the same point in the far field as emitters from the slope of the Gaussian wavefront. By using two parabolic wavefronts we emulated the interference of spatially separated emitters in the far field.

In a different interpretation, we can consider the third source to be an approximation for the non-linear part of the intensity-dependent dipole phase. The choice of α-parameter is only valid for a given intensity, and works best for describing harmonics near the cut-off, since these harmonics are only generated at the highest intensity near the peak of the spatial intensity distribution. The lower-order harmonics were generated across the entire spatial distribution, at different peak intensities, and could therefore have a spread of different α-parameters, as shown in Fig. 3.15 (b). Near the wings of the intensity profile, the magnitude of the α-parameter for a given harmonic was small, meaning that the spatial phase variation was low compared to the peak of the intensity profile. Accounting for this non-linearity of the α-parameter, the wings of the parabolic wavefront can become flattened and cause spatially dependent interference in the far field.

Another, more exotic, interpretation of the third source is that it originates from the third trajectory, *i.e.*, an electron that missed the parent ion during the first return and therefore recombined in the subsequent cycle. The third trajectory was theoretically determined beforehand in both SFA [38] and TDSE [55], but not measured experimentally.

The principal difference between the third-trajectory and long-trajectory self-interference in the chirp-scan technique is how the intensity-dependent dipole parameter, α, behaves when approaching the cut-off. For the interpretation of long-trajectory self-interference, the difference $\alpha_1 - \alpha_3$ should converge towards zero at the cut-off. In the self-interference interpretation, α_3 was introduced to correct a geometrical mismatch between experiment and model. Since the divergence of the harmonics decreased towards the cut-off, we would

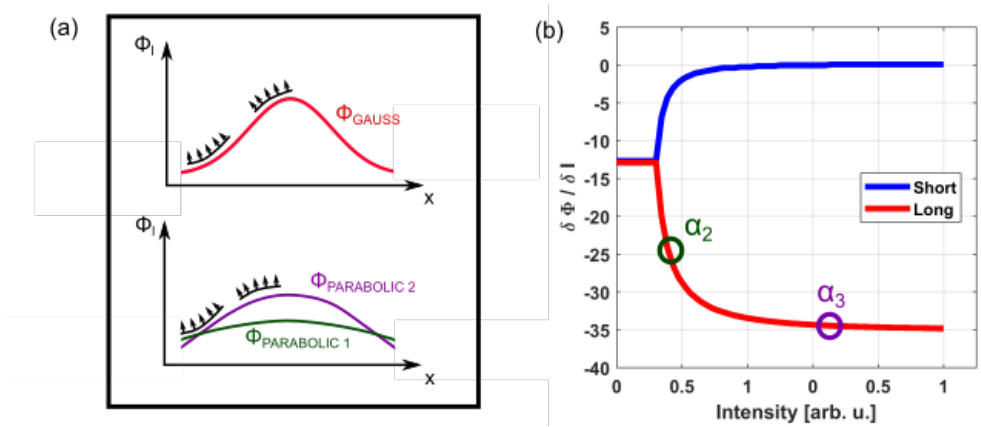

Figure 3.15: (a) Illustration of the expected wavefront in the experiments (top). At the wings of the Gaussian distribution the slope of the intensity profile changes, allowing for light emitted near the wings to interfere with light emitted at the slope. (bottom) Using two parabolic wavefronts, it is possible to reproduce the self-interference effect from a Gaussian intensity distribution. (b) For a given harmonic, linear intensity dependent phase is only valid for high intensity (near the peak of the intensity distribution). For lower intensities, the phase accumulation is lower.

expect $\alpha_1 - \alpha_3$ to decrease with the divergence, as in Fig. 3.14.

For the interpretation of long-/-third-trajectory interference, based on TDSE calculations [56], we would expect $\alpha_1 - \alpha_3$ to have a constant separation up to HH21, and from HH23 it is presumed to diverge. The difference between these two fitting procedures should be the largest for higher harmonics. The cut-off energy for the third trajectory is lower than for either the long or the short trajectories, however, this has no effect on the comparison. What is important is that the QPI plot contains visible off-axis structures. From Fig. 3.13, HH27 and HH29 were considered to be the last harmonics to display off-axis interference.

Fig. 3.16 displays the results of the comparison. For the third-trajectory interpretation we used a diverging model for the α-parameters, and for the long-trajectory self-interference we had a converging model for the α-parameters. The comparison shows the measured QPI plots with the crests (black lines) of the simulated QPI plots superposed. In this spectral region, the QPI plots had just a short scan range before the signal dropped to the noise level, and the divergence of the harmonics was low. There is therefore a limited number of oscillations in the interference that could be matched. However, certain indications pointed at the crests from the diverging model fitting the measurements better. The resulting α-parameters are shown in Fig. 3.17. For harmonics above HH29 there was no visible off-axis interference to match, and they were not assigned an α_3. In this alternative interpretation of the third source, the behavior of the α_1 and α_3 values is more concise compared to their

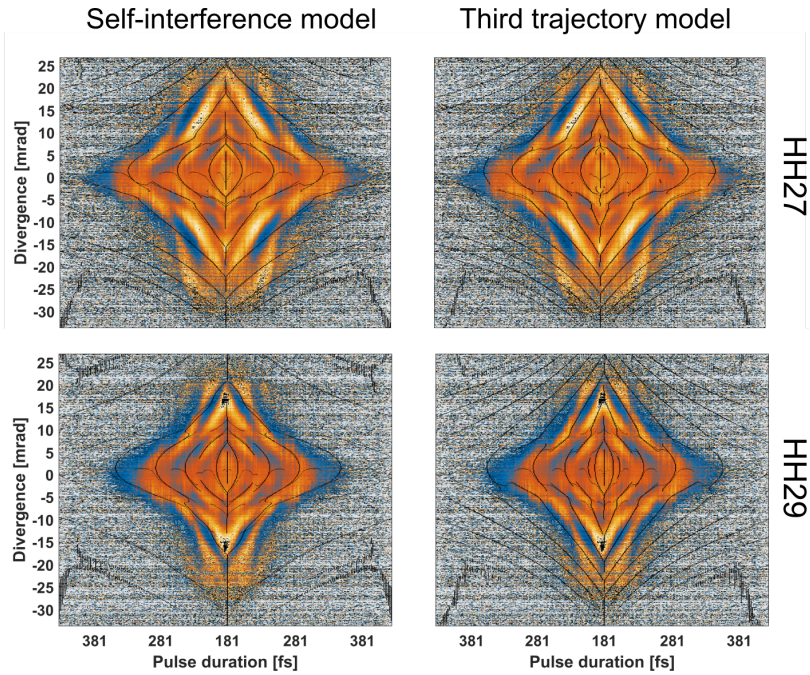

Figure 3.16: Comparison between the two interpretations of the third source contribution. The self-interference interpretation proposes that a_1 and a_3 converge (left column). In the third trajectory interpretation a_1 and a_3 should diverge (right column). The comparison is made for the two highest harmonics that still display off-axis interference, H27 (top) and H29 (bottom).

corresponding values in Fig. 3.14, where there occurred an increase of their separation in both models starting at HH23.

The results from these comparisons should not be interpreted as proof of a third quantum trajectory. The chirp-scan technique works best for the long- and short-trajectory interference, where many interference oscillations can be matched. For the higher-order, off-axis interference there were only two oscillation fringes that matched. The results from these comparisons only indicate how the presence of a third trajectory would affect our QPI plots.

3.1.5 Conclusions

The chirp-scan technique together with the Gaussian beam simulations can decompose the interference, due to the intensity-dependent dipole phases, of the long and the short trajectories. The chirp-scan technique reduces the peak intensity of the IR laser pulses,

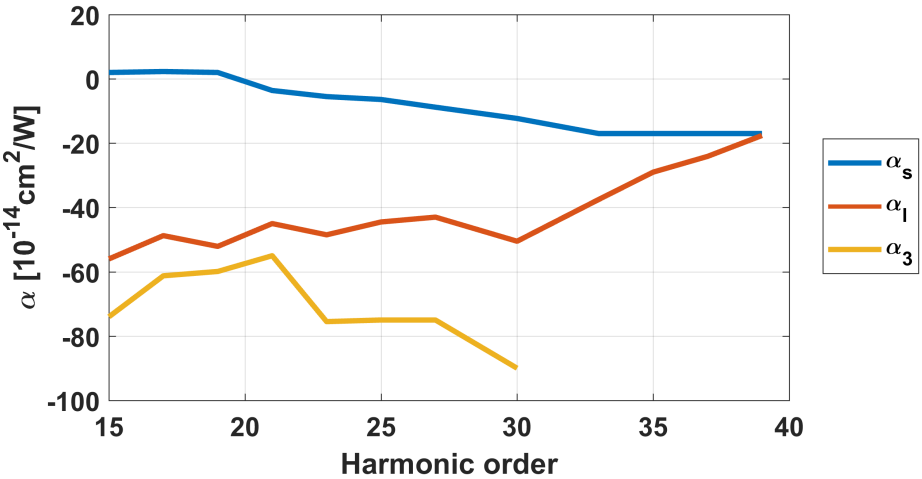

Figure 3.17: The alpha-values retrieved when fitting with divergent a_1 and a_3 values in Fig. 3.16.

but retains the pulse energy, allowing for an increase in possible scan range. By comparing the chirp-scan technique with an intensity scan, we demonstrated that an additional phase between the long- and short-trajectory contributions is not introduced due to the chirp of the IR laser beam.

In the QPI plots, the difference in dipole phase parameters, α, translates into the spacing between oscillation fringes. The retrieval of the α-parameters is done by visually matching the simulated and experimental interference pattern crests. In the simulations, we introduced a third source in order to model the, low-periodicity, off-axis interference. Our results showed that the short trajectories of the harmonics, close to the ionization threshold of the target atom, had an anomalous behavior of the α-parameter. Harmonics 19-23 displayed very faint interference on axis, and harmonics above HH23 had a normal behavior of the α-parameter. These results indicate that there occurred a zero-crossing of the short-trajectory α-parameter found in our spectra.

3.2 Opto-optical modulation

Opto-optical modulation (OOM) is a technique for spatial modulation the phase of XUV radiation using an IR control pulse [25, 26].

The principle operation of OOM is that XUV radiation in our experiments (generated by HHG) is refocused into a gas target, resonantly exciting the atoms into a coherent superposition of the ground and excited states. This excitation can be long-lived compared to

the duration of the XUV pulses. When the XUV pulse has passed, and while the atoms are still in a superposition state, an IR control pulse is used to AC-Stark-shift the energy level of the excited states. For a given excited state, A_n, we can express this Stark-shift of an energy level by [71]:

$$A_n(E) = A_n + \delta A_n(E), \tag{3.6}$$

where $A_n(E)$ is the energy of the Stark-shifted state in a time-varying electric field E, and $\delta A_n(E)$ is the magnitude of the shift in energy, as illustrated in Fig. 3.18 (a). Once the IR control pulse has passed, the excited state shifts back to its unperturbed energy level, A_n. For the highest states of an atom, the direction of the Stark-shift is predominantly towards a higher energy, and these are the states considered in the following example. As the phase of the excited state evolves at a higher frequency when it is shifted to a higher energy, the phase of the emitted radiation becomes advanced, compared to the state in the absence of an IR control pulse, *cf.* Fig. 3.18 (b). The accumulated Stark phase, Φ_S, can be expressed as the time-integral of the Stark-shift of the state δA_n during the presence of the IR control pulse τ_{IR} [25]:

$$\Phi_S = \frac{1}{\hbar} \int_{\tau_{IR}} \delta A_n(t) dt, \tag{3.7}$$

where $\hbar$ is the reduced Planck's constant. The shift δA_n is state- and intensity-specific, therefore it is possible to control the spatial phase of the XUV emission by tailoring the overlap of the spatial intensity distribution of the IR control pulse across the XUV-excited ensemble.

The XUV emission can be redirected by controlling its spatial phase, and this process is illustrated in Fig. 3.19. The XUV pulse is focused into the target gas medium, coherently exciting the atoms. The excited atoms slowly radiate collinearly with the pump XUV pulse, producing narrow absorption lines in the spectrum measured at the far-field. The foci of the pump XUV beam and the IR control beam are slightly off-centered. The larger IR focus covers the XUV focus within the slope of its intensity distribution, and the excited ensemble therefore experiences a spatial intensity gradient when it is Stark-shifted, introducing a spatial phase variation capable of rotating the wavefront of the emitted XUV radiation. This renders it possible to redirect the XUV beam by controlling the offset and the intensity of the IR control beam.

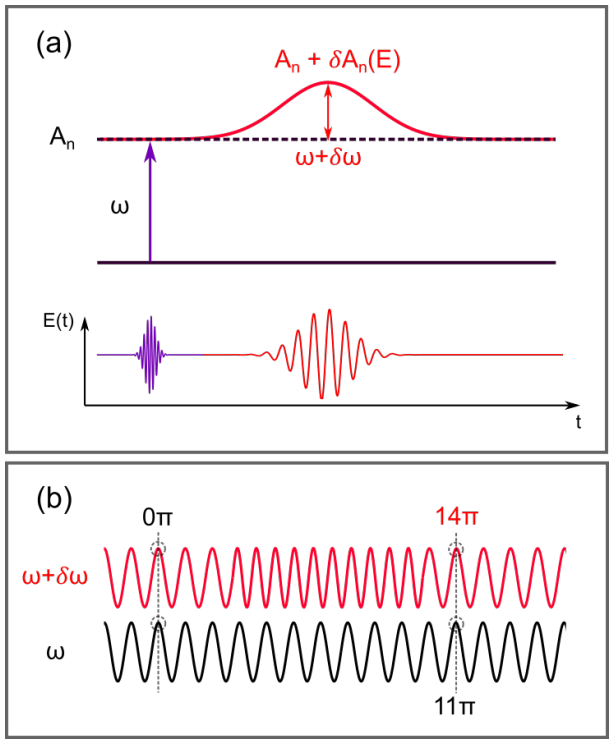

Figure 3.18: Illustration of phase accumulation from AC-stark shift. (a) An XUV beam, with frequency ω, resonantly excites an atom to an excited state, A_n. After the XUV pulse has passed, a non-resonant IR pulse Stark shifts the state A_n by $\delta A_n(E)$. (b) In the presence of the IR pulse, the energy separation from ground to excited state is given by $\omega + \delta\omega$. Once the IR pulse has passed, the phase of the Stark-shifted state will have advanced faster compared to an un-shifted state.

3.2.1 Experimental setup

The OOM experiments were performed with the 1- kHz laser system. The setup for OOM was based on a Mach-Zehnder type interferometer, where most of the optics were inside a vacuum-chamber in order to avoid jitter between the two arms due to sound vibrations and air turbulence. Fig. 3.20 illustrates the beam propagation through the interferometer. The IR beam from the laser was split before the chamber using an annular mirror. The reflected outer part from this annular mirror was used for HHG inside the chamber, and the transmitted inner part is used as the IR control pulse. The beams entered the chamber through two window ports at the Brewster angle for the IR wavelength, which allowed for lossless transmission into the chamber. Inside the chamber, the beams were reflected using a set of two annular mirrors, **HM1** and **HM2**. The small control beam was reflected on the side of the hole on **HM1**, and the larger, annular, generation beam covered only the

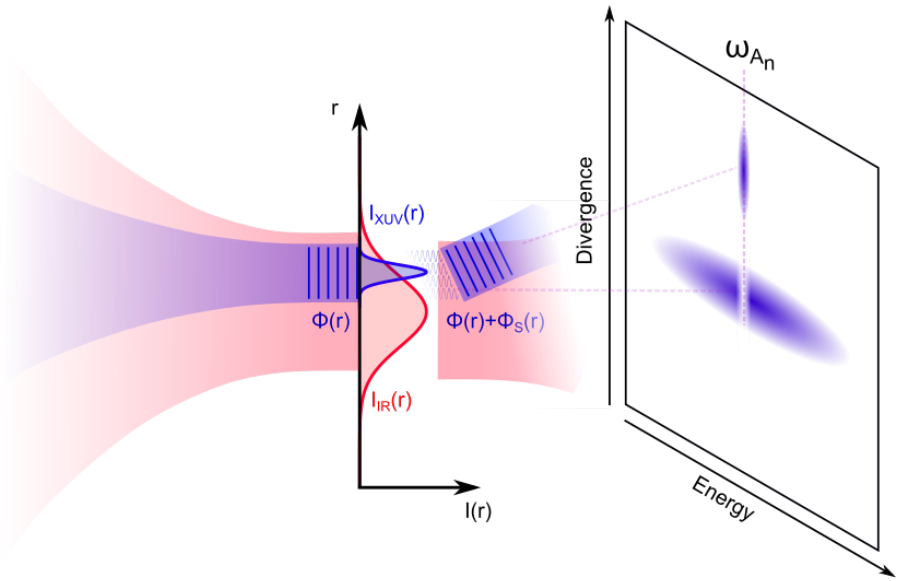

Figure 3.19: Illustration of XUV redirection with OOM. An XUV pulse is focused into a gas target, resonantly exciting a long lived state. After the XUV has passed, a slightly off-centered IR control pulse is is overlapped with the excited gas region, such that the excited region experiences the intensity gradient of the IR control pulse. The IR pulse Stark-shifts the state, creating an spatially intensity dependent phase accumulation. This phase accumulation tilts the resulting wavefront of the radiating XUV emission, redirecting it off-axis.

reflective part of **HM2**.

The beams were reflected into a delay chamber, where two focusing mirrors **FM1** and **FM2** reflected and focused the beams back through the annular mirrors (**HM1** and **HM2**). The focusing mirrors were mounted on motorized translation stages from SmarAct (SLC-2445-S-HV) in order to control the delay between the arms. The focusing mirror in the control arm also had an additional, higher-precision piezo translation stage from Piezosystems Jena (PX 100 CAP vacuum). The generation beam passed through **HM2** and was focused into a pulsed gas cell (Attotech GR020), synchronized with the IR laser at 1 kHz, generating high order harmonics. The generation beam and harmonic beam passed through a differential pumping hole into the recombination chamber, where the more divergent, annular generation beam was removed using a motorized iris, **I1** (SID-0-22-S-HV, SmarAct). When performing HHG with the pump beam, however, a nonlinear phase for the IR beam was accumulated, resulting in small amounts of on-axis IR radiation passing through the recombination mirror **RM2**. A filter wheel with thin metallic filters can be used right before the iris to ensure that no residual IR from the pump arm is transmitted after recombination. The lower-divergence Gaussian spatial intensity profile of the harmonic beam was

transmitted through the partially closed iris and transmitted through the annular IR-XUV recombination mirror, **RM2**.

The IR control beam was focused in vacuum, after passing **HM1**. The control beam could be attenuated using a motorized iris, **I2** (SID-0-22-S-HV, SmarAct), and the smaller control beam was then reflected, using **RM1**, horizontally next to the hole on the annular recombination mirror **RM2**. The XUV and IR beams were then incident on a platinum-coated torodial mirror, re-imaging the foci of the beams, using 2f-2f geometry, into the application chamber.

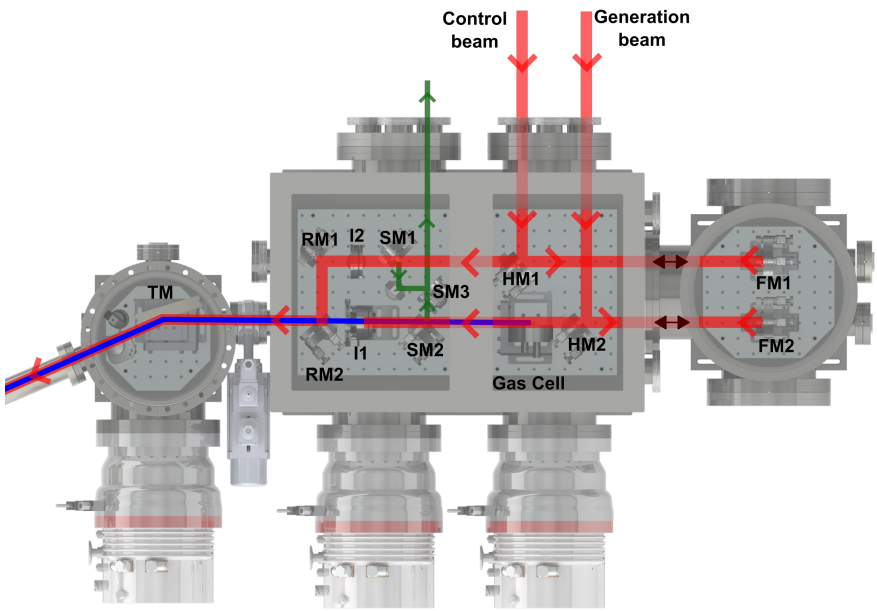

Figure 3.20: Schematic view of the beam propagation through the interferometer vacuum chamber. The IR pulses from the 1 kHz laser are split outside the chamber using an annular mirror into a control beam and a generation beam. The beams enter the chamber through window ports. The control beam is reflected on the side of an annular mirror, **HM1**, towards a focusing mirror, **FM1**. **FM1** focuses the beam back through the hole of the annular mirror, onto a plane mirror **RM1** and finally to the annular recombination mirror **RM2**. The generation beam follows a similar path, being reflected on an annular mirror **HM2**, a focusing mirror **FM2** but is then focused into a pulsed gas cell generating harmonics. The IR beam and the XUV beam in the generation arm travel to an iris **I1**, where the less divergent harmonic beam passes through the iris opening and most of the IR beam is discarded. A metallic filter wheel (not pictured) can also be used to completely remove the residual IR beam in the generation arm. The XUV beam passes through the annular mirror, **RM2**, recombining with the IR control beam. Together the beams propagate towards a torodial mirror where their foci are imaged in an application chamber.

Since both beams underwent focusing they had the same parity, as both of their profiles were inverted. In addition, the mirror parity in both the generation and control arms was equal, meaning that pointing instabilities of the input beam would shift the two split beams in the same direction. Aside from accounting for passive stability, the interferometer was also actively stabilized using a CW HeNe laser (R-32734, Newport). The HeNe laser co-propagated with the IR beam before it reached the interferometer, and once inside it traveled the same path as both the control- and generation beams. Part of the HeNe was picked-off at **SM2** in the generation arm, and at **SM1** in the control arm. The beams recombined at **SM3** which coupled them out through a window port of the chamber, where the two HeNe beams were made to overlap in order to display spatial interference fringes. When the stabilization system was active, it controls the motorized translation stages of **FM1** in order to keep the fringe position static. **RM1** and **RM2** were however not stabilized, since they were positioned after the HeNe pickoff.

In the application chamber, the XUV and IR beam foci were located in a second pulsed gas cell (Attotech GR020), shown in Fig. 3.21. This is where the XUV pump pulse coherently excites the gas and the IR control pulse Stark-shifts the excited states. The beams then enter a photon spectrometer, almost identical in design as the one described in Sec. 3.1.1. In the detector, the XUV radiation is spectrally resolved in the horizontal axis (in the lab frame). The redirection using OOM must therefore be done in the vertical axis. This is achieved by offsetting the overlap of the foci in the vertical direction, using **RM1**. The position of the gas cell can be moved using a 3D-translation stage located outside of the chamber, controlling the gas cell through an edge-welded, vacuum-compatible bellow.

The interferometric setup has certain drawbacks, which need to be considered when performing OOM experiments. Since the IR control pulse is attenuated using an iris, the focal spot size also changes when the beam is attenuated. In some scans, a variable-density ND filter can be used outside of the chamber, however, this filter is not motorized and can not fully attenuate the beam. Since the translation stages for the delay control move the focusing mirrors, the position of the foci also becomes displaced. Although the scan range is usually not very long– at most a few millimeters (corresponding to a few picoseconds (10^{-12}s)) –it might influence the spatial overlap of the IR and XUV pulses in the application chamber.

A typical spectrum of harmonics generated in argon with the setup, with a fully open iris, **I1** , is shown in Fig. 3.22 (a). The harmonics were not as uniform as those generated in the 200– kHz setup, as seen in, for example, Fig. 3.8. On either side of most harmonics in Fig. 3.22 were two additional intensity peaks, corresponding second order diffractions of the cutoff harmonics. The irregular shape of the harmonics most likely originated from the generation with the annular beam. Since the central part of the generating IR beam was used for the control pulse, the annular part of the beam was used for HHG. The annular beam was trimmed using another iris, before entering the interferometer chamber,

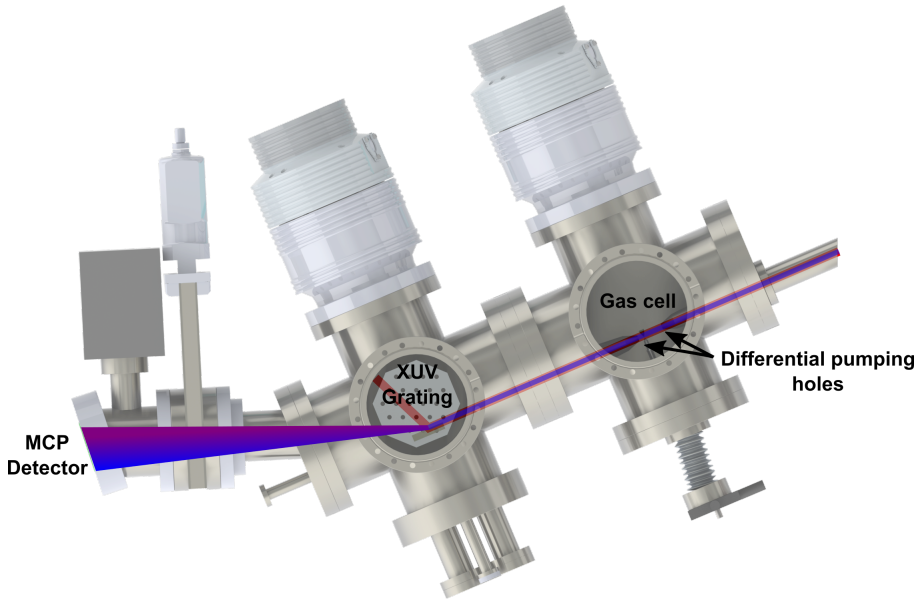

Figure 3.21: Schematic view of the target gas chamber and the spectrometer chamber succeeding the interferometer chamber in Fig. 3.20. The foci of the XUV pump and the IR control beam are imaged into a pulsed gas cell for the OOM experiments. The target gas chamber has two pinholes to limit the gas into both the spectrometer chamber and the preceding torodial mirror chamber. After passing though the spectrometer chamber the XUV pump and IR control pulse are incident onto a focusing flatfield grating. The zeroth order dispersion (specular reflection) hit a beam block, the IR diffraction hits the side of the chamber, and only the diffracted XUV light is imaged onto a MCP detector.

in order to control the intensity of the beam in the interaction region. The generation beam therefore had a thin, ring-like intensity distribution.

Any irregularities of the original IR beam profile will influence the quality of the focus in the HHG chamber. The harmonics still displayed visible contributions from the long and the short trajectories, however, at a much lower divergence compared to the 200–kHz setup. Since both setups used an identical geometry of the photon spectrometer, the divergence on the detector screen was set by the focusing geometry. The setup for OOM used a 40 cm focusing mirror for HHG, compared to the 10 cm focal length lens in the QPI setup.

When performing the OOM experiments, the divergence of the harmonics was further reduced using the iris, **I2**, in order to measure as small off-axis shifts due to OOM as possible. The divergence of these harmonics was usually close to 1 mrad, as shown in Fig. 3.22 (b). In order to reach resonances with the harmonics, the intensity of the generating IR beam was increased blueshifting the harmonics [72]. Shifting the central frequency of the harmonics

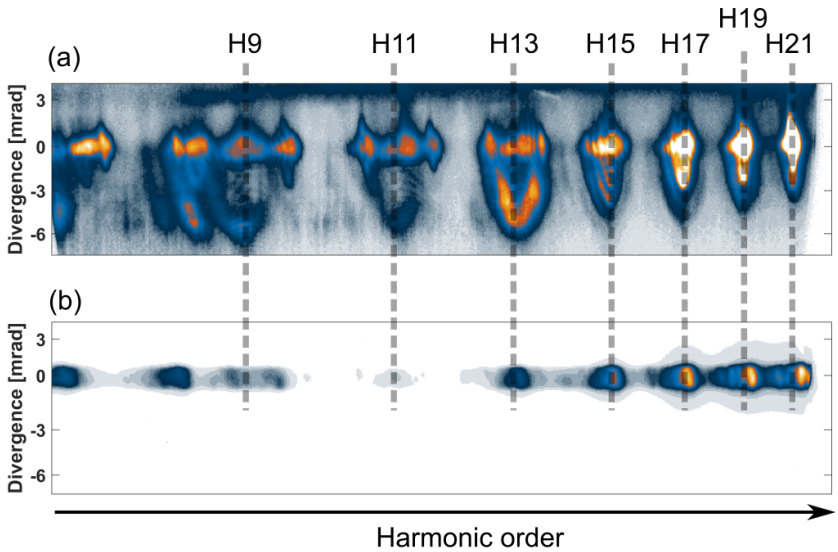

Figure 3.22: Harmonics generated in the 1 kHz HHG setup. Without trimming the harmonic spectra (top) the short trajectory contributions cover up to ± 6 mrad. In order to measure smaller redirections using the OOM technique, the iris, **I2**, is used to reduce the divergence of the spectrum to ± 1 mrad (bottom).

by tuning the laser wavelength was possible, but since the laser bandwidth was reduced, the harmonics also became more narrow. Ultimately, there was only a marginal shift of the harmonic peak positions when tuning the laser wavelength.

3.2.2 Helium 1s2p

So far, we have considered a unidirectional redirection of the XUV signal using OOM, which is the case if we have a linear and increasing intensity dependence of the Stark-shift, and an approximately linear intensity gradient spatially across the target. In principle, linear Stark-shifts only occur for the highest states of an atom. These states Stark-shift close to *ponderomotively*, as described in Eq. 2.6. The experiments described in **Paper II** were performed in helium, and demonstrated that a lower lying state, helium 1s2p, has a non-linear Stark shift. The ground state configuration of helium is $1s^2$, after the XUV excitation pulse states up to high np-manifold are coherently excited as seen in Fig. 3.24. Helium 1s2p is therefore one of the lowest excited states in the atoms.

The direction of the Stark shift of a given state depends on the density of states surrounding it. In the case of helium 1s2p, it has a higher density of states above it compared to the high-np manifold, and it will first shift towards lower energy when experiencing a weak external laser field, as shown in Fig. 3.23. When the laser field amplitude is increased it will

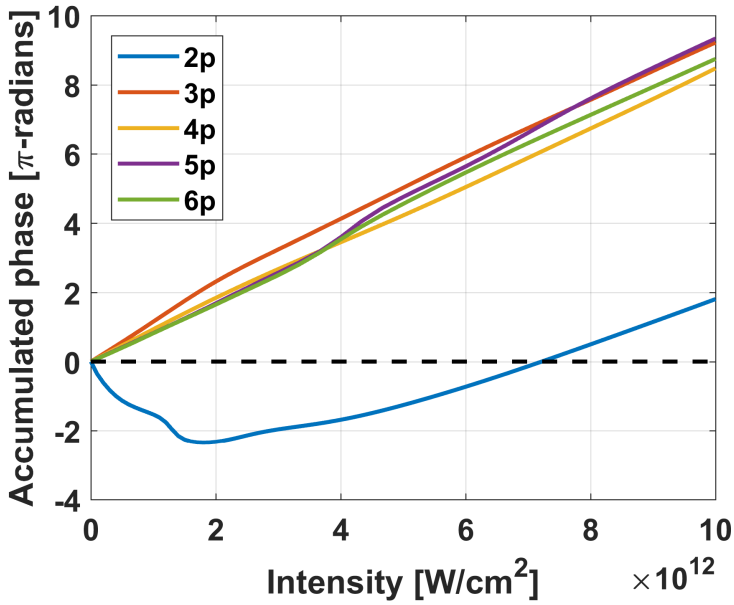

Figure 3.23: Accumulated phases for different states in helium from TDSE calculations.

then shift to higher energy, and with sufficiently high strength of the electric field, the 1s2p state will also shift ponderomotively. Fig. 3.24 shows a measured spectrum in helium where the emission from the high–np states were redirected up, and the emission from 1s2p was redirected in both directions. Harmonic 13, generated with 800 nm, was centered near 20 eV, but was blue–shifted into resonance with the 1s2p state. Harmonic 15, which is centered near 23 eV, naturally covered the higher–np manifold.

In order to determine the order of the Stark shift (either up then down, or down then up) for the 1s2p state, an intensity scan was performed, where the IR control pulse was attenuated using the iris, **I2**, from Fig. 3.20. The measurement was theoretically reproduced with coupled Maxwell wave equation TDSE simulations, displayed in Fig. 3.25. In the simulation, the XUV and IR Gaussian focal FWHM were set to 28 µm and 56 µm, respectively and spatially offset by 35 µm. The experimentally measured IR focal spot was estimated to be ∼120 µm, whereas the experimental XUV focal spot was harder to measure. The gas cell, which was attached to a 3D-translation stage, from Fig. 3.21, was replaced with a knife edge and the harmonic spectrum was measured as a function of translation of the knife edge. The estimated XUV focal spot size in the vertical direction was ∼50 µm. However, the horizontal scan varied between ∼50 µm to ∼150 µm for different back-to-back measurements. We believe that this was due to hysteresis of the vacuum edge-welded bellow, wherefore the actual size remained uncertain.

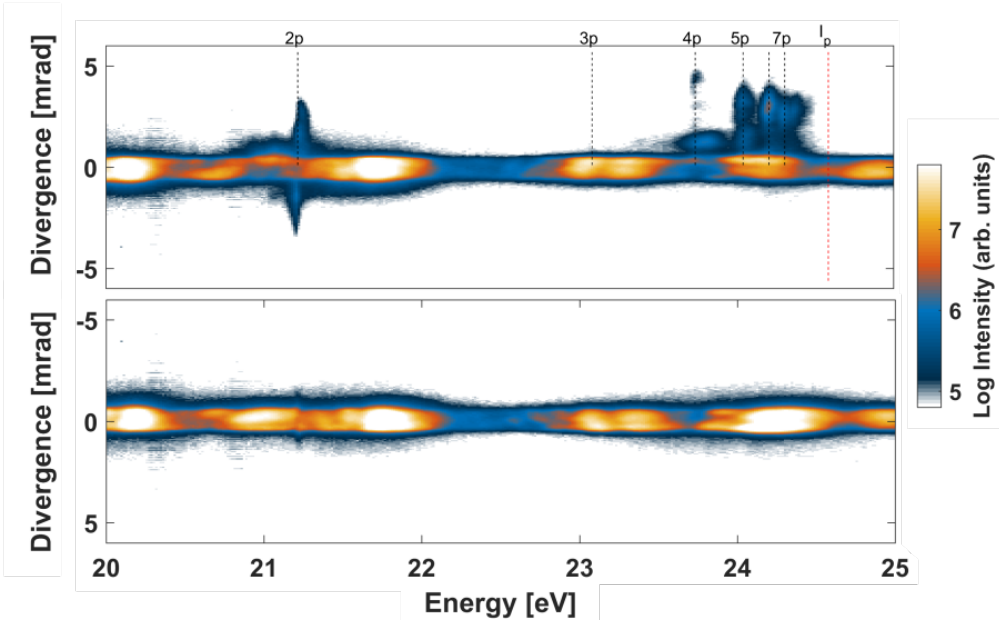

Figure 3.24: Redirection of XUV radiation with the OOM technique. The ambient pressure in the gas target chamber was $1.1 \cdot 10^{-3}$ mbar. Measurement with IR control pulse (top) and without the control pulse (bottom). The np manifold displays redirection up, whereas the 1s2p state is redirected both up and down due to its nonlinear Stark phase accumulation.

The results in Fig. 3.25 display the main features of the Stark-phase accumulation. In both the experiment and the simulation, the IR beam was located above the XUV beam. For small iris openings (low intensity), the emission from the 1s2p state in helium was first redirected down. When the iris was opened more and the laser field in the focus was increased, the emission started to also be redirected upward. These experiments show the first measurements of non-linear Stark–shifts, displaying the OOMs ability to access Stark-induced dynamics in atoms. For OOM as a technique to control light, this is also a demonstration of an XUV beam splitter controlled by an IR control pulse.

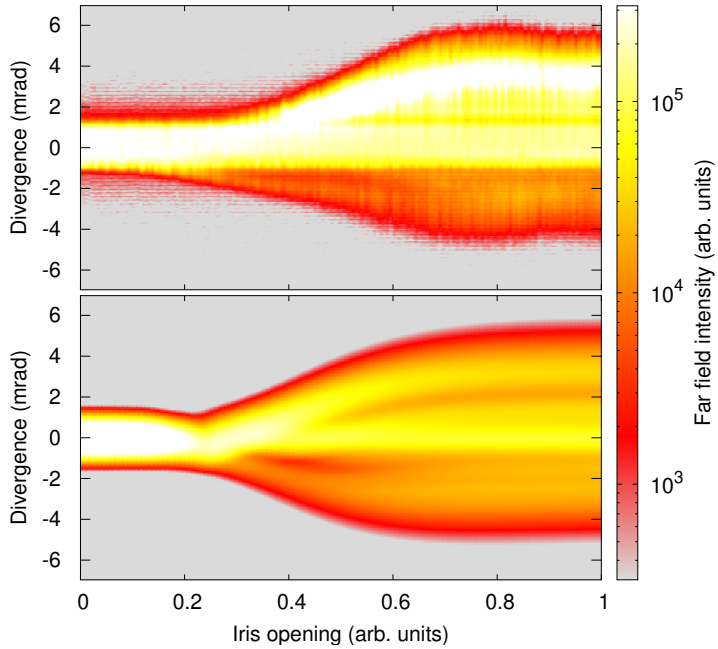

Figure 3.25: Experimental (top) and simulated (bottom) iris opening scans of the 2p deflection in the far field. The IR beam is located below the XUV beam in the near field.

3.2.3 High np self-interference

When the size of the XUV focal spot is such that the high np states in helium not only experience the linear intensity gradient of the IR, but also the nonlinear wings and crest of the Gaussian intensity distribution then the situation becomes more complicated. The high np states predominantly have a linear, positive intensity dependence as seen in Fig. 3.23. The XUV wavefront created near the wings of the Gaussian IR profile is less redirected than the XUV wavefront near the maximum of the slope of the IR intensity profile. The difference in emission direction in the near field will cause the OOM redirected light to interfere in the far field, as illustrated in Fig. 3.26.

A geometrical model was created to simulate the interference of the redirected light. The IR and XUV profiles are simulated in the near field with parameters estimated from the experimental conditions. The size and peak intensity of the IR beam is estimated from experimentally imaging the focus of the beam and measuring the average power of the laser beam. The overlap of the XUV and IR beams is optimized for maximum OOM deflection angle in the far-field, which corresponds to the XUV beam sampling the steepest intensity gradient of the IR intensity profile. The intensity dependent Stark-phase accumulation is provided from the TDSE calculations as shown in Fig 3.23. However, for the high–*np*

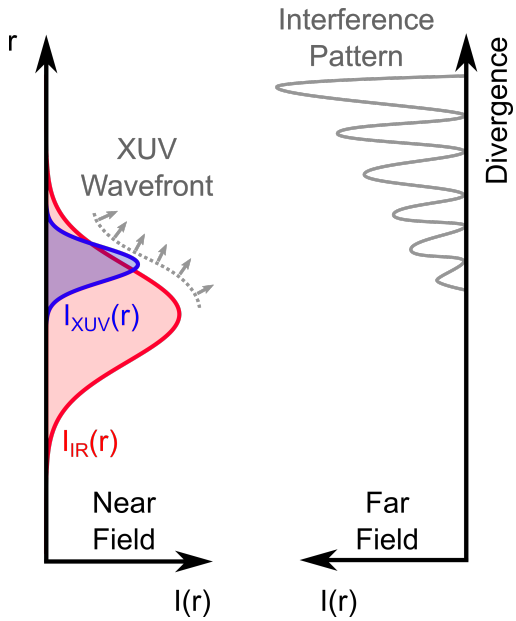

Figure 3.26: Illustration of self interference of an XUV beam that is Stark-shifted at the wings and around the crest of the Gaussian intensity distribution of the IR beam. The wavefront of the XUV beam will be non-linear in the near field, which will result in an interference pattern when observed in the far-field.

manifold we simply use the ponderomotive energy from these calculations, therefore the spatial phase in the near field can be calculated. The spatial XUV intensity profile in the far field is then calculated by Fourier transforming the spatial profile in the near field.

The comparison of the measured and experimental results are shown in Fig. 3.27. The simulated IR and XUV beams have FWHM width of 120 µm and 50 µm respectively. The offset between the beams is 50 µm. The geometrical model manages to reproduce the interference fringes in the redirected radiation. Ideally, this could potentially be used as a technique for XUV focal spot size measurements, but currently the precision of the experimentally measured parameters, such as peak intensity of the IR beam and XUV-IR beam offset, is not sufficient.

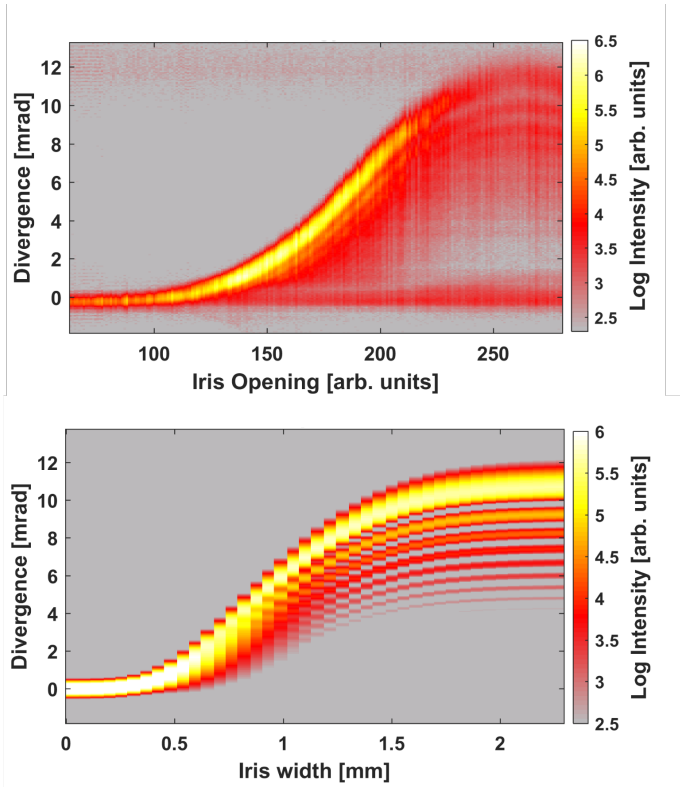

Figure 3.27: Measured deflection of the high–np manifold in helium as a function of iris opening (top). Simulated deflection of the high–np manifold in helium as a function of iris opening using the geometrical model (bottom).

3.3 Free electron laser synthesizer

FELs have the possibility to produce XUV radiation at very high intensities and with a tunable wavelength. However, compared with pulses generated with HHG, pulses from FELs are longer and less stable with respect to intensity and duration. Attosecond pulse generation with FELs has been demonstrated in SASE operation, where sub femtosecond spikes are sometimes generated by the stochastic process [73]. The SASE process relies on chance to produce these short pulses, and many of the shots are discarded with this technique. A more reliable means of generating attosecond pulse structures from FELs is desired. **Paper III** proposes a more controlled technique for producing these short pulses in a seeded FEL. Here, the electron bunches are microbunched in a first undulator, called the radiator, then successively pass a set of undulators where the main FEL radiation is produced. The radiators do not necessarily have to be set to resonantly enhance the FEL radiation at the wavelength of the seeding laser that is used for microbunching. Instead,

they can generate any integer harmonic of the seeding laser. The work in **Paper III** focused on synthesizing temporal waveforms by generating different harmonics in the radiators, and controlling the amplitude and phase between them. This is the same principle as illustrated in Fig. 2.1.

It has been demonstrated previously that the harmonics generated in the radiators have a phase relation that can be controlled in order to create an asymmetric XUV field [74]. The experiment in **Paper III** extends this technique to create a train of sub femtosecond pulses using an FEL. In the experiment the third harmonic of a 780 nm IR laser was used to seed the electron bunch in the modulator. Three radiators were set resonant to the 7th, 8th and 9th harmonic of the 260 nm seeding laser. Phase shifters between the radiators allowed for individual control of a harmonics phase with respect to the other generated harmonics. By choosing different phase relations between the harmonics it therefore became possible to create a train of pulses using three harmonics. One challenge now was to measure the sub-femtosecond temporal structures when the jitter between the FEL generated XUV and a reference laser is $\sim$6 fs.

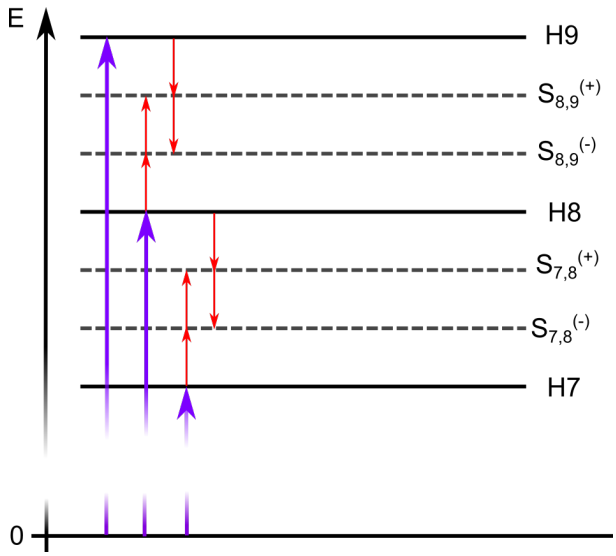

Figure 3.28: Illustration of the energy level diagram of the generated photo-electrons for the FEL synthesizer experiment. The photo-electrons can absorb either just the harmonics, H7, H8, H9, or a harmonic and IR photons. The number IR photons absorbed (one or two) determine the emission direction of the photo-electron. To determine the phase between the harmonics, the correlation of the side-band signals, $S_{7,8}^{(\pm)}$ and $S_{8,9}^{(\pm)}$, are measured.

A group from the University of Freiburg developed a technique in **Paper III**, to resolve the attosecond pulses with jitter between the IR and XUV pulse which is $\sim$6 fs. The meas-

urement relies on a method, similar to RABBITT (Reconstruction of Attosecond Beating By Interference of Two-photon Transitions) [12, 75, 76], where an atom is irradiated by an XUV pulse and an IR pulse at the same time. This is typically a HHG technique, where an IR beam and odd harmonic orders of the IR are absorbed by an atom, emitting photo-electrons. The emitted photo-electrons can be released either by absorbing a photon of the harmonic $q\omega$, by absorbing a photon of the harmonic and one from the IR beam $q\omega + \omega$, or by absorbing a photon of the harmonic and emitting a photon $q\omega - \omega$.

In RABBITT performed with HHG, the spacing between consecutive harmonics is two IR photons. Spectrally resolved, these photo-electrons generate a *side-band* between the consecutive odd harmonic orders. Since there are two different quantum paths to reach the same energy, *e.g.*, $q\omega + \omega$ and $(q+2)\omega - \omega$, the side-band signal oscillates depending on the phase difference between the harmonics $q\omega$, $(q+2)\omega$ and the IR field.

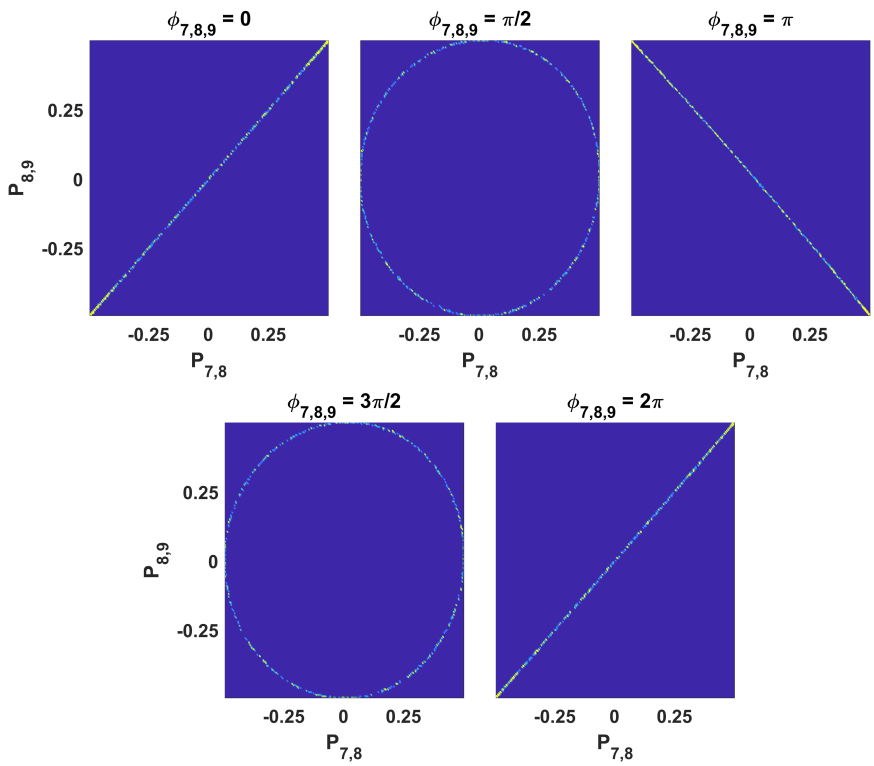

Figure 3.29: Correlation plots simulated with SFA for different phase relations between the harmonics H7, H8 and H9.

In the FEL experiment described in **Paper III**, the spacing between consecutive harmonic orders was three IR photons, which means that there were two side-bands between each

consecutive harmonic as seen in Fig. 3.28. If we consider two harmonics, H8 and H9, then the photo-electrons in one of the side-bands, $S_{8,9}{}^{(\pm)}$, can interact with either H8 or H9, but this would require an interaction with either one or two IR photons depending on which harmonic was absorbed by the atom. This difference in photon parity for the two side-bands, $S_{8,9}{}^{(\pm)}$, results in opposite emission direction of the photo-electrons, the phase of the IR with respect to the harmonics then determines the probability of which side-band is favored. By measuring the photo-electron signal of the side-bands in one emission direction, the signals of $S_{8,9}{}^{(+)}$ and $S_{8,9}{}^{(-)}$ are always anti-correlated since they interact with the same source of IR photons.

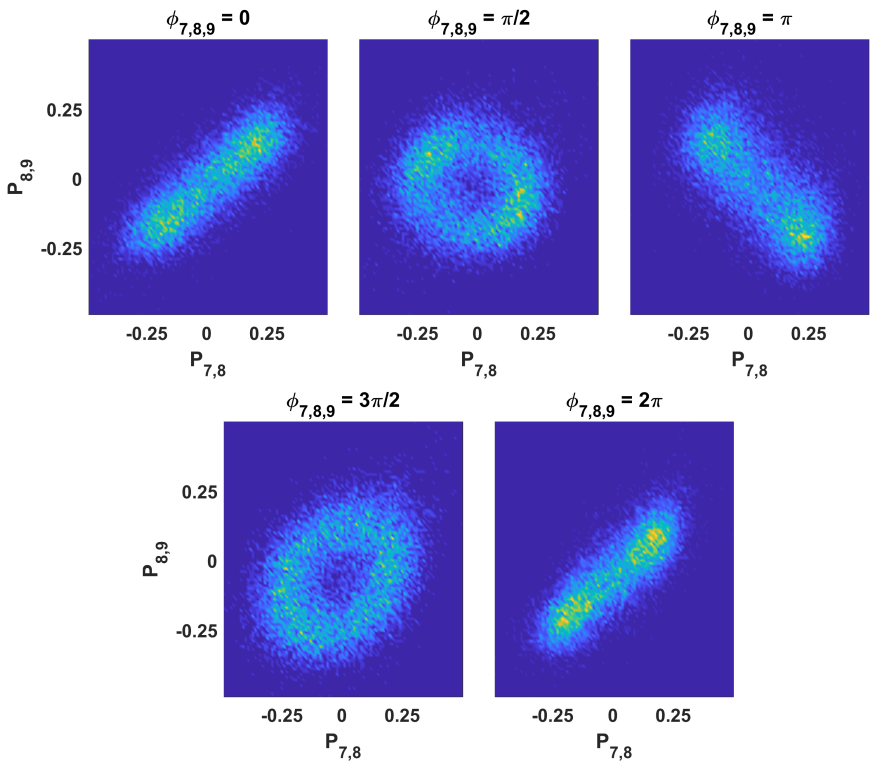

Figure 3.30: Correlation plots measured in a neon gas target for different phase relations between the harmonics H7, H8 and H9.

If we consider three harmonics instead, H7, H8 and H9, and measure the signal of both side-band pairs, $S_{7,8}{}^{(\pm)}$ and $S_{8,9}{}^{(\pm)}$ between the harmonics, then the signals correlation would be dependent on the phase between these harmonics. If all harmonics are in phase, the correlation would be positive. If all harmonics are out of phase with respect to each other, $\Delta\phi_{7,8,9} = \pi$, then the side-band signals will be anti-correlated. By measuring the

correlation between the side-band signals, the need for sub-cycle resolution of the delay between the XUV and IR is eliminated. The relative phase of the harmonics can instead be retrieved from the measured correlation patterns, as shown in Fig. 3.29.

The experiment was performed at the Low Density Matter beamline at FERMI. Part of the IR beam (before the third harmonic up-conversion for the seed pulse) was split off and recombined with the XUV harmonics generated with the FEL in a neon gas target. The photo-electrons were measured with a magnetic bottle electron spectrometer optimized for a 2π steradian collection angle. The delay of the IR with respect to the XUV beam was set to zero and the natural jitter between the IR and XUV beams maps the delays between the pulses. The resulting correlation plots, shown in Fig. 3.30, were performed for various phase relations between the three harmonics. From these measurements, since the spectral phase and shape of the XUV harmonics was known, it was possible to reconstruct the temporal profile of the pulses. The measurements in **Paper III** show that pulses reconstructed with this method were expected to be shorter than 1 fs. To date, this is the only technique where attosecond pulse trains can be consistently produced with an FEL.

3.4 Nitrogen air lasing

Compared with HHG and FELs, nitrogen air lasing does not produce light the VUV region. The technique still relies on a femtosecond laser to create a UV beam with properties that can be governed by controlling the IR beam. Focusing an intense femtosecond laser with an 800– nm wavelength in nitrogen may produce directional, coherent forward emission at 391 nm. Under the conditions where this radiation is generated, the IR laser is strong enough to create a filament [77], and ionize the nitrogen molecules. The 391– nm emission is resonant with the transition from the second excited state $B^2\Sigma_u^+$ to the ground state $X^2\Sigma_g^+$ of the singly excited nitrogen molecule, N_2^+. Injecting a weak seed at the 391 nm together with the 800 nm laser, can amplify the seed intensity by two orders of magnitude.

The mechanism of this optical gain is currently still not understood, and it is debated whether population inversion between the ground state and the excited state is required for the enhancement of the 391 nm emission. According to certain theories, population inversion can be achieved by radiative transfer from the ground state to the excited state by the driving IR laser [78, 79]. In another interpretation, the inversion can be attined due to electron recollisions with the nitrogen ions [27].

Paper IV describes the testing of the recollision model. From previous experiments it is known that the ellipticity dependence of the 391– nm forward emission is similar to the ellipticity dependence of HHG [27, 80]. For the study presented in **Paper IV**, the carrier wavelength dependence was instead tested. Provided that recollision plays an important

role in nitrogen air lasing, the central wavelength of the driving laser field can not be an even integer number of the 391 nm radiation. This follows the same principle as in Sec. 2.2.1, *i.e.*, if the central wavelength of the laser is 782 nm, 391 nm would be its second harmonic. Since the laser in this case can not produce this energy, there is no contribution to the population inversion.

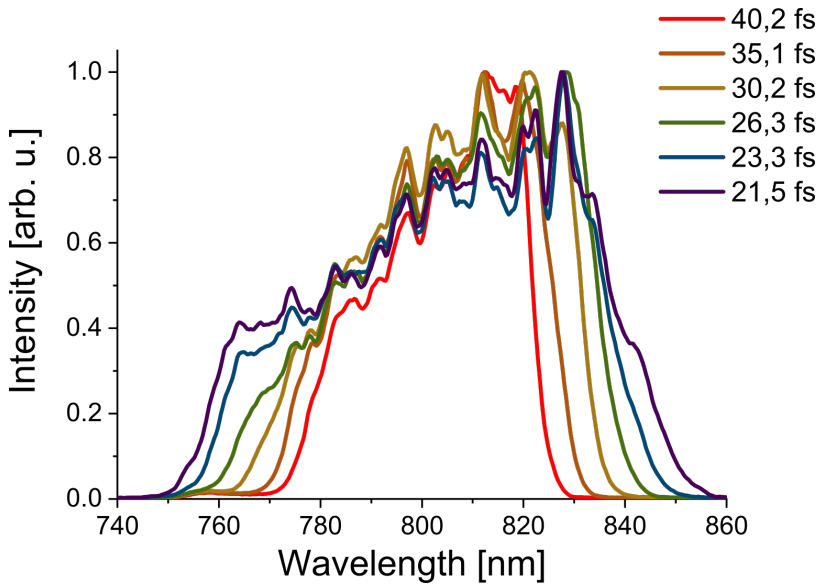

Figure 3.31: Measurements of the spectra using the spectrometer (Ocean Optics, HR4000) for different pulse durations. Figure courtesy of Penji Ding.

In order to test how well a recollision model describes the phenomena, a two–dimensional scan was performed where the pulse duration and central wavelength was tuned. From Fig. 3.32 (b), one would expect to always have a minimum of the 391 nm signal when the driving laser had the wavelength 782 nm. By tuning away from 782 nm, an increase of the 391 nm signal would be presumed and eventually a peak should be reached. The position of this peak would depend on the pulse duration: provided that the pulses were very long, the peak would be located at an odd order harmonic of 391 nm, whereas if the pulses were fairly short, small maxima would appear between the even- and odd-order harmonics. By scanning the wavelength for different durations of the driving laser field it should be possible to measure the signal peak shift.

The experiment was performed with the 1–kHz HHG setup. For these tests, only the probe arm of the interferometer was used. The application chamber was filled with 5 mbar of nitrogen, instead of using the pulsed gas cell. To avoid filling the interferometer chamber with nitrogen, a window port valve between the torodial mirror and application chamber can be closed. The AOMs of the laser were used to change its gain bandwidth and central

wavelength. Since the bandwidth of the laser was limited to 100 nm, as described in Sec. 2.1.2, the scan range was confined between 750 nm and 850 nm. This meant that the 20–fs pulses had no scan range, since they used the entire bandwidth, whereas the central wavelength of a 40–fs pulse could be tuned between 780 nm to 820 nm. The recorded spectra for varying pulse durations, when centered at 800 nm, are shown in Fig. 3.31

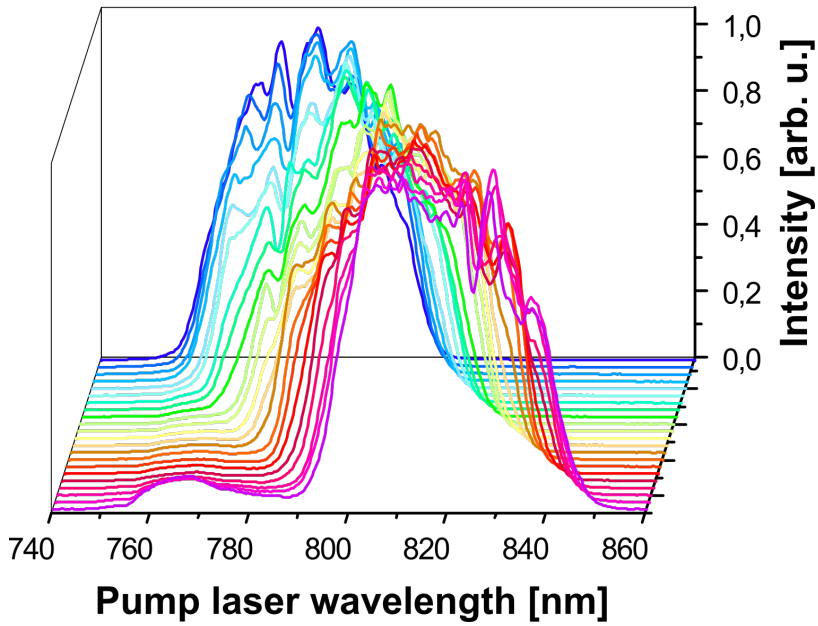

Figure 3.32: Measurements of the spectra using the spectrometer (Ocean Optics, HR4000) for different central wavelengths. The small peak near 750 nm for the higher central wavelengths of the IR pulse is assumed to stem from amplified spontaneous emission, and is therefore incoherent. Figure courtesy of Penji Ding.

Fig. 3.32 displays the recorded spectra from a wavelength scan, using a visible-IR spectrometer (Ocean Optics, HR4000). The DAZZLER was used to control the gain bandwidth and shift the central wavelength position. The WIZZLER is used to correct the phase of the pulses after the DAZZLER in order to transform–limit them. This phase correction often alters the spectral profile, wherefore the procedure was performed a few times until the spectrum measured with the spectrometer was visibly shifted.

The shape of the spectrum affected the 391– nm signal in our experiments: if the spectrum went from a top-hat to a Gaussian distribution between wavelength scans, there was low reproducibility of the 391 nm signal. The spectral shape of the IR pulses was therefore controlled by suppressing parts of the spectrum with a programmable gain *hole* with the DAZZLER. More effort was put into retaining the shape of the spectrum than the position of the central wavelength, as the actual position of the central wavelength was retrieved by

finding the spectral center of mass after the experiments. In Fig. 3.32, there was a small signal peak near 770 nm when the central wavelength is tuned to 820 nm. This signal was assumed to come from amplified spontaneous emission, and did therefore not participate in the nitrogen lasing process as it is incoherent.

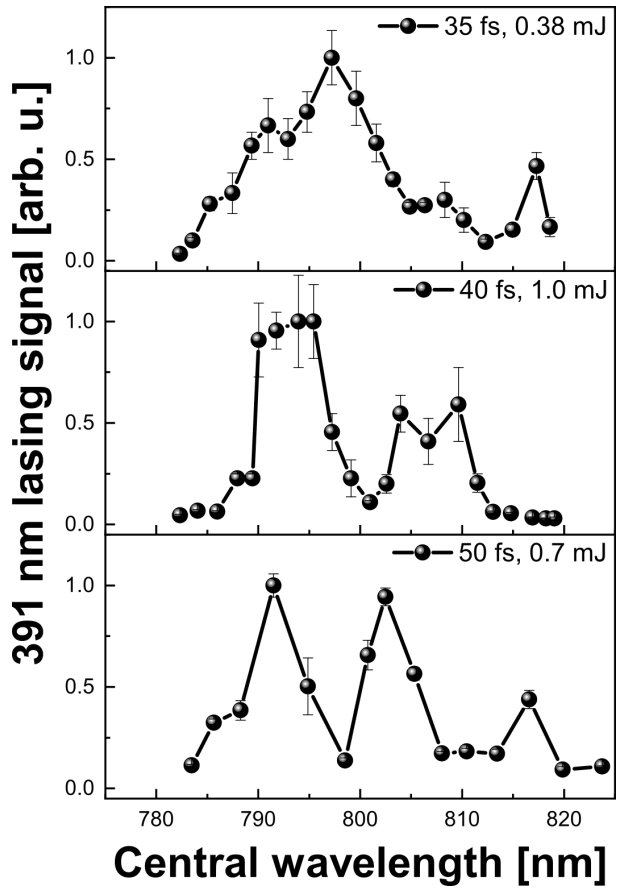

Figure 3.33: Wavelength scans performed for three different pulse durations: 35 fs (top), 40 fs (middle) and 50 fs (bottom). The central wavelength position is calculated from the center of mass of the spectra. The measurements display an increase of peaks, and a decrease of peak separation for increasing pulse duration. These results are expected if a recollision process is participating in the 391 nm signal generation. Figure courtesy of Penji Ding.

The results of the wavelength scans are shown in Fig. 3.33 for IR pulse durations of 35, 40 and 50 fs. As predicted, a minimum was always found near 782 nm. The peak position of the first maximum on the red side shifted towards 782 nm as a function of increasing pulse duration.

These results were consistent with the theory of a multi periodic recollision process as described in Sec. 2.2.1: the 391– nm signal would be the second harmonic of the driving laser if the laser is centered at 782 nm. At this wavelength, since both the target gas medium and the laser field are inversion symmetric, the laser could not populate the excited state in the nitrogen ions through a recollision process. Since the laser pulses are fairly short (tens of cycles), secondary interference maxima are presumed to exist between the consecutive odd harmonics, as displayed in Fig. 2.5 (c). The spacing between these secondary maxima is dependant on the duration of the laser pulse, which is what gives rise to the duration dependant oscillations of the 391– nm signal.

Chapter 4

Summary and Outlook

The experiments presented in this thesis aim to demonstrate control of light in the UV- to XUV regimes. Each of the light sources used in this thesis work have properties which outperform the other sources: HHG is a compact source, producing very large bandwidths and short pulse durations, FELs produce the highest pulse intensities and the wavelength is fully tunable, nitrogen air lasing can be used for remote sensing in atmospheric conditions.

These light sources also have their individual disadvantages: the intensity of the light produced through HHG is low, pulses produced by FELs are too long for attosecond measurements, and nitrogen air lasing process is not yet fully understood in order to be used for remote measurements. Our experiments demonstrate steps forward for these techniques by performing low-loss control of HHG radiation, sub-fs pulse generation with FELs and investigative experiments in order to understand nitrogen air lasing. Science is often done by a number of small increments; the techniques presented in this thesis are mainly a proof-of-concept, driven by their potential for future applications. Since fundamental demonstration of these control techniques has been performed, it is now interesting to further develop the reliability and versatility of these methods for applications.

Nitrogen lasing

Nitrogen air lasing is a complicated phenomenon, where more than just one "key" process participates in the generation of the 391– nm emission. Experiments to understand these processes and their impact on the generation are driven by the possible utility of this technique for remote sensing. Since the emission is bi-directional it can be used to induce a coherent backwards propagating beam at an arbitrary distance in the atmosphere.

The experiment presented in **Paper IV** tested whether a recollision model, similar to that of HHG, could be responsible for populating the excited state in the nitrogen ions, by measuring the intensity of the 391– nm signal as a function of pulse duration and central wavelength of the driving laser. The results showed a periodic oscillation of the 391– nm signal intensity as a function of central wavelength, which was always at a minimum when the driving field wavelength is exactly twice as long as the signal wavelength. The periodicity was increased with increasing pulse duration. These results indicated that the behaviour of the nitrogen air lasing can be explained by a recollision process, however, they did not directly exclude the contribution of other processes to the emission.

Phase control during HHG

In the QPI experiments, the phase difference between the quantum trajectories give an insight into the sub-cycle dynamics of the HHG process. With the Gaussian beam simulation it was possible to estimate the phase accumulation as a function of intensity and therefore apply limited control to the spatio-temporal phase *during* the HHG process. The semi-classical interpretation of the phase accumulation allowed for intuitive understanding of the process. Recently, other research groups have investigated more phenomenological interpretations of the harmonic phase accumulation, in order to predict the positions of the harmonic foci, and possibly to control their position [81, 82]. Since there are no efficient optics for radiation in the XUV regime, controlling the phase front during HHG offers a solution without the use of XUV optics.

The presented chirp-scan technique allowed for reconstruction of the intensity dependent dipole phase of the HHG process. In our experiments, we demonstrated that the dipole phase accumulation can be both positive and negative. In addition, it was possible to pinpoint in our measurements the turning point of the phase accumulation, where the harmonics became insensitive to the applied intensity. This is to the best of our knowledge the first measurements of anomalous intensity–dependent dipole phases in HHG. Introducing a third source term in the simulations provided an improved visual match with experimental chirp-scan measurements. When retrieving the intensity dependent dipole phase parameter of this third source term, it appeared to diverge from the dipole phase term of the long–trajectory contribution, as a function of increasing harmonic order. This behavior can be explained by a third electron trajectory from the semi-classical three step model. Proof of the presence of the third trajectory can however not be made from these measurements alone; additional experiments have to be performed in order to deduce the origin of this third source contribution.

It would be interesting to reproduce the retrieval of the dipole–phase parameters using a tunable wavelength source, such as an optical parametric amplifier. The harmonics in our

experiments present a window where the interference from our long multi–cycle pulses is constructive. This is beneficial in our experiments since each harmonic, when spectrally resolved, is well separated from the consecutive harmonics, thus avoiding interference from the neighbouring harmonics on the detector. However, the separation between each harmonic is large which makes it hard to follow the evolution of the dipole–phase parameters as a function of wavelength. By having a tunable source for HHG it would be possible to continuously, and more reliably, retrieve the dipole–phase parameters. Additionally, mapping these parameters close to, or even below, the ionization potential might reveal interesting dynamics. The harmonics with energy below the ionization potential can not be explained with the classical three step model, and the notion of classical trajectories becomes abstract. Therefore it would be interesting to see the behavior of the intensity–dependant dipole–phase parameters in this regime.

Phase control after HHG

Using the OOM techniques it is possible to retrieve the accumulated Stark-phase of different energy levels in atoms. The OOM also provides a way to steer XUV light using an IR control beam. Since conventional optical components do not work efficiently in this wavelength regime, OOM demonstrates an alternative method for light manipulation. The response time of OOM is dependent on the pulse duration of the IR pulse, which is faster than any acusto- and electro-optical modulators, allowing for ultrafast beam redirection [83].

Future experiments aim to implement spatial light modulators, increasing the amount of control when tailoring the IR control pulses, and increasing the amount of control pulses. With these additions to the OOM toolbox it would be possible to perform synchronized operations using XUV radiation. For example, two IR pulses can be used to redirect the OOM onto a target for a controlled period of time, creating an XUV source with a tunable pulse duration. Two IR pulses can also be offset on either side of the XUV pulse. This would technically focus the XUV emission at a distance which can be controlled by the intensity of the IR pulses.

OOM has been demonstrated with XUV from HHG, but it may also be implemented at FEL–facilities. The principle would remain the same, where the XUV from an FEL would be absorbed in a gas target after the generation process. An IR pulse would then be overlapped, off-centered in order to redirect the XUV light. By using two IR pulses, it would be possible to redirect the beam from the propagation axis using the first pulse, and redirecting it back with the second pulse. By doing this, it might be possible to switch out an XUV pulse that has a very small jitter compared to the control pulses. Alternatively, the IR pulses could be injected at an off–axis angle with respect to the XUV pulses that are

generated by an FEL. In this off–axis configuration it might be possible to redirect an XUV beam to co–propagate with the IR control pulse.

Temporal phase control in FEL

The experiments with OOM do present a method for low-jitter short pulse genereation that could be used for FELs. The experiments portrayed in **Paper III**, however, demonstrate a more direct and controlled method for producing attosecond pulse trains using a seeded FEL. An interesting conclusion that was drawn from these experiments was that the degree of phase control of the XUV radiation was superior to the HHG process. The FEL synthesizer technique provided full control of the amplitude and temporal phase of the individual XUV harmonics, which is not possible in HHG.

With the technique described in **Paper III** it is possible deduce the relative phase of the XUV and the IR beams within one cycle of the IR pulse with attosecond precision, which enables phase–resolved interferometric measurements to be performed with FELs. Such experiments, which usually were confined to HHG sources, can now be performed at much higher intensities and shorter wavelengths. This type of control also opens the door for coherent control experiments in the XUV regime [74].

Acknowledgements

During my time here at the Atomic Physics Division in Lund, I have had the pleasure of working with some exceptional people without whom this work would not have been possible.

First and foremost, I would like to thank my main supervisor, Johan Mauritsson. Not only for supervising me during my PhD work, but also when i was a bachelor's- and master's-student. During my time in your group I have had the opportunity to work with very interesting and fun experiments, and when things did not seem to work you have always managed to know in what direction to steer the group efforts. I would like to thank my assisting supervisors, Lars Rippe and Cord Arnold for always having time to discuss things which I found to be unclear, and for providing helpful input. I would like to express my gratitude to my third assisting supervisor, Emma Simpson, who has (aside from supervising me) performed much of the experimental work together with me.

A huge thank you to the past and present people in the Attosecond XUV Spectroscopy group, with whom I have been working with for the past years. Esben, for being my co-supervisor when i was an undergraduate student and for the fun times we had working together. Samuel, for being overly cheerful and kind. It is also impressive how efficient you are in the lab once the sun sets. Thank you Anna, for not being like Samuel (you are efficient and kind though). Thank you Stefanos for having the patience and trying to explain theory to me. Thank you Ello for making me feel included when i just started in the group. I have also had the pleasure of supervising two Master's students during my time in the group, Simon Ek and Timothé Ramboazanaka, their work significantly contributed to the experiments and the data analysis. Thank you guys, and great job!

I would also like to extend my thanks the people currently in the full atto-group. Professors Anne L'Huiller and Per Johnsson I thank for being available when I had questions. Thank you Mathieu Gisselbrecht for nice long discussions about life in general and Anders Persson for sharing your experience. Thanks to David Busto for constantly disagreeing with me, I never knew I needed this in my life. Thanks to Fabian Langer for all the regular conversations, which we rehearsed beforehand. Thank you Sylvain Maclot, for all the nice

food and activities at your place. Lana Neoricic, you also organized this with Sylvain, but I would like to thank you for supporting my spanish, even when it was nonsense. Thank you Ivan Sytsevich for the constant supply of mind-boggling t-shirts and hoodies you are sporting. Thank you Jasper Peschel for excellent sauna company, and for organizing the journal clubs. Thank you Robin Weissenbilder for somehow managing to always disagree with me *and* David at the same time. I have no idea how you pull this off. Thank you Chen Guo, for all the Chinese words you've taught me over the past seven years, I know at least 10 right now! Thank you Diego Guenot for all the french slang you've taught me. Thank you Anne-Lise Viotti for all the coffees we've managed to have during your short stay here. Shiyang Zhong for your impressive competence. Hugo Dacasa, I am very impressed by your dedication to Burgundy Monday, thank you. Thank you Sara Mikaelsson for always helping me when I have a question. Thank you Hugo Laurell and Maria Hoflund for being so respectful and kind. And finally, Jan Vogelsang, you never want to join for lunch, but that one time where you joined was one of my all time favourite lunches.

Of course, there people outside of the atto-group at the division which I would like to thank. I'd like to thank Alexander Permogorov for... well, for being yourself, Sebastian Hovrath for keeping me safe and David Hill for giving us riddles (almost) every day. Thank you Jonas Björklund Svensson for normalizing danish culture. Thank you Giada Contono for bringing some nice Italian anger to cold sweden, Åsa Bengtsson for the nice times we've had teaching together, Xiaocui Wang for interesting discussions, Hafsa Syed for always being cheerful and Adam Kinos for warming up the lights at the department before people come in for work.

I would like to thank the people that were working here when I started but finished before me. Thank you Maite for being such a great friend. Thank you Miguel showing me the barren lands of Portugal, and for your inhuman calmness. Jan Lahl, mein mensch, thank you for teaching me the proper rules of German drinking games. Filippo Campi for making fun of the Italians, so that we know how to do it properly. Thank you Yu-chen Cheng, for your amazing singing voice and for taking your time making sure that I've gotten the help I needed for whenever I asked you for help. Thank you Hélène Coudert-Alteirac for all the fun discussions we had. Thank you Piotr Rudawski for being so extremely kind and humble. Anne Harth, you were also always kind and humble, and I admire your passion for physics, thank you for that. Thank you Saikat Nandi for being helpful and professional. I would like to thank Linnea Rading for all the ping-pong games we had, Marcus Isinger for being so calm and courteous at all times, and David Kroon and Marija Kotur for the nice company during all the dissertation parties.

The great work environment at the Atomic Physics Division in Lund can of course be attributed to all the people that work here, but i believe that a lot of work has been done by the head of the division, Professor Claes-Göran Wahlström, to support such an open, friendly atmosphere here at the department, thank you Claes-Göran. I would like to thank

the administrative staff at the division, not only for making sure that I am not having problems that I am not supposed to have, but also for being really nice people. Thank you Jakob, for all the hours you've spent teaching me some hilarious recent Swedish history. Thank you Anne Petersson Jungbeck, for all the coffee breaks where you care to speak your mind. Thank you Åke Johansson, for all the interesting philosophical discussions we have had. Additionally, I would like to thank Lars Engström for managing the teaching and Andreas Walther for helping me manage the study plans as a PhD student.

Finally, I would of course like to thank all my friends and family for being so supportive. You know who you all are and how much I appreciate you, so I won't have to list you. But I will explicitly thank my parents, Jadranka Orascanin and Enver Ibrakovic, they can't read English but I think they might be happy to see their names here.

References

[1] T. H. Maiman. Stimulated optical emission in Ruby. *J. Opt. Soc. Am.*, **50**:1134, 1960.

[2] A. Zewail. Femtochemistry: Atomic-Scale Dynamics of the Chemical Bond. *J. Phys. Chem. A*, 104:5660, 2000.

[3] P. A. Franken, A. E. Hill, C. W. Peters, and G. Weinreich. Generation of optical harmonics. *Phys. Rev. Lett.*, 7:118, 1961.

[4] D. E. Spence, P. N. Kean, and W. Sibbett. 60-fsec pulse generation from a self-mode-locked Ti:sapphire laser. *Opt. Lett.*, **16**:42, 1991.

[5] J. J. Rocca, V. Shlyaptsev, F. G. Tomasel, O. D. Cortázar, D. Hartshorn, and J. L. A. Chilla. Demonstration of a discharge pumped table-top soft-x-ray laser. *Physical Review Letters*, 73(16):2192–2195, oct 1994.

[6] V. N. Shlyaptsev, G. Avaria, M. Grisham, Jing Li, F. Tomasel, M. Busquet, and J. J. Rocca. Capillary discharge x-ray lasers: The quest for sub-10 nm lasers. In *Springer Proceedings in Physics*, pages 103–112. Springer International Publishing, sep 2015.

[7] Chris D. Decker and Richard A. London. Designs for a compact ni-like-tungsten x-ray laser. *Physical Review A*, 57(2):1395–1399, feb 1998.

[8] A. McPherson, G. Gibson, H. Jara, U. Johann, T. S. Luk, I. A. McIntyre, K. Boyer, and C. K. Rhodes. Studies of multiphoton production of vacuum-ultraviolet radiation in the rare gases. *J. Opt. Soc. Am. B*, **4**:595, 1987.

[9] M. Ferray, A. L'Huillier, X.F. Li, L.A. Lompre, G. Mainfray, and C. Manus. Multiple-harmonic conversion of 1064 nm radiation in rare gases. *J. Phys. B*, **21**:L31, 1988.

[10] M.-C. Chen, P. Arpin, T. Popmintchev, M. Gerrity, B. Zhang, M. Seaberg, D. Popmintchev, M. M. Murnane, and H. C. Kapteyn. Bright, coherent, ultrafast soft x-ray

harmonics spanning the water window from a tabletop light source. *Phys. Rev. Lett.*, 105:173901, Oct 2010.

[11] Ph. Antoine, A. L'Huillier, and M. Lewenstein. Attosecond Pulse Trains Using High-Order Harmonics. *Phys. Rev. Lett.*, 77:1234, 1996.

[12] P.M. Paul, E.S. Toma, P. Breger, G. Mullot, F. Augé, Ph. Balcou, H.G. Muller, and P. Agostini. Observation of a train of attosecond pulses from high harmonic generation. *Science*, 292:1689, 2001.

[13] R. Kienberger, E. Goulielmakis, M. Uiberacker, A. Baltuška, V. Yakovlev, F. Bammer, A. Scrinzi, Th. Westerwalbesloh, U. Kleineberg, U. Heinzmann, M. Drescher, and F. Krausz. Atomic transient recorder. *Nature*, 427:817, 2004.

[14] G. Sansone, E. Benedetti, F. Calegari, C. Vozzi, L. Avaldi, R. Flammini, L. Poletto, P. Villoresi, C. Altucci, R. Velotta, S. Stagira, S. De Silvestri, and M. Nisoli. Isolated single-cycle attosecond pulses. *Science*, 314:443, 2006.

[15] F. Krausz and M. Ivanov. Attosecond physics. *Rev. Mod. Phys.*, 81(1):163–234, 2009.

[16] A L Cavalieri, E Goulielmakis, B Horvath, W Helml, M Schultze, M Fieß, V Pervak, L Veisz, V S Yakovlev, M Uiberacker, A Apolonski, F Krausz, and R Kienberger. Intense 1.5-cycle near infrared laser waveforms and their use for the generation of ultra-broadband soft-x-ray harmonic continua. *New Journal of Physics*, 9(7):242–242, jul 2007.

[17] J. Li, X. Ren, Y. Yin, K. Zhao, A. Chew, Y. Cheng, E. Cunningham, Y. Wang, S. Hu, Y. Wu, M. Chini, and Z. Chang. 53-attosecond X-ray pulses reach the carbon K-edge. *Nat. Commun.*, 8:186, Aug 2017.

[18] D. A. G. Deacon, L. R. Elias, J. M. J. Madey, G. J. Ramian, H. A. Schwettman, and T. I. Smith. First operation of a free-electron laser. *Physical Review Letters*, 38(16):892–894, apr 1977.

[19] J.B. Murphy and C. Pellegrini. Free electron lasers for the XUV spectral region. *Nuclear Instruments and Methods in Physics Research Section A: Accelerators, Spectrometers, Detectors and Associated Equipment*, 237(1-2):159–167, jun 1985.

[20] R. Bonifacio, L. De Salvo Souza, P. Pierini, and E.T. Scharlemann. Generation of XUV light by resonant frequency tripling in a two-wiggler FEL amplifier. *Nuclear Instruments and Methods in Physics Research Section A: Accelerators, Spectrometers, Detectors and Associated Equipment*, 296(1-3):787–790, oct 1990.

[21] L. H. Yu. Generation of intense uv radiation by subharmonically seeded single-pass free-electron lasers. *Phys. Rev. A*, 44(8):5178–, October 1991.

[22] Yi Liu, Yohann Brelet, Guillaume Point, Aurélien Houard, and André Mysyrowicz. Self-seeded lasing in ionized air pumped by 800 nm femtosecond laser pulses. *Optics Express*, 21(19):22791, sep 2013.

[23] A. Dogariu, J. B. Michael, M. O. Scully, and R. B. Miles. High-gain backward lasing in air. *Science*, 331(6016):442–445, jan 2011.

[24] A. Baltuška, Th. Udem, M. Uiberacker, M. Hentschel, E. Goulielmakis, Ch. Gohle, R. Holzwarth, V. S. Yakovlev, A. Scrinzi, T. W. Hänsch, and F. Krausz. Attosecond control of electronic processes by intense light fields. *Nature*, **421**:611, 2003.

[25] S. Bengtsson, E. W. Larsen, D. Kroon, S. Camp, M. Miranda, C. L. Arnold, A. L'Huillier, K. J. Schafer, M. B. Gaarde, L. Rippe, and J. Mauritsson. Space–time control of free induction decay in the extreme ultraviolet. *Nature Photonics*, 11(4):252–258, mar 2017.

[26] Samuel Bengtsson and Johan Mauritsson. Ultrafast control and opto-optical modulation of extreme ultraviolet light. *Journal of Physics B: Atomic, Molecular and Optical Physics*, 52(6):063002, mar 2019.

[27] Yi Liu, Pengji Ding, Guillaume Lambert, Aurélien Houard, Vladimir Tikhonchuk, and André Mysyrowicz. Recollision-induced superradiance of ionized nitrogen molecules. *Physical Review Letters*, 115(13), sep 2015.

[28] I. J. Kim, C. M. Kim, H. T. Kim, G. H. Lee, Y. S. Lee, J. Y. Park, D. J. Cho, and C. H. Nam. Highly Efficient High-Harmonic Generation in an Orthogonally Polarized Two-Color Laser Field. *Phys. Rev. Lett.*, 94:243901, 2005.

[29] T. Pfeifer, L. Gallmann, M. J. Abel, D. M. Neumark, and S. R. Leone. Single attosecond pulse generation in the multicycle-driver regime by adding a weak second-harmonic field. *Opt. Lett.*, 31:975, 2006.

[30] P. F. Moulton. Spectroscopic and laser characteristics of ti:al_2o_3. *J. Opt. Soc. Am. B*, 3(1):125–133, Jan 1986.

[31] D. Strickland and G. Mourou. Compression of amplified chirped optical pulses. *Opt. Commun.*, **56**:219, 1985.

[32] P. Tournois. Acousto-optic programmable dispersive filter for adaptive compensation of group delay time dispersion in laser systems. *Opt. Commun.*, **140**:245, 1997.

[33] V. Petrov and F. Noack. Mid-infrared femtosecond optical parametric amplification in potassium niobate. *Optics Letters*, 21(19):1576, oct 1996.

[34] Sergei Antipov, Darren D. Hudson, Alexander Fuerbach, and Stuart D. Jackson. High-power mid-infrared femtosecond fiber laser in the water vapor transmission window. *Optica*, 3(12):1373, nov 2016.

[35] S. K□per and M. Stuke. Femtosecond uv excimer laser ablation. *Applied Physics B Photophysics and Laser Chemistry*, 44(4):199–204, dec 1987.

[36] K. J. Schafer, B. Yang, L. F. DiMauro, and K. C. Kulander. Above threshold ionization beyond the high harmonic cutoff. *Phys. Rev. Lett.*, 70:1599, 1993.

[37] P.B. Corkum. Plasma perspective on strong-field multiphoton ionization. *Phys. Rev. Lett.*, 71:1994, 1993.

[38] M. Lewenstein, Ph. Balcou, M.Yu. Ivanov, A. L'Huillier, and P.B. Corkum. Theory of high-order harmonic generation by low-frequency laser fields. *Phys. Rev. A*, 49:2117, 1994.

[39] A. L'Huillier, M. Lewenstein, P. Salières, Ph. Balcou, M. Yu. Ivanov, J. Larsson, and C. G. Wahlström. High-order harmonic generation cutoff. *Phys. Rev. A*, 48:R3433, 1993.

[40] M. D. Perry and J. K. Crane. High-order harmonic emission from mixed fields. *Phys. Rev. A*, 48, 1993.

[41] H. Eichmann, A. Egbert, S. Nolte, C. Momma, B. Wellegehausen, W. Becker, S. Long, , and J. K. McIver. Polarization-dependent high-order two-color mixing. *Phys. Rev. A*, 51:R3414, 1995.

[42] E. Mansten, J. M. Dahlström, P. Johnsson, M. Swoboda, A. L'Huillier, and J. Mauritsson. Spectral shaping of attosecond pulses using two-colour laser fields. *New. J. Phys.*, 10(8):083041, 2008.

[43] J. Mauritsson, P. Johnsson, E. Gustafsson, A. L'Huillier, K.J. Schafer, and M.B. Gaarde. Attosecond Pulse Trains Generated Using Two Color Laser Fields. *Phys. Rev. Lett.*, 97:013001, 2006.

[44] J. Mauritsson, P. Johnsson, E. Mansten, M. Swoboda, T. Ruchon, A. L'Huillier, and K. J. Schafer. Coherent Electron Scattering Captured by an Attosecond Quantum Stroboscope. *Phys. Rev. Lett.*, 100:073003, 2008.

[45] E. Mansten J. Mauritsson, M. Dahlström and T. Fordell. Sub-cycle control of strong field processes using two color laser fields. *J. Phys. B*, 2009.

[46] I.J. Sola, E. Mével, L. Elouga, E. Constant, V. Strelkov, L. Poletto, P. Villoresi, E. Benedetti, J.-P. Caumes, S. Stagira, C. Vozzi, G. Sansone, and M. Nisoli. Controlling attosecond electron dynamics by phase-stabilized polarization gating. *Nature Phys.*, 2:319, 2006.

[47] R. Clark Jones. A new calculus for the treatment of optical SystemsI description and discussion of the calculus. *Journal of the Optical Society of America*, 31(7):488, jul 1941.

[48] Bing Shan and Zenghu Chang. Dramatic extension of the high-order harmonic cutoff by using a long-wavelength driving field. *Phys. Rev. A*, 65(1):011804, Dec 2001.

[49] P. Colosimo, G. Doumy, C. I. Blaga, J. Wheeler, C. Hauri, F. Catoire, J. Tate, R. Chirla, A. M. March, G. G. Paulus, H. G. Muller, P. Agostini, and L. F. DiMauro. Scaling strong-field interactions towards the classical limit. *Nature Physics*, 4:386, 2008.

[50] Eiji J. Takahashi, Tsuneto Kanai, Kenichi L. Ishikawa, Yasuo Nabekawa, and Katsumi Midorikawa. Coherent Water Window X Ray by Phase-Matched High-Order Harmonic Generation in Neutral Media. *PHYSICAL REVIEW LETTERS*, 101(25), DEC 19 2008.

[51] T. Popmintchev, M.-C. Chen, D. Popmintchev, P. Arpin, S. Brown, S. Alisauskas, G. Andriukaitis, T. Balciunas, O.D. Mücke, A. Pugzlys, A. Baltuska, B. Shim, S.E. Schrauth, A. Gaeta, C. Hernández-Garcia, L. Plaja, A. Becker, Agnieszka J.-B., M.M. Murnane, and H.C. Kapteyn. Bright coherent ultrahigh harmonics in the keV X-ray regime from mid-infrared femtosecond lasers. *Science*, 336(6086):1287–1291, 2012.

[52] J. Tate, T. Auguste, H. G. Muller, P. Salieres, P. Agostini, and L. F. DiMauro. Scaling ofWave-Packet Dynamics in an Intense Midinfrared Field. *Phys. Rev. Lett.*, 98:013901, 2007.

[53] C M Heyl, C L Arnold, A Couairon, and A L'Huillier. Introduction to macroscopic power scaling principles for high-order harmonic generation. *J. Phys. B: At., Mol. Opt. Phys.*, 50(1):013001, dec 2017.

[54] M. Lewenstein, K. C. Kulander, K. J. Schafer, and P. H. Bucksbaum. Rings in above-threshold ionization: A quasiclassical analysis. *Phys. Rev. A*, 51:1495, 1995.

[55] K. Varjú, Y. Mairesse, B. Carre, M. B. Gaarde, P. Johnsson, S. Kazamias, R. Lopez-Martens, J. Mauritsson, K. J. Schafer, Ph. Balcou, A. L'Huillier, and P. Salières. Frequency chirp of harmonic and attosecond pulses. *J. Mod. Opt.*, 52:379, 2005.

[56] Stefanos Carlström, Jana Preclíková, Eleonora Lorek, Esben Witting Larsen, Christoph M Heyl, David Paleček, Donatas Zigmantas, Kenneth J Schafer, Mette B Gaarde, and Johan Mauritsson. Spatially and spectrally resolved quantum path interference with chirped driving pulses. *New Journal of Physics*, 18(12):123032, dec 2016.

[57] S. V. Milton. Exponential gain and saturation of a self-amplified spontaneous emission free-electron laser. *Science*, 292(5524):2037–2041, may 2001.

[58] W. Ackermann, G. Asova, V. Ayvazyan, A. Azima, N. Baboi, BahrJ., BalandinV., BeutnerB., BrandtA., BolzmannA., BrinkmannR., BrovkoO I., CastellanoM., CastroP., CataniL., ChiadroniE., ChorobaS., CianchiA., CostelloJ T., CubaynesD., DardisJ., DeckingW., Delsim-HashemiH., DelserieysA., Di PirroG., DohlusM., DustererS., EckhardtA., EdwardsH T., FaatzB., FeldhausJ., FlottmannK., FrischJ., FrohlichL., GarveyT., GenschU., GerthCh., GorlerM., GolubevaN., GraboschH.-J., GreckiM., GrimmO., HackerK., HahnU., HanJ H., HonkavaaraK., HottT., HuningM., IvanisenkoY., JaeschkeE., JalmuznaW., JezynskiT., KammeringR., KatalevV., KavanaghK., KennedyE T., KhodyachykhS., KloseK., KocharyanV., KorferM., KolleweM., KoprekW., KorepanovS., KostinD., KrassilnikovM., KubeG., KuhlmannM., LewisC L. S., LiljeL., LimbergT., LipkaD., LohlF., LunaH., LuongM., MartinsM., MeyerM., MichelatoP., MiltchevV., MollerW D., MonacoL., MullerW F. O., NapieralskiO., NapolyO., NicolosiP., NolleD., NunezT., OppeltA., PaganiC., PaparellaR., PchalekN., Pedregosa-GutierrezJ., PetersenB., PetrosyanB., PetrosyanG., PetrosyanL., PflugerJ., PlonjesE., PolettoL., PozniakK., PratE., ProchD., PucykP., RadcliffeP., RedlinH., RehlichK., RichterM., RoehrsM., RoenschJ., RomaniukR., RossM., RossbachJ., RybnikovV., SachwitzM., SaldinE L., SandnerW., SchlarbH., SchmidtB., SchmitzM., SchmuserP., SchneiderJ R., SchneidmillerE A., SchneppS., SchreiberS., SeidelM., SertoreD., ShabunovA V., SimonC., SimrockS., SombrowskiE., SorokinA A., SpanknebelP., SpesyvtsevR., StaykovL., SteffenB., StephanF., StulleF., ThomH., TiedtkeK., TischerM., ToleikisS., TreuschR., TrinesD., TsakovI., VogelE., WeilandT., WeiseH., WellhoferM., WendtM., WillI., WinterA., WittenburgK., WurthW., YeatesP., YurkovM V., ZagorodnovI., and ZapfeK. Operation of a free-electron laser from the extreme ultraviolet to the water window. *Nat Photon*, 1(6):336–342, Jun 2007.

[59] P. Emma. Lasing and Satuaration of LCLS FEL. *Proceeding of FEL2009*, 2009.

[60] L.-H. Yu, M. Babzien, I. Ben-Zvi, L. F. DiMauro, A. Doyuran, W. Graves, E. Johnson, S. Krinsky, R. Malone, I. Pogorelsky, J. Skaritka, G. Rakowsky, L. Solomon, X. J. Wang, M. Woodle, V. Yakimenko, S. G. Biedron, J. N. Galayda, E. Gluskin, J. Jagger, V. Sajaev, and I. Vasserman. High-Gain Harmonic-Generation Free-Electron Laser. *Science*, 289(5481):932–934, 2000.

[61] E. Allaria, G. De Ninno, and W.M. Fawley. The Second Stage of FERMI@Elettra: A Seeded FEL in the Soft X-ray Spectral Range. *Proceedings from FEL2009*, WEPC53, 2009.

[62] M. Bellini, C. Lyngå, A. Tozzi, M.B. Gaarde, C. Delfin, T.W. Hänsch, A. L'Huillier,

and C.-G. Wahlström. Temporal coherence of ultrashort high-order harmonic pulses. *Phys. Rev. Lett.*, 81:297, 1998.

[63] C. Lyngå, M. B. Gaarde, C. Delfin, M. Bellini, A. L'Huillier T. W. Hänsch, and C.-G. Wahlström. Studies of the temporal coherence of high-order harmonics. *Phys. Rev. A*, 60:4823, 1999.

[64] M. Gaarde, F. Salin, E. Constant, Ph. Balcou, K. J. Schafer, K. C. Kulander, and A. L'Huillier. Spatiotemporal separation of high harmonic radiation into two quantum path components. *Phys. Rev. A*, 59:1367, 1999.

[65] G. Sansone, E. Benedetti, J.-P. Caumes, S. Stagira, C. Vozzi, S. De Silvestri, and M. Nisoli. Control of long electron quantum paths in high-order harmonic generation by phase-stabilized light pulses. *Physical Review A*, 73(5), may 2006.

[66] A. Zaïr, M. Holler, F. Schapper, J. Biegert, L. Gallmann, U. Keller, A.S. Wyatt, A. Monmayrant, I.A. Walmsley, E. Cormier, T. Auguste, J.P. Caumes, and P. Salières. Quantum Path Interferences in High-Order Harmonic Generation. *Physical Review Letters*, 100:143902–1–4, 2008.

[67] F. Schapper, M. Holler, T. Auguste, A. Zair, M. Weger, P. Salieres, L. Gallmann, and U. Keller. Spatial fingerprint of quantum path interferences in high order harmonic generation. *Optics Express*, 18(3):2987–2994, 2010.

[68] F. Catoire, A. Ferré, O. Hort, A. Dubrouil, L. Quintard, D. Descamps, S. Petit, F. Burgy, E. Mével, Y. Mairesse, and E. Constant. Complex structure of spatially resolved high-order-harmonic spectra. *Physical Review A*, 94(6), dec 2016.

[69] Aura Inés Gonzalez, Ga□tan Jargot, Philippe Rigaud, Lo□c Lavenu, Florent Guichard, Antoine Comby, Thierry Auguste, Olivier Sublemontier, Michel Bougeard, Yoann Zaouter, Patrick Georges, Marc Hanna, and Thierry Ruchon. Spatio-spectral structures in high harmonic generation driven by tightly focused high repetition rate lasers. *Journal of the Optical Society of America B*, 35(4):A6, feb 2018.

[70] J. Mauritsson, P. Johnsson, R. López-Martens, K. Varjú, W. Kornelis, J. Biegert, U. Keller, M. B. Gaarde, K. J. Schafer, and A. L'Huillier. Measurement and control of the frequency chirp rate of high-order harmonic pulses. *Phys. Rev. A*, 70:R021801, 2004.

[71] N. B. Delone and V. P. Krainov. AC Stark shift of atomic energy levels. *Phys. Uspekhi*, 42:669, 1999.

[72] Wm. M. Wood, C. W. Siders, and M. C. Downer. Measurement of femtosecond ionization dynamics of atmospheric density gases by spectral blueshifting. *Physical Review Letters*, 67(25):3523–3526, dec 1991.

[73] N. Hartmann, G. Hartmann, R. Heider, M. S. Wagner, M. Ilchen, J. Buck, A. O. Lindahl, C. Benko, J. Grünert, J. Krzywinski, J. Liu, A. A. Lutman, A. Marinelli, T. Maxwell, A. A. Miahnahri, S. P. Moeller, M. Planas, J. Robinson, A. K. Kazansky, N. M. Kabachnik, J. Viefhaus, T. Feurer, R. Kienberger, R. N. Coffee, and W. Helml. Attosecond time–energy structure of x-ray free-electron laser pulses. *Nature Photonics*, 12(4):215–220, mar 2018.

[74] K. C. Prince, E. Allaria, C. Callegari, R. Cucini, G. De Ninno, S. Di Mitri, B. Diviacco, E. Ferrari, P. Finetti, D. Gauthier, L. Giannessi, N. Mahne, G. Penco, O. Plekan, L. Raimondi, P. Rebernik, E. Roussel, C. Svetina, M. Trovò, M. Zangrando, M. Negro, P. Carpeggiani, M. Reduzzi, G. Sansone, A. N. Grum-Grzhimailo, E. V. Gryzlova, S. I. Strakhova, K. Bartschat, N. Douguet, J. Venzke, D. Iablonskyi, Y. Kumagai, T. Takanashi, K. Ueda, A. Fischer, M. Coreno, F. Stienkemeier, Y. Ovcharenko, T. Mazza, and M. Meyer. Coherent control with a short-wavelength free-electron laser. *Nature Photonics*, 10(3):176–179, feb 2016.

[75] H.G. Muller. Reconstruction of attosecond harmonic beating by interference of two-photon transitions. *Appl. Phys. B*, 74:17, 2002.

[76] Y. Mairesse, A. de Bohan, L. J. Frasinski, H. Merdji, L. C. Dinu, P. Monchicourt, P. Breger, M. Kovačev, R. Taïeb, B. Carré, H. G. Muller, P. Agostini, and P. Salières. Attosecond synchronization of high-harmonic soft X-rays. *Science*, 302:1540, 2003.

[77] C.P. Hauri, W. Kornelis, F.W. Helbing, A. Heinrich, A. Couairon, A. Mysyrowicz, J. Biegert, and U. Keller. Generation of intense, carrier-envelope phase-locked few-cycle laser pulses through filamentation. *Appl. Phys. B*, 79:673, 2004.

[78] Huailiang Xu, Erik Lotstedt, Atsushi Iwasaki, and Kaoru Yamanouchi. Sub-10-fs population inversion in n_2^+ in air lasing through multiple state coupling. *Nature Communications*, 6(1), sep 2015.

[79] Jinping Yao, Shicheng Jiang, Wei Chu, Bin Zeng, Chengyin Wu, Ruifeng Lu, Ziting Li, Hongqiang Xie, Guihua Li, Chao Yu, Zhanshan Wang, Hongbing Jiang, Qihuang Gong, and Ya Cheng. Population redistribution among multiple electronic states of molecular nitrogen ions in strong laser fields. *Physical Review Letters*, 116(14), apr 2016.

[80] E. W. Larsen, S. Carlström, E. Lorek, C. M. Heyl, D. Paleček, K. J. Schafer, A. L'Huillier, D. Zigmantas, and J. Mauritsson. Sub-cycle ionization dynamics revealed by trajectory resolved, elliptically-driven high-order harmonic generation. *Scientific Reports*, 6(1), dec 2016.

[81] Hampus Wikmark, Chen Guo, Jan Vogelsang, Peter W. Smorenburg, Hélène Coudert-Alteirac, Jan Lahl, Jasper Peschel, Piotr Rudawski, Hugo Dacasa, Stefanos Carlström, Sylvain Maclot, Mette B. Gaarde, Per Johnsson, Cord L. Arnold, and

Anne L'Huillier. Spatiotemporal coupling of attosecond pulses. *Proceedings of the National Academy of Sciences*, 2019.

[82] L. Quintard, V. Strelkov, J. Vabek, O. Hort, A. Dubrouil, D. Descamps, F. Burgy, C. Péjot, E. Mével, F. Catoire, and E. Constant. Optics-less focusing of XUV high-order harmonics. *Science Advances*, 5(4):eaau7175, apr 2019.

[83] Samuel Bengtsson. Ultrafast opto-optical control of extreme ultraviolet light pulses, 2017.